Studies on atmospheric tides and planetary waves in the mesosphere-lower thermosphere (MLT) region using SuperDARN HF radars and meteor radar

by

Sibusiso H. Mthembu

Submitted in fulfillment of the academic requirements for the Degree of Doctor of Philosophy in the School of Chemistry and Physics, University of KwaZulu-Natal, Durban.

December 2013

As the candidate's supervisor I have/have not approved this thesis/dissertation for submission.

Signed: _____ Name: _____ Date: _____

As the candidate's co-supervisor I have/have not approved this thesis/dissertation for submission.

Signed: _____ Name: _____ Date: _____

Abstract

In this work, observational results of atmospheric dynamics caused by upward propagating atmospheric waves (tides, planetary waves and their interactions) in mesosphere-lower thermosphere (MLT) region are presented. This study is imperative as it contributes toward an understanding of various physical and dynamical processes that take place in this region.

The seasonal and inter-annual variations of tides are investigated using MLT winds recorded simultaneously by SuperDARN HF radars situated at Halley (75°S, 26°W), SANAE (72°S, 3°W) and Syowa (69°S, 36°E) from 1998 to 2007. The seasonal variation of tides was found to be characterized by maximum amplitudes in summer and minimum amplitudes in winter. The semidiurnal tides showed additional enhancement of amplitude in autumn. The seasonal behavior of the diurnal tide (semidiurnal tide) was found to be similar to that of tropospheric specific humidity (stratospheric ozone mixing ratio) which suggests a forcing mechanism as a possible source of tidal variation. Long-term variation of semidiurnal tide was found to be correlated to F10.7 solar flux, which suggests solar activity as a possible driver of the semidiurnal tide variation.

The variability of tides prior and post 2002 sudden stratospheric warming (SSW) event was studied using MLT winds derived from SuperDARN HF radars at Halley, SANAE and Syowa. Forcing mechanism using the ozone mixing ratio was found to be a possible source of semidiurnal tide (SDT) variability before the SSW event (160-250). Nonlinear interaction between planetary waves and tides on the other hand, was found to be a possible source responsible for the SDT variation just before, during and after the SSW event (250-300).

Nonlinear interaction between planetary waves and tides in the MLT region was studied using wind velocity data collected from meteor radar located at Rothera (68°S, 68°W) Antarctica during the year 2005. Wavelet analysis conducted on the wind data showed that the MLT region is dominated by SDT's and planetary waves with period ~ 5, 10, 16 and 23 days. Further analysis showed that SDT's are modulated at the periods of ~5, ~16 and ~23 days. However, non-linear interaction between the SDT and 16-day planetary wave was found to be mostly responsible for the variability of the SDT than the interaction between the SDT and 5- as well as 23-day planetary.

Study on the coupling between neutral atmosphere and ionosphere was conducted using SuperDARN HF radar and magnetic field data, both data sets were recorded from SANAE. The results showed that the quasi-16-day periodicity observed in the ionosphere most probably

originated from the neutral atmosphere. This was established on the basis of the travel time of oscillation from the neutral atmosphere to the ionosphere. Modulation of semidiurnal tide at quasi-16-day periodicity was found to be the mechanism responsible for the neutral atmosphere/ionosphere coupling through ionospheric electrodynamo effect. Magnetosphere/ionosphere coupling was also observed at quasi-20- and -23-day periodicity using Dst index as the magnetospheric parameter. Solar-ionosphere coupling on the other hand was not observed.

Preface

The work described in this thesis was carried out at the University of KwaZulu-Natal, School of Chemistry and Physics and at South African National Space Agency (SANSA), Hermanus under the supervision of Professor Sivakumar Venkataraman, co-supervision of Dr Sandile Malinga and the late Professor Sadhasivan Pillay. These studies represent original work by the author and have not otherwise been submitted in any form for any degree or diploma to any tertiary institution. Where use has been made of the work of others it is duly acknowledged in the text.

Sibusiso Hector Mthembu

Declaration 1 – Plagiarism

I, Sibusiso Hector Mthembu, declare that

1. The research reported in this thesis, except where otherwise indicated, is of my original research.

2. This thesis has not been submitted for any degree or examination at any other university.

3. This thesis does not contain other persons' data, pictures, graphs or other information, unless specifically acknowledged as being sourced from other persons.

4. This thesis does not contain other persons writing, unless specifically acknowledged as being sourced from other researchers. Where other written sources have been quoted, then: (a) Their words have been re-written but the general information attributed to them has been referenced (b) Where their exact words have been used, then their writing has been placed in italics, inside quotation marks, and referenced.

5. This thesis does not contain text, graphics or tables copied and pasted from the internet, unless specifically acknowledged, and the source being detailed in the thesis and in the References sections.

Signed: _____

Declaration 2 – Publications

Details of contribution to publications that form part and/or include research presented in this thesis (include publications in preparation, submitted, in press and published and give details of the contributions of each author to the experimental work and writing of each publication)

Publication 1

Mthembu, S. H., Sivakumar, V., Mitchell, N. J. and Malinga, S. B. (2013). Studies on planetary waves and tide interaction in the mesosphere-lower thermosphere region using meteor RADAR data from Rothera (68°S, 68°W), Antarctica. *J. Atmos. Sol. Terr. Phys.,* 102, 59–70.

(most of the contents are included in chapter-6)

Publication 2

Mthembu, S. H., Sivakumar, V. and Malinga, S. B. (2013), Semidiurnal tide variability during the 2002 sudden stratospheric warming (SSW) studied using SuperDARN HF radars, Antarctic. Submitted to *J. Atmos. Sol. Terr. Phys.* (Journal Ref. ATP3569R1)

(most of the contents are included in chapter-5)

Publication 3

Mthembu, S. H., Sivakumar, V., J. M. Ruohoniemi and Malinga, S. B. (2013), Long term variation of atmospheric tides studied using Southern hemisphere SuperDARN HF radars. Submitted to *Terr. Atmos. Ocean. Sci.* (Journal Ref. A13078)

(most of the contents are included in chapter-4)

Publication 4

Mthembu, S. H., Sivakumar, V. and Malinga, S. B. (2014), Coupling between the neutral atmosphere and ionosphere through planetary waves. To be submitted to *Annales Geophysicae,*

(most of the contents are included in chapter-7

Signed: _____

Acknowledgments

I would like to sincerely thank my supervisor Professor Sivakumar Venkataraman for his guidance and valuable advice during the preparation and compilation of this thesis. Your kindness and support in many aspects of this journey was much appreciated, may God bless and keep you in his care. A profound "thank you" to the late Professor Sadhasivan Pillay for his support, advice and confidence in my abilities. It was invaluable in ensuring my perseverance throughout this project. Sincere gratitude also goes to my co-supervisor Dr. Sandile Malinga who has partnered with me from Honours level, a sincere appreciation for your continuous, valuable and insightful contribution. This journey would have been impossible without the financial assistance of the South African National Space Agency (SANSA) and for this I am truly thankful.

Gratitude also goes to the following people:

- Dr Nkanyiso Bongumusa Mbatha "KaShandu" who was a brother and a friend. The advice he offered, and the discussions we engaged in, were an invaluable contribution to the success of this project, "Ngiyabonga Mfwethu".

- Professor Nick Mitchell, Dr. Dora Pancheva and Associate Professor Mike Ruohoniemi, your contributions and advice were instrumental in overcoming some of the challenges. Thank you.

- To all my friends at SANSA, Kenneth, Sfundo, Makhendlas, John Bosco 'The Mini Bus', Chris, Mpho, Stef, Chigo, Patrick 'Mdala' and Jean to mention the few, your contribution in many aspects was appreciated.

- Rose McArthur for proof reading this thesis, thank you.

- My lovely girlfriend Penelope for moral support, love, caring and so much more…thank you.

This work is dedicated to my younger brothers, sisters, nieces, nephews, sons and daughters. My aspiration is that my achievements inspire you to aim for greatness. This is proof that nothing is impossible - all you need is hope, dedication and perseverance. To the older generation, I would like to say thank you for your moral support, advices and contributions in many areas - I could not have done this without you - love you all and thank you.

Table of contents

Table of figures

1 Introduction and Background theory

The atmosphere is a thin blanket that covers the planet earth thereby protecting the living organisms on it. For example, the ozone layer in the stratosphere absorbs harmful ultra-violet radiation from the sun, the abundance of oxygen in the atmosphere helps burn external bodies emanating from outer space e.g. meteors, preventing them from reaching the earth. Moreover the earth's atmosphere, among other things, makes climate possible, provides oxygen and water to sustain and prevent living organisms from extinction. Thus understanding dynamical processes, physics and chemistry that determine the behaviour of the atmosphere is imperative. South African's contribution towards atmospheric science research has contributed greatly in enhancing the understanding of some of the complex processes.

The Mesosphere-lower thermosphere (MLT) region is controlled by dynamics driven by large scale atmospheric waves originating from the lower regions of the atmosphere. Interaction among these waves and/or with mean flow drives large scale circulations that contribute to complicate the physics of this region (Manson et al., 2003). Furthermore, signatures of oscillations with planetary wave periods have been observed in the ionosphere regardless of the fact that they are unable to propagate beyond 100-110 km altitude (Lastovicka et al., 2003). Modeling studies using space- and ground-based observations distributed around the globe play a crucial role in trying to understand the MLT dynamics and coupling between neutral atmosphere and the ionosphere.

There is a substantial amount of work being conducted using ground-based observations to study the dynamics of the MLT region, however most of these studies were in the Northern hemisphere (Lysenko et al., 1994; Mitchell et al., 1999; Pancheva, 2000; Merzlyakov et al., 2001; Luo et al., 2002; Igarashi et al., 2002; Middleton et al., 2002; Manson et al., 2004, 2005; Jacobi et al., 2007, 2009) and few from the Southern hemisphere (Riggin et al., 1999, 2003; Murphy et al., 2003, 2006; Baumgaertner et al., 2006; Hibbins et al., 2006; Hibbins and Jarvis, 2008; Merzlyakov at al., 2009; Iimura et al., 2011; Hibbins et al., 2010, 2011). Among the Southern hemisphere studies most were conducted using medium frequency (MF) radars measurements (Riggin et al., 1999, 2003; Murphy et al., 2003, 2006; Baumgaertner et al., 2006; Hibbins and Jarvis, 2006; Merzlyakov at al., 2009; Iimura et al., 2011). Discovery by Hall et al. (1997), that the Super Dual Auroral Radar Network (SuperDARN) HF radars are also capable of measuring the mesospheric winds was remarkable because such measurements contribute towards the study of MLT dynamics. Thus far, there has been a limited number of studies conducted using SuperDARN HF radars measurements e.g. Hibbins and Jarvis (2008); Hibbins

et al. (2010, 2011); Mbatha et al. (2010); Mbatha (2012) and therefore the current study further addresses SuperDARN HF radars' contribution towards the study of MLT dynamics.

In particular, this study addresses two aspects: the first part addresses the use of SuperDARN HF radar winds recorded in the Southern hemisphere to study the dynamics in the MLT region, that are caused by upward propagating atmospheric tides (periods 6, 8, 12 and 24 h) and planetary waves (periods ranging from 2 to 30 days). Interaction of tides and planetary waves with the mean circulation drives short-term and long-term conditions which in turn set the MLT region in a state far removed from radiative equilibrium. Normally, these conditions are observed at certain locations and thus their global scale nature could not be addressed. Thus the contribution made by SuperDARN HF radars measurement in studying the MLT dynamic is crucial.

The second part of this study is to investigate the coupling effect between the neutral atmosphere and the ionosphere. Propagation conditions and dissipation inhibits planetary waves from propagating beyond 100-110 km altitude however planetary wave signature has been observed in the ionosphere (e.g. Pancheva et al., 2002, 2006; Borries et al., 2007). Among possible mechanisms responsible for such coupling, ionospheric electrodynamo effect is one of a causative mechanism. During this process neutral winds driven by tides (modulated at planetary wave periods) generate electric field and current which in turn induces wave-like magnetic field perturbations that can be detected by ground-based magnetometers.

Different topics presented in this work are largely dependent on the availability of the data and thus some of the specific subjects are outlined at the beginning of each chapter. This chapter provides a brief description of neutral and ionized atmospheric regions in Section 1.1, followed by a brief review of theoretical aspects of atmospheric dynamics in Section 1.2. Section 1.3 describes coupling between neutral atmosphere and ionosphere as well as a brief theoretical aspect of electrodynamic effect. The thesis outline is presented in Section 1.4.

1.1 Atmospheric structure

The purpose of this study is to investigate dynamics that take place in the MLT region (80-110 km) caused by atmospheric waves excited from the lower regions of the atmosphere. The troposphere and stratosphere indirectly form part of this study since they are regions from where atmospheric waves are excited, therefore they are briefly discussed. Another aspect of the study

is the coupling effect between the neutral atmosphere and the ionosphere, thus the ionospheric region where coupling (E- and F-regions) takes place will be briefly looked at.

1.1.1 Neutral atmosphere

The neutral atmosphere is the region that extends from sea level to about 60 km, above which ionization starts to dominate. Based on the thermal structure of the neutral atmosphere from the ground, different regions with different properties can be identified and these are termed the 'troposphere, stratosphere and mesosphere'.

1.1.1.1 Troposphere

With reference to Figure 1.1, the troposphere is the lowest region of the atmosphere extending from sea level up to about 12 km (over mid-latitude). This region contains 75-80% of the total mass of the atmosphere and almost all the weather system takes place in this region. 99% of water vapor is found in this region thus the majority of thermal diurnal tides are excited in the troposphere as they are formed due to absorption of solar radiation by water vapor (Zhang et al., 2010). The ground absorbs more solar radiation than water vapor and therefore the temperature of the troposphere falls with altitude. The tropopause is the region that separates the troposphere and the stratosphere. In this region the lapse rate changes from positive in the troposphere to negative in the stratosphere.

1.1.1.2 Stratosphere

The stratosphere is the region above the troposphere, extending from the tropopause to ~50 km. The temperature in this region is stratified with layers of low temperature at lower altitude and layers of high temperature at higher altitudes. The temperature increase with height is due to an increase in ozone concentration with height which then absorbs more solar radiation (Gold, 1909). Semidiurnal tides are generated through absorption of solar radiation by ozone, thus substantial amounts of semidiurnal tides are formed in this region. A spectacular phenomenon also occurring in this region is a sudden stratospheric warming which is characterized by rapid enhancement of temperature followed by reversal of stratospheric winds poleward of 60° latitude in both hemispheres (Matsuno, 1971). The limit of the stratosphere is marked by the stratopause, which is the layer separating stratosphere from mesosphere.

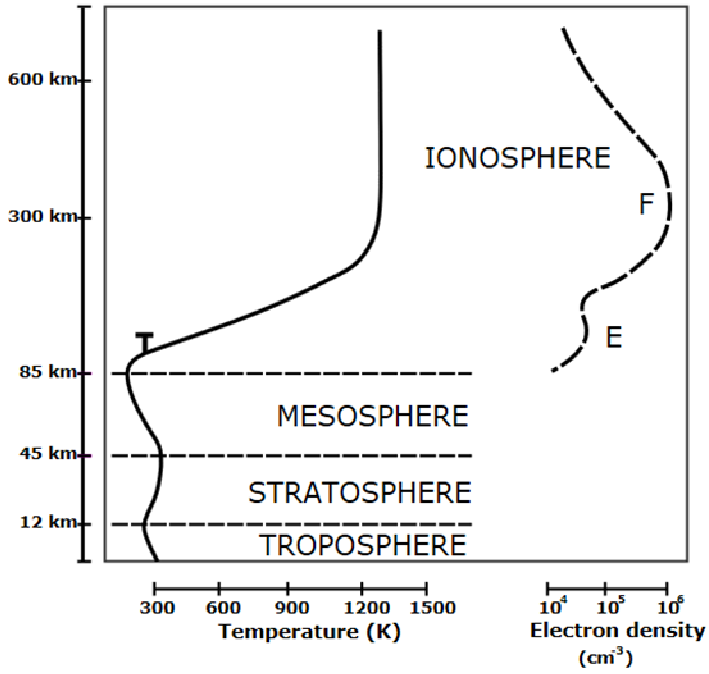

Figure 1.1: Vertical profile of the atmosphere. Modified version from http://en.wikipedia.org/wiki/Ionosphere.

1.1.1.3 Mesosphere

Above the stratopause is the mesospheric region extending from the stratopause to ~90 km. Ozone concentration in this region drastically decreases with increasing height resulting in a decrease in solar radiation absorption by ozone and a consequent decrease in temperature with height, added to the fact that the atmospheric density exponentially decreases with height. Furthermore, the temperature in this region decreases due to CO_2 radiating heat to outer space. Atmospheric waves excited from the troposphere and the stratosphere propagate upward and their amplitudes grow exponentially with height. Above 80 km, these waves become convectively unstable and break. This deposits their momentum and energy and drives some of atmospheric dynamics which will be discussed later. Interesting phenomena found in this region are noctilucent clouds. These are the highest clouds in the earth's atmosphere composed of small ice droplets which are visible during twilight, as illuminated by light rays from the sun below the horizon. The end of this region is designated by mesopause, which is the coldest layer of the atmosphere.

1.1.2 Ionosphere

The ionosphere is the region of the atmosphere extending from about 60 to 600 km and consisting of neutral and charged particles. The charged particles are the product of ionization

of neutral molecules that have been bombarded by high energetic solar radiation. The ionosphere is divided into three layers i.e. D-, E- and F-region separated according to their composition, ion and electron densities. The focus of this study is in the E- and F-region. Electron density has a latitudinal, diurnal and seasonal variation but in this study, altitude variation as shown in Figure 1.1 was of interest.

1.1.2.1 E-region

The E-region extends from about 85 to 130 km altitude and is dominated by oxygen and nitrogen molecules. This region is formed during the day where free electrons result from ionization of O_2 and N_2 by X-ray and UV radiations to form NO^+ and O^+. Just like in the D-region, at night reverse reaction takes place and this region weakens, or to a larger extent disappears.

1.1.2.2 F-region

Above the E-region is the F-region which is broader and extends from about 130 to 600 km altitude. This region is dominated by O^+ ions while H^+ dominates at higher altitudes. UV radiations are responsible for ionization of oxygen molecule. Unlike the E-region which perishes at night, the F-region persists due to downward diffusion of ions from higher region.

Subsequent to the consideration of neutral atmosphere and ionospheric regions, the theoretical aspects of atmospheric waves dominating these regions are discussed here.

1.2 Brief review of atmospheric dynamics

There are numerous factors that contribute to the complexity of dynamics in the MLT region. For example, those caused by atmospheric waves including planetary waves, tides and gravity waves originating from lower regions of the atmosphere. However, this study excludes a discussion of gravity waves because the data used here were sampled at 1 h interval which is too long to capture gravity wave short-term periodicity (less than an hour).

Planetary waves are large-scale oscillations that originate from the troposphere and propagate horizontally and vertically to the stratosphere, mesosphere and sometimes beyond especially in winter when propagation conditions are conducive. They are excited by, among other sources, topography and instabilities associated with temperature variations. Periods of interest in this study are those ranging from 2 to 30 days but commonly observed periods are those close to 2, 5, 10, 16, 23-27 days. Planetary waves with periods 23-27 days are related to the earth's rotation

while those with periods close to 2, 5, 10 and 16 days are related to the Rossby normal modes (Salby, 1984; Luo et al., 2002). Observational studies have reported westward propagating waves with zonal wavenumber one (e.g. Clark et al., 2002; Dowdy et al., 2004; Espy et al., 2005) and vertical wavelengths ranging from 50 to100 km (Pancheva and Mitchell 2004; Day and Mitchell, 2010; Mthembu et al., 2013).

Another category of waves to be discussed is atmospheric thermal tides. These are global-scale oscillations excited in the troposphere, stratosphere, mesosphere and thermosphere due to absorption of solar radiation by water vapour, ozone, oxygen and nitrogen molecules. The tides are classified according to their periods i.e. the diurnal (24 h), semidiurnal (12 h), terdiurnal (8 h) and quardiurnal (6 h) tides. Upon excitation, tides propagate vertically and horizontally with zonal wavenumbers ranging from -5 to 5 and vertical wavelengths from 50 km and more (Pancheva and Mitchell, 2004; Mthembu et al., 2013). The tides are further divided into migrating and nonmigrating according to their motion relative to the sun i.e. migrating tide are sun synchronous while nonmigrating tides are not sun synchronous.

In and above the stratospheric region, these waves are large enough that wave-wave interaction between tides and planetary waves or wave-mean flow interaction between planetary wave and zonal mean winds occurs. These processes result in numerous atmospheric dynamical processes which include among others, reversal of zonal mean winds, nonlinear interaction between waves, sudden stratospheric warming, and coupling between different layers of atmosphere. Some of the observational evidence of these atmospheric dynamical processes is presented in this study; therefore an understanding of the basics of the atmospheric dynamic is very imperative in order to give a better account of the obtained results. Accordingly, the theoretical aspect of these waves is discussed first including derivation of their equations.

1.2.1 Fundamental equations

Atmospheric dynamics are governed by fundamental equations including conservation of mass, momentum and energy. In their general form, these equations are far more complicated than necessary (Andrews et al., 1987). Scale analysis shows that application of some approximations may lead to some simplification. These approximations include using spherical coordinates, replacing the vertical momentum equation by hydrostatic balance, neglecting Coriolis force associated with horizontal component of the earth's rotation and replacing distance r from any point in the atmosphere to the center of the earth by a mean radius a. A set of equations that result after these simplifications is called primitive equations. Among numerous choices of the

vertical coordinate, primitive equations become simpler when log-pressure coordinates are used. Thus using spherical and log-pressure coordinates, the primitive equations become:

$$\frac{\partial u}{\partial t}+\frac{u}{a\cos\phi}\frac{\partial u}{\partial \lambda}+\frac{v}{a\cos\phi}\frac{\partial v}{\partial \phi}(u\cos\phi)+w\frac{\partial u}{\partial z}-fv+\frac{1}{a\cos\phi}\frac{\partial \Phi}{\partial \lambda}=X$$

Equation 1.1

$$\frac{\partial v}{\partial t}+\frac{u}{a\cos\phi}\frac{\partial u}{\partial \lambda}+\frac{v}{a}\frac{\partial v}{\partial \phi}+w\frac{\partial u}{\partial z}+\frac{u^2\tan\phi}{a}+fu+\frac{1}{a}\frac{\partial \Phi}{\partial \phi}=Y$$

Equation 1.2

$$\frac{1}{a\cos\phi}\frac{\partial u}{\partial \lambda}+\frac{1}{a\cos\phi}\frac{\partial}{\partial \phi}(v\cos\phi)+\frac{\partial w}{\partial z}-\frac{w}{H}=0$$

Equation 1.3

$$\frac{\partial T}{\partial t}+\frac{u}{a\cos\phi}\frac{\partial T}{\partial \lambda}+\frac{v}{a}\frac{\partial T}{\partial \phi}+w\left(\frac{\partial T}{\partial z}+\frac{\kappa T}{H}\right)=\frac{J}{c_p}$$

Equation 1.4

$$\frac{\partial \Phi}{\partial z}=\frac{RT}{H}$$

Equation 1.5

Equation 1.1 to Equation 1.5 represents zonal and meridional momentum equations, the mass continuity equation, thermodynamic energy equation and hydrostatic balance in the vertical, respectively. The symbols used are indicated below:

t	time
ϕ	latitude
λ	longitude
z	log-pressure vertical coordinate ($=-H\ln(p/p_o)$)
u	eastward velocity
v	northward velocity
w	upward velocity ($=dz/dt$)
H	scale height ($\equiv RT/g$) where T is a constant mean temperature
g	gravitational acceleration
f	Coriolis force ($=2\Omega\sin\phi$)
Ω	angular velocity of earth
Φ	geopotential
T	temperature

c_p specific heat at constant pressure

κ gas constant ($= R / c_p$)

R gas constant for dry air

a radius of earth

J heat rate per unit mass

X, Y horizontal components of unspecified non-conservative forcing

Replacing the spherical coordinates (ϕ, λ) with Cartesian coordinates (x, y) and considering height as the vertical coordinate with small increment distances in eastward and northward directions given by $dx = a\cos\phi d\lambda$ and $dy = ad\phi$, the momentum, continuity and the thermodynamic energy equations become:

$$\frac{Du}{Dt} - \left(2\Omega + \frac{u}{a\cos\phi}\right)(v\sin\phi - w\cos\phi) + \frac{1}{\rho}\frac{\partial p}{\partial x} = X$$

Equation 1.6

$$\frac{Dv}{Dt} + \frac{wv}{a} + \left(2\Omega + \frac{u}{a\cos\phi}\right)uv\sin\phi + \frac{1}{\rho}\frac{\partial p}{\partial y} = Y$$

Equation 1.7

$$\frac{Dw}{Dt} - \frac{u^2 + v^2}{a} - 2\Omega u\cos\phi + \frac{1}{\rho}\frac{\partial p}{\partial z} + g = Z$$

Equation 1.8

$$\frac{1}{p}\frac{D\rho}{Dt} + \frac{\partial u}{\partial x} + \frac{\partial v}{\partial y} + \frac{\partial w}{\partial z} = 0$$

Equation 1.9

$$\frac{D\theta}{Dz} = -g\rho$$

Equation 1.10

with $\frac{D}{Dt}$ being the material derivative given by $\frac{D}{Dt} = \frac{\partial}{\partial t} + u\frac{\partial}{\partial x} + v\frac{\partial}{\partial y} + w\frac{\partial}{\partial z}$, Z is the vertical component of unspecified non-conservative forcing, ρ is density and $\theta = T(p_o / p)^{\kappa}$ is

potential temperature. Further simplification can be achieved by using the following approximations:

$$\frac{|u|}{a\cos\phi} << 2\Omega$$

$$|w\cos\phi| << |v\sin\phi|$$

$$|wv|/r << |u\sin\phi|$$

And thus Equation 1.6 to Equation 1.8 become:

$$\frac{Du}{Dt} - fv + \frac{1}{\rho}\frac{\partial p}{\partial x} = X$$

Equation 1.11

$$\frac{Dv}{Dt} + fu + \frac{1}{\rho}\frac{\partial p}{\partial y} = Y$$

Equation 1.12

$$\frac{Dw}{Dt} + \frac{1}{\rho}\frac{\partial p}{\partial z} + g = 0$$

Equation 1.13

Using scale analysis, Equation 1.11 to Equation 1.13 further simplify to

$$fv = \frac{1}{\rho}\frac{\partial p}{\partial x}$$

Equation 1.14

$$-fu = \frac{1}{\rho}\frac{\partial p}{\partial y}$$

Equation 1.15

$$\frac{\partial p}{\partial z} = -g\rho$$

Equation 1.16

where Equation 1.14 and 1.15 are called geostrophic while Equation 1.16 is hydrostatic. Substituting the ideal gas law $p = RT\rho$ in Equation 1.15 and Equation 1.16, thermal windshear equations can be derived as:

$$f\frac{\partial v}{\partial z} = \frac{g}{T}\frac{\partial T}{\partial x}$$

Equation 1.17

$$f\frac{\partial u}{\partial z} = -\frac{g}{T}\frac{\partial T}{\partial y}$$

Equation 1.18

1.2.2 Atmospheric tides

The present study concentrates specifically on atmospheric solar tides. These are global-scale periodic oscillations in the atmosphere that are excited through absorption of infrared radiation by water vapor in the troposphere, ultraviolet radiation by ozone in the stratosphere and mesosphere as well as ultraviolet radiation by molecular oxygen in the thermosphere. Tides are classified according to their periods i.e. diurnal (24 h), semidiurnal (12 h) terdiurnal (8 h) and quadiurnal (6 h) tides. The terdiurnal and quadiurnal tides may have smaller amplitudes and thus are excluded in the present study. In general, the semidiurnal tides seem to dominate at higher latitude while the diurnal tides dominate at the equatorial regions (Manson et al., 1989; Manson and Meek, 1991). This is because the periodicity of the diurnal tide at latitudes higher than 30° are longer than the inertial period which result in the trapping of the diurnal tides at these latitudes on both hemispheres. Upon excitation the tides propagate upward, their amplitude grows exponentially due to a decrease in density. At the MLT region tidal amplitude are large enough to contribute to atmospheric dynamics which may include for example nonlinear interaction with the gravity waves (Fritts and Vincent, 1987; Ortland and Alexander, 2006) as well as with planetary waves (Beard et al., 1999; Jacobi, 1999; Pancheva, 2000; Pancheva and Mukhtarov, 2000; Pancheva, 2001; Pancheva et al., 2002; Pancheva and Mitchell, 2004; Baumgaertner et al., 2005; Mthembu et al., 2013). On the theoretical and observational point of view (Sprenger and Schminder, 1969; Greisiger et al., 1987; Namboothiri et al., 1994; Bremer et al., 1997; Jacobi et al., 1997; Baumgaertner et al., 2005; Hagan et al., 1999; Labitzke, 2005; Iimura et al., 2010; Iimura et al., 2011), the tidal amplitudes have been shown to be modulated by numerous mechanisms which result in variation of tidal amplitudes at periods ranging from a few days to several years. The theoretical aspects of tides are considered prior to the presentation of the observational results.

The theoretical discussion on the tidal waves presented here is based on Chapman and Lindzen (1970). There are numerous approximations that are considered to simplify the derivation of tidal waves which include using Navier-Stokes equations for a compressible gas expressed in a spherical coordinate for a frame of reference rotating with the earth. Another approximation is that the tidal fields are taken as linearized perturbations around some basic state, e.g. for the eastward velocity $u = u_o + u'$ where u_o is the basic state eastward velocity and u' is the perturbation eastward velocity. Assuming that the basic state and the horizontal component of unspecified non-conservative forcing may be set to zero, a linearized version of the primitive equations become:

$$\frac{\partial u'}{\partial t} - 2\Omega v' \cos\phi = -\frac{1}{a}\frac{\partial}{\partial \phi}\left(\frac{p'}{\rho_o} + \Phi'\right)$$

Equation 1.19

$$\frac{\partial v'}{\partial t} + 2\Omega u' \cos\phi = -\frac{1}{a\sin\phi}\frac{\partial}{\partial \lambda}\left(\frac{p'}{\rho_o} + \Phi'\right)$$

Equation 1.20

$$\frac{\partial p'}{\partial z} = -g\rho' - \rho_o \frac{\partial \Phi'}{\partial z}$$

Equation 1.21

$$\frac{\partial \rho'}{\partial t} + w\frac{\partial \rho'}{\partial z} = -\rho'\Gamma, \textit{ where}$$
$$\Gamma = \left(\frac{1}{a\sin\phi}\frac{\partial}{\partial \phi}\left(u'\sin\phi\right) + \frac{1}{a\sin\phi}\frac{\partial v'}{\partial \lambda} + \frac{\partial w'}{\partial z}\right)$$

Equation 1.22

$$\frac{R}{\gamma - 1}\left(\frac{\partial T'}{\partial t} + w\frac{\partial T_o}{\partial z}\right) = \frac{gH}{\rho}\frac{D\rho'}{Dt} + J'$$

Equation 1.23

$$\frac{p'}{p_o} = \frac{T'}{T_o} + \frac{\rho'}{\rho_o}$$

Equation 1.24

where u', v', p', ρ', T' and J' are perturbation of eastward velocity, northward velocity, pressure, density, temperature and heat rate per unit mass, p_o, T_o and ρ_o are basic state pressure, temperature and density and $\gamma = c_p / c_v$ with c_v being specific heat at constant volume. Other variables are as mentioned earlier. Here Equation 1.19 to Equation 1.24 are linearised zonal and meridional momentum equations, the mass continuity equation,

thermodynamic energy equation, hydrostatic balance in the vertical and perfect gas law, respectively. Substituting Equation 1.24 into Equation 1.23 and eliminating T' yield:

$$\frac{Dp}{Dt} = \frac{\partial p'}{\partial t} + w\frac{\partial p_o}{\partial z} = \lambda gH\frac{D\rho'}{Dt} + (\gamma - 1)\rho_o J$$

Equation 1.25

$\frac{Dp}{Dt}$ is normally considered as a main variable and the related variable which is suitable in the tidal theory is given by

$$G = -\frac{1}{\gamma p_o}\frac{Dp}{Dt}$$

Equation 1.26

and will be used later. To separate vertical dependence from horizontal dependence, complex quantity given by Equation 1.27 is used since in tidal theory we are concerned with fields that are periodic in time and longitude.

$$f = f^{\sigma,s}(\phi, z)e^{i(\sigma t + s\lambda)}$$

Equation 1.27

From Equation 1.27, $2\pi/\sigma$ represent the solar day, $s = 0, \pm 1, \pm 2, \ldots$ is the zonal wavenumber, $\frac{\partial}{\partial t} = i\sigma$ and $\frac{\partial}{\partial \lambda} = is$. Substituting Equation 1.27 into Equation 1.19 and Equation 1.20 and solving for u' and v' yields:

$$u'^{\sigma,s} = \frac{i\sigma}{4a\Omega^2\left(f^2 - \cos^2\phi\right)}\left(\frac{\partial}{\partial\phi} + \frac{s\cot\phi}{f}\right)\left(\frac{p'^{\sigma,s}}{\rho_o} + \Phi'^{\sigma,s}\right)$$

Equation 1.28

$$v'^{\sigma,s} = \frac{-\sigma}{4a\Omega^2\left(f^2 - \cos^2\phi\right)}\left(\frac{\cos\phi}{f}\frac{\partial}{\partial\lambda} + \frac{s}{\sin\phi}\right)\left(\frac{p'^{\sigma,s}}{\rho_o} + \Phi'^{\sigma,s}\right)$$

Equation 1.29

where $f \equiv \frac{\sigma}{2\Omega}$, p' is a complex function. Substituting Equation 1.28 and Equation 1.29 into the expression Γ in Equation 1.22 yields:

$$\Gamma - \frac{\partial w}{\partial z} = \frac{i\sigma}{4a^2\Omega^2} F\left(\frac{p'}{\rho_o} + \Phi\right)$$

Equation 1.30

where Γ is the velocity divergence and

$$F \equiv \frac{1}{\sin\lambda}\frac{\partial}{\partial\lambda}\left(\frac{\sin\lambda}{f^2 - \cos^2\lambda}\frac{\partial}{\partial\lambda}\right) - \frac{1}{f^2 - \cos^2\lambda}\left(\frac{s}{f}\frac{f^2 + \cos^2\lambda}{f^2 - \cos^2\lambda} + \frac{s^2}{\sin^2\lambda}\right)$$

Equation 1.31

Equation 1.21, Equation 1.22, Equation 1.25, Equation 1.26 and Equation 1.30 can be reduced into a single expression of G alone:

$$H\frac{\partial^2 G^{\sigma,s}}{\partial z^2} + \left(\frac{\partial H}{\partial z} - 1\right)\frac{\partial G^{\sigma,s}}{\partial z} - \frac{i\sigma}{g}\frac{\partial^2 \Phi^{\sigma,s}}{\partial z^2} = \frac{g}{4a^2\omega^2} F\left(\left(\frac{\partial H}{\partial z} + \kappa\right)G^{\sigma,s} - \frac{\kappa J^{\sigma,s}}{\gamma g H}\right)$$

Equation 1.32

Assuming a shallow atmosphere; $\frac{\sigma}{g}\frac{\partial^2\Phi}{\partial z^2}$ can be neglected and Equation 1.32 reduces to:

$$H\frac{\partial^2 G^{\sigma,s}}{\partial z^2} + \left(\frac{\partial H}{\partial z} - 1\right)\frac{\partial G^{\sigma,s}}{\partial z} = \frac{g}{4a^2\omega^2} F\left(\left(\frac{\partial H}{\partial z} + \kappa\right)G^{\sigma,s} - \frac{\kappa J^{\sigma,s}}{\gamma g H}\right)$$

Equation 1.33

Equation 1.33 can be solved by the method of separation of variables. If we assume that

$$G^{\sigma,s} = \sum_n L_n^{\sigma,s}(z)\Theta_n^{\sigma,s}(\phi)$$

Equation 1.34

and that $\{\Theta_n^{\sigma,s}(\phi)\}_{all\ n}$ is complete for $0 \le \phi \le \pi$, then J may be expanded as:

$$J^{\sigma,s} = \sum_n J_n^{\sigma,s}(z)\Theta_n^{\sigma,s}(\phi)$$

Equation 1.35

Thus substituting Equation 1.34 and Equation 1.35 into Equation 1.33 yields:

$$F\left(\Theta_n^{\sigma,s}\right) = -\frac{4a^2\Omega^2}{gh_n^{\sigma,s}}\Theta_n^{\sigma,s}$$

Equation 1.36

and

$$H\frac{d^2L^{\sigma,s}}{dz^2} + \left(\frac{dH}{dz} - 1\right)\frac{dL_n^{\sigma,s}}{dz} = +\frac{1}{h_n^{\sigma,s}}\left(\frac{dH}{dz} + \kappa\right)L_n^{\sigma,s} = \frac{\kappa J^{\sigma,s}}{\gamma g H h_n^{\sigma,s}}$$

Equation 1.37

Equation 1.36 is called Laplace's Tidal Equation which represents the horizontal structure of the tide and according to Hough (1897) can be rewritten as:

$$\frac{d}{d\mu}\left(\frac{1-\mu^2}{f^2-\mu^2}\frac{d\Theta_n}{\mu}\right) - \frac{1}{f^2-\mu^2}\left[\frac{s}{f}\frac{f^2+\mu^2}{f^2-\mu^2} + \frac{s^2}{1-\mu^2}\right]\Theta_n + \frac{4a^2\Omega^2}{gh_n}\Theta_n = 0$$

Equation 1.38

where $\mu = \sin\phi$ is a latitude variable, $\frac{4a^2\Omega^2}{gh_n}$ are the eigenvalues of the problem, $\Theta_n(\phi)$ are the eigenfunction and are called Hough function which is complete between latitude $-90 \le \phi \le 90$. The subscript n represents the number of possible solutions while s represents the number of waves along the latitudinal cycle and the sign indicates the wave direction where negative denotes eastward and positive denotes westward. Figure 1.2 presents the example of the latitudinal distribution of the first three Hough Functions of the solar migrating tide where $s = 2$ and $\sigma = 2$.

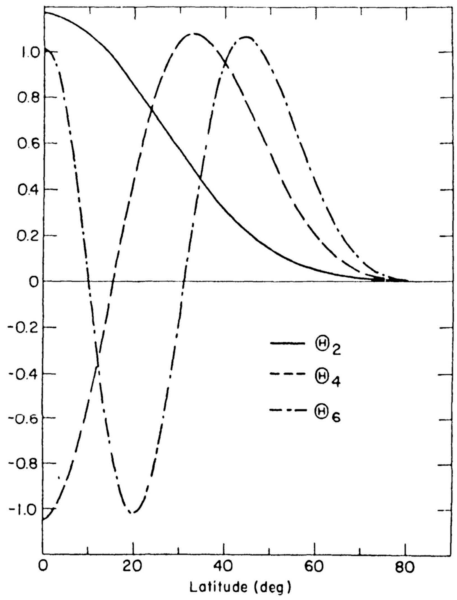

Figure 1.2: The first three Hough functions for the migrating solar semidiurnal tide as a function of latitude (sourced from Sandford 2008).

Equation 1.37 is an inhomogeneous vertical structure equation where $h_n^{\sigma,s}$ is the constant of separation. Considering $z = -\log\left(\frac{p_o}{p_o(0)}\right)$ and $L_n^{\sigma,s} = e^{z/2} W_n^{\sigma,s}$ Equation 1.37 can be reduced to:

$$\frac{d^2 W_n^{\sigma,s}}{dz^2} - \frac{1}{4}\left[1 - \frac{4}{h_n^{\sigma,s}}\left(\kappa H + \frac{dH}{dz}\right)\right] W_n^{\sigma,s} = \frac{\kappa J_n'^{\sigma,s}}{\gamma g h_n} e^{-z/2}$$

Equation 1.39

where W is a perturbation in the vertical velocity. The inhomogeneous vertical equation can be solved for a vertical structure of various modes with boundary condition. The lower boundary condition is given by $z = 0$ while the upper boundary condition depends on the sign of the factor $\frac{4}{h_n^{\sigma,s}}\left(\kappa H + \frac{dH}{dz}\right)$ in Equation 1.39 (Lindzen 1969). When this factor is positive, the solution is vertically propagating wave. However, if the factor is negative, the energy of the wave is trapped near the level of excitation.

1.2.3 Planetary waves

Planetary waves are quasi-horizontal disturbances whose restoring force is the Coriolis force. These disturbances are excited in the lower region of the atmosphere (troposphere) by among other sources, topography and the instabilities associated with the temperature variations and propagate towards the middle atmosphere. Observational studies (Beard et al., 2001) have shown that planetary waves are normally found with periods, close to about 2, 5, 10 and 16 days which corresponds to normal modes (Salby, 1984). Upward propagating planetary wave drives numerous atmospheric dynamics through wave-mean flow interaction and wave-wave interaction which may result from e.g. interaction with the background mean flow as well as non-linear interaction with atmospheric tides. The consequence of non-linear interaction between planetary wave and tide is the short-term variability of tidal amplitude. This nonlinear interaction results in the formation of secondary waves which may be accompanied by a reduction of tidal amplitude caused by the energy loss during the formation of 'baby' waves. Another consequence of upward propagating planetary wave is forcing of sudden stratospheric warming (SSW) which is attributed to an interaction of upward propagating planetary waves with zonal mean circulation (Matsuno, 1971). These phenomena will be discussed more extensively however; the theory of planetary waves will now be deliberated.

The theory of planetary waves presented here is based on the work by Holton (1975); Volland (1988); Mbatha (2012). The reduced primitive Equation 1.11 to Equation 1.13 are used with some approximations applied to simplify them. Firstly, these equations may be approximated by Boussinesq equations where density variations are ignored except when they are coupled to gravity, secondly the Boussinesq equations are approximated by restricting the flow to quasi-geostrophic flow. The result of these approximations is a quasi-geostrophic vorticity equation given by:

$$D_g q = 0$$

Equation 1.40

where D_g is the time derivative following the geostrophic flow (u_g, v_g) which is in turn given by $D_g = \frac{\partial}{\partial t} + u_g \frac{\partial}{\partial x} + v_g \frac{\partial}{\partial y}$ and the parameter q is the quasi-geostrophic potential and is given by:

$$q = f_o + \beta y + \frac{\partial^2 \psi}{\partial^2 x} + \frac{\partial^2 \psi}{\partial^2 y} + \frac{\partial}{\partial z}\left(\frac{f_o^2}{N^2} \frac{\partial \psi}{\partial z} \right).$$

Equation 1.41

The geostrophic stream-function is given by $\psi \equiv {}^{p}\!/_{f_o \rho_o}$, N is the buoyancy frequency and f_o is the Coriolis parameter defined in the center of the beta plane. Assuming uniform background flow with small amplitude and β-plane approximation $f(y) \approx f_o + \beta y$ disturbance produces stream function given by

$$\psi = -Uy + \psi'$$

Equation 1.42

where ψ' is perturbation geostrophic stream-function and U is the zonal background flow. Equation 1.41 becomes

$$\left(\frac{\partial}{\partial t} + U \frac{\partial}{\partial x} \right)\left(\frac{\partial^2 \psi}{\partial^2 x} + \frac{\partial^2 \psi}{\partial^2 y} + \frac{f_o^2}{N^2} \frac{\partial^2 \psi}{\partial z^2} \right) + \beta \frac{\partial \psi}{\partial x} = 0$$

Equation 1.43

The procedure for finding the solutions to Equation 1.43 is to consider the sinusoidal forms $\psi = \mathrm{Re}\left(\psi_o \exp\left[i\left(\omega t + kx + ly + mz\right)\right]\right)$ where k, l and m are zonal, meridional and vertical wavenumbers, ω is the angular velocity and ψ_o is the amplitude. This results in a dispersion relation given by

$$m^2 = \frac{N}{f_o}\left(\frac{\beta}{U - \left({}^{\omega}\!/_{k}\right)} - \left(k^2 + l^2\right) \right)$$

Equation 1.44

If $\beta > 0$ the zonal phase speed of the wave c is given by

$$c = \frac{\omega}{k} = U - \frac{\beta}{k^2 + l^2 + f_n^2 m^2 / N^2} \qquad \Rightarrow \qquad U - c = \frac{\beta}{k^2 + l^2 + f_n^2 m^2 / N^2}$$

which satisfies the condition $U - c > 0$ and this implies that the planetary wave always propagates westward with respect to the background mean flow. For a wave to propagate upward m^2 must be greater than zero and thus m must be real and non-zero. Based on the analytical calculations given by Charney and Drazin (1961), waves propagating upward should satisfy $0 < U - c < U_c \quad \Rightarrow \quad 0 < U < U_c$, where for stationary waves c is zero and U_c is a critical speed always with a positive value which is determined by wave numbers as well as parameters of atmospheric medium.

1.3 Coupling between neutral atmosphere and ionosphere

Atmospheric waves (gravity waves, tides and planetary waves) excited in the lower regions of the atmosphere propagate upward and their amplitude grow exponentially. At altitudes around 80-120 km dissipation becomes important, causing these waves to be convectively unstable and break. Under certain atmospheric conditions, gravity waves and tides may penetrate to the ionosphere while planetary waves cannot penetrate to altitudes above 100-110 km (Lastovicka et al., 2003). However planetary wave type oscillations (PWTO) with period range (2-30 days) are observed in the ionosphere (Pancheva et al., 2002) indicative of neutral atmosphere-ionosphere coupling. Possible mechanism responsible for such coupling is modulation of gravity waves and tides at planetary wave periods such that when gravity waves and tides reach the ionosphere they transfer planetary wave signature (Pancheva et al., 2002, 2006). This study concentrates on tidal modulation because 1 hour sampling period of wind velocity (used in this study) is too long to capture short period gravity wave activity. Neutral winds driven by tides moves ionospheric plasma through magnetic field thereby creating ionospheric electrodynamic effect. The theory of ionospheric electrodynamic effect, hereafter called the ionospheric dynamo effect is now discussed.

1.3.1 Ionospheric dynamo effect

In this subsection a brief summary on the aspect of ionospheric dynamo effect is given, however a detailed discussion is given by e.g. Rishbeth (1997); Richmond and Thayer (2000); Paschmann et al. (2000); Heelis (2004). The ionosphere is a charged region of the atmosphere consisting of ions and electrons. Upward propagating atmospheric waves reaching the ionosphere induce a force that causes relative motion between ions and electron which then generates electric field and current. Current density ($\bar{j}$) can be expressed in terms of particle motion or ionospheric Ohm's Law as:

$$\bar{j} = N_i e(\bar{V}_i - \bar{V}_e) = \sigma_P \bar{E}_\perp + \sigma_\parallel \bar{E}_\parallel - \sigma_H \bar{E}_\perp \times \hat{b}$$

Equation 1.45

where N_i is the number density of ions, e is an electron charge, $\bar{V}_i, \bar{V}_e$ are drift velocities of ions and electrons, $\bar{E}_\perp, \bar{E}_\parallel$ are perpendicular and parallel components of the electric field, $\hat{b}$ is a unit vector along the magnetic field, σ_P, σ_H and $\sigma_\parallel$ are Pedersen conductivity along $\bar{E}_\perp$, Hall conductivity along $\bar{E}_\perp \times \hat{b}$ and field aligned conductivity along the magnetic field. The conductivity defines component of current with respect to electric and magnetic fields and can be derived from motion of each particle under the influence of magnetic and electric fields. These conductivities are given by:

$$\sigma_\parallel = \frac{Ne^2}{m_e s_e} + \frac{Ne^2}{m_i s_i} \approx \frac{Ne^2}{m_e s_e},$$

$$\sigma_P = Ne^2 \left[\frac{1}{m_e} \frac{s_e}{(s_e^2 + \Omega_e^2)} + \frac{1}{m_i} \frac{s_i}{(s_i^2 + \Omega_i^2)} \approx \frac{Ne^2}{m_i} \frac{s_i}{(s_i^2 + \Omega_i^2)} \right],$$

$$\sigma_H = Ne^2 \left[\frac{1}{m_e} \frac{\Omega_e}{(s_e^2 + \Omega_e^2)} + \frac{1}{m_i} \frac{\Omega_i}{(s_i^2 + \Omega_i^2)} \right].$$

Equation 1.46

Most of the variables are as indicated earlier, while m, s, e and $\Omega = eB/m$ are mass, collision frequency (subscript *i* and *e* stands for ion and electron), electron charge and gyrofrequency. The height variation of the field aligned, Pedersen and Hall conductivities is presented in Figure 1.3. The conductivity depends on electron density and collision frequency between charged and neutral particle. In the E-region and F-region the ratio of the collision frequency to gyrofrequency for the electron is very much less than 1, that is $(s/\Omega)_e << 1$ implying that $s_e << \Omega_e$ while for the ions $(s/\Omega)_i \approx 2$ in the E-region and $(s/\Omega)_i \approx 1/300$ in the F-region (Rishbeth 1997). Thus, the Hall and Pedersen conductivities are highest in E-region and they are also comparable as shown in Figure 1.3, however above this region atmospheric density and $(s/\Omega)_i$ decrease and so does the Hall and Pedersen conductivities, with the Hall conductivity decreasing at a higher rate. In the E- region and above the electrons are frozen in the magnetic

field and this result in a minimal collision frequency (s_e) and thus $\sigma_{\parallel}$ (from Equation 1.46) becomes large. Moreover, charged particles move along the magnetic field and not across it, therefore field aligned conductivity becomes very much greater than Hall and Pedersen conductivities as shown in Figure 1.3.

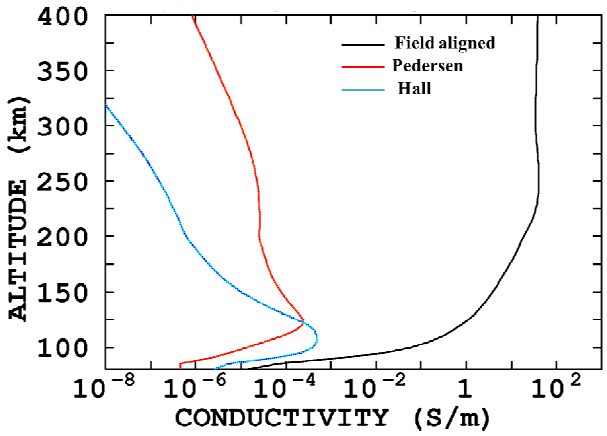

Figure 1.3: The daytime height variation of field aligned, Pedersen and Hall conductivities. Modified version from http://wdc.kugi.kyoto-u.ac.jp/ionocond/exp/icexp.html.

E-region has a narrow altitude range and if it is assumed that wind does not vary much with altitude in the F-region, thin-sheet approximation of the E- and F-region is assumed valid. Using these simplifications and other considerations outlined in Heelis (2004), the wind dynamo equation can be contracted from ionospheric Ohm's Law as

$$\nabla_{\perp} \bullet \sum \overline{E} + \nabla_{\perp} \bullet \sum \left(\overline{U} \times \overline{B} \right) = J_b^{\parallel} - J_a^{\parallel}$$

Equation 1.47

where $\sum$ is the flux integrated field aligned conductivity and $J^{\parallel}$ is the component of current from point *a* to *b* along the magnetic field. The dynamo equation describes electric field and current induced by neutral winds which are driven by atmospheric waves originated from the lower regions of the atmosphere. The induced electric field and current generate perturbations in the earth's magnetic field that can be detected by ground-based magnetometers. This process describes the ionospheric electrodynamo effect that will be used to explain the neutral atmosphere-ionosphere coupling mechanism.

1.4 Thesis outline

In this work, dynamics of the MLT region caused by atmospheric tides and planetary waves observed in the Southern hemisphere using the SuperDARN HF radars located at Halley, SANAE and Syowa are presented. The coupling effect between neutral atmosphere and ionosphere was studied using magnetic field data recorded by SANAE magnetometer as well as wind data also recorded from SANAE. The description of instruments used to record the data which was utilized in this study as well as the data analysis techniques including Fourier transform, wavelet transform, analytic signal and bispectrum, used to analyse the data are described in chapters 3 and 2 respectively.

The climatology of tides observed at Halley, SANAE and Syowa is presented in Chapter 4. In this chapter, the variability of tidal amplitudes at timescales ranging from 1 year to 11 years was investigated using wind velocity data recorded from 1998 to 2007. In particular, seasonal, quasi-biennial, ~5-year and 11-year solar cycle periodicities were investigated. Forcing mechanisms responsible for such oscillations are also investigated.

Chapter 5 presents a study on the variability of semidiurnal tidal amplitude before and just after the 2002 sudden stratospheric warming (SSW) event in the southern hemisphere. The forcing mechanism and nonlinear interaction between the SDT and planetary waves were investigated as the possible sources of the semidiurnal tidal variation.

A case study on the investigation of in-situ non-linear interaction between semidiurnal tides and planetary waves in the Southern hemisphere and the connection between the variability of the tidal wave observed in the MLT region and this process were presented in Chapter 6. For this analysis wind velocity data recoded by the MF radar located at Rothera was used.

Chapter 7 presents investigation of the coupling effect between the neutral atmospheres and ionosphere through upward propagating planetary wave type oscillations. For this study wind velocity data recorded prior to the 2002 SSW event and magnetic field data both recorded at SANAE were used. Possible magnetospheric and solar effects on the ionosphere were also investigated. The, summary and conclusion is presented in Chapter 8.

2 Data Analysis Techniques

2.1 Introduction

This chapter provides a theoretic review of data analysis techniques used to investigate numerous aspects as presented in the results sections. The techniques presented in this chapter builds on from my master's degree dissertation (Mthembu, 2007). These techniques include Fourier analysis, Wavelet analysis, High Order Spectrum and analytical signal. For an investigation of frequency content of a time series, Fourier transform is a suitable technique. But, when temporal evolution of a particular spectral component is required, a superior technique such as wavelet transform has to be used. Time variation of particular spectral component is investigated using the analytic signal. Lastly, for an investigation of nonlinear interaction between waves, high order spectrum is used. Further explanation on the application of these techniques is provided under relevant sections, however their theoretical aspect is detailed here.

2.2 Fourier transform

In most spectral analysis the first piece of information that is required is the frequency content of a signal and this can be obtained using Fourier transform (FT). This technique investigates the frequency content of the signal by actually decomposing it into sinusoids of different frequencies which add to an original signal. Brook and Wynne (1998) defined the Fourier transform of a signal $x(t)$ as

$$X_f = \int_{-\infty}^{\infty} x(t) e^{-i2\pi ft} dt$$

Equation 2.1

and the inverse Fourier transform as

$$x_t = \frac{1}{2\pi} \int_{-\infty}^{\infty} X(f) e^{i2\pi ft} df$$

Equation 2.2

Fourier power spectrum is then given by

$$P_f = |X_f|^2$$

Equation 2.3

For spectral components to be comparable to each other and to the transforms of other time series, the Fourier power transform need to be normalized. Therefore the normalized Fourier power spectrum is given by

$$P_{Nf} = \frac{N}{2}\frac{|X_f|^2}{\sigma^2}$$

Equation 2.4

where N is the number of points and σ^2 is the variance of time series given by $\sigma^2 = \frac{\sum_{t=0}^{t=N} x_t^2}{N}$.

Some peaks in the power spectrum indicate true features but some are caused by random processes. A significance test is normally used to make a distinction between the two sets of peaks. The significance of a peak in a power spectrum is tested by first choosing an appropriate background spectrum which could be white noise with a flat Fourier spectrum or red noise with power increasing with decreasing frequency. The red noise can be represented by $x_n = \alpha x_{n-1} + z_n$ where α in the assumed lag-1 autocorrelation, z_n is taken from Gaussian noise and $x = 0$ (Torrence an Compo, 1998). According to Gilman et al. (1963) the discrete Fourier power spectrum of the red noise is given by

$$P_k = \frac{1-\alpha^2}{1+\alpha^2-2\alpha\cos(2\pi k/N)}$$

Equation 2.5

If $\alpha = 0$ Equation 2.5 gives the discrete Fourier power spectrum of the white noise. Assuming that the red noise in normally distributed and knowing that the square of the normally distributed function is chi-square distributed with one degree of freedom (DOF), $|X_f|^2$ is chi-square distributed with two DOFs (Jenkins and Watts 1968). For example, to determine a 95% confidence level, the Fourier power spectrum is multiplied by a 95th percentile value for chi-square for two DOFs and thus the confidence level is given by

$$P_{ck} = \frac{1}{2} P_k \chi_2^2$$

Equation 2.6

where χ_2^2 is a chi-square distribution with two DOFs. Therefore any peak below this power is considered to be result of random noise while that above this power is considered to be significant with a certain percentage of confidence (e.g. 95%).

Fourier transform reveals spectral components within an entire signal, however, the technique fails to indicate the time of occurrence of a particular component. This poses a limitation to the technique i.e. it becomes applicable only in an investigation of stationary signals. Other techniques such as Short-Time Fourier Transform and wavelet transform can be used to analyse non-stationary signals and are discussed in Sections 2.3 and 2.4 respectively.

2.3 Short Time Fourier transform

One of the techniques that is able to overcome the above mentioned limitation of the Fourier transform is the Short-Term Fourier Transform (STFT). The STFT is able to analyse the signals with spectral components that vary with time owing to its ability to divide the signal into smaller segments which are assumed to be stationary. The segmentation process can be achieved by multiplying the signal with the window function of a fixed length. Ideally, the window length should be to an extent to which an assumption of stationarity reasonably holds given prevailing physical factors and conditions (Polikar, 2002).

In the computation of the STFT, the FT is applied on the windowed signal and the window is then advanced in time. This process is repeated until the end of the signal. The equation which summarizes the whole procedure is given by

$$STFT(t', f) = \int_t \left[x(t) \bullet W^*(t - t') \right] e^{-j2\pi ft} dt$$

Equation 2.7

where $x(t)$ is the signal being analysed, $W(t)$ is the window function and * denotes a complex conjugate. This operation results in the time-frequency representation of the signal which shows frequency components that are present in the signal and their better approximated times of occurrence. The length of the window function determines the precision of the time-frequency

representation. The FT yields a good frequency resolution and absolutely no time resolution because the window function covers the whole signal. In STFT, the narrow window results in a better time localization of a spectral component, but this is at the expense of the frequency resolution. Basically there is a trade-off between the time localization and the frequency resolution in a sense that a good time-frequency representation of the signal can be achieved by using a narrow window when looking for high frequency and vice versa. The problem with this technique is that once the window length has been chosen, it is consistently used for extraction of all frequency components. To manage this challenge, a technique is needed with a window function that is adaptive to the frequency that is being analysed.

2.4 Wavelet Analysis

A suitable technique to circumvent the problem in the STFT is the Wavelet transform. Wavelet transform is superior to STFT in a sense that a length of the window function is variable and thus can analyse both high and low frequency components. More details are discussed in Section 2.4.3, but for now the background theory of wavelet analysis are presented.

2.4.1 Wavelet

The wavelet is a waveform that is effectively limited in duration and its average value is zero (Misiti et al., 1996). This term is used to describe the set of functions $\psi_{ab}(t)$ that are deduced from shifted and dilated or scaled version of the mother wavelet or basic wavelet given by $\psi(t)$. The mother wavelet is defined as the prototype for the generation of other wavelets. There are different types of mother wavelets that can be used, which include among others, the Morlet, Paul, and DOG wavelets (Torrence and Compo, 1998). In this analysis the Morlet wavelet transform was as it is widely accepted in the scientific community, and has been used by a number of researchers for investigating the spectral content of time series (Malinga and Ruohoniemi, 2007; Pancheva and Mitchell, 2004).

2.4.2 Continuous wavelet transform

The continuous wavelet transform (CWT) of the signal $x(t)$ is defined as a sum over time of the signal multiplied by the scaled and shifted wavelet and mathematically it is given by (Torrence and Compo, 1998)

$$WT(\tau,s)=\frac{1}{\sqrt{|s|}}\int x(t)\,\psi^{*}\left(\frac{t-\tau}{s}\right)dt$$

Equation 2.8

where $\psi\left(\frac{t-\tau}{s}\right)$ are the wavelet basis functions, * indicates a complex conjugate, s is the scale and τ is the translation. The scale parameter scales the function by dilating or compressing it. The scale parameter and the frequency are inversely related and the constant of proportionality is not the same for each wavelet. The proportionality constant can be deduced by finding a wavelet power spectrum of a cosine signal of known frequency and finding the scale of the largest power (Malinga, 2001). Then a ratio between the scale and the frequency of the cosine gives the proportionality constant. The translation parameter is related to time information and it gives the position of the wavelet as it is shifted along the signal.

The results of Equation 2.8 are the wavelet coefficients (*WT)* which depend on the s and τ . *WT* gives the degree of correlation between the wavelet and the portion of the signal around τ . If the wavelet closely resembles the portion of the signal, the value of *WT* is high and if not then the WT is small (Malinga, 2001). Once the *WT* is deduced, the wavelet power spectrum can be calculated according to Torrence and Compo (1998)

$$WP(s,\tau)=|WT(s,\tau)|^{2}$$

Equation 2.9

and the corresponding phase is given by (Torrence and Compo, 1998)

$$\phi(s,\tau)=\arctan\left[\frac{\mathrm{Im}\left(WT(s,\tau)\right)}{\mathrm{Re}\left(WT(s,\tau)\right)}\right]$$

Equation 2.10

In order to compare the wavelet power spectrum to other spectra, normalization becomes necessary. For white noise time series, normalized wavelet power spectrum is given by

$$WP_{N}(s,\tau)=\frac{1}{\sigma^{2}}P(s,\tau)$$

Equation 2.11

The significance of the peaks in the wavelet power spectrum can be tested using the same method as that used in the Fourier transform. The appropriate background spectrum may also be given by white noise or red noise and its power spectrum is given Equation 2.5. If the Fourier coefficients are normally distributed, wavelet coefficients are also normally distributed since wavelet spectra follow Fourier spectrum (Torrence and Compo, 1998). If this is the case then the normalized wavelet power spectrum $WP_N(s,\tau)$ should be chi-squared (χ_2^2) distributed i.e. $WP_N(s,\tau) \Rightarrow \frac{1}{2} P_k \chi_2^2$. The 1/2 takes away a degree of freedom from χ_2^2 thus $WP_N(s,\tau) \Rightarrow P_k \chi_1^2$. For a particular confidence level for example 95%, $P_k \chi_1^2$ can be used to compute 95% confidence contour lines. Therefore any peak above this confidence contour line is considered a true feature while peaks below can be attributed to random processes.

2.4.3 Time-Frequency localization

The time-frequency localisation of the wavelet transform, which is based on the wavelets theory, is now discussed. The wavelet transform has a good time-frequency representation due to the fact that it has a variable 'window' function. It should be noted that the wavelet does not use a fixed window function as is the case in STFT. The 'window' refers to the wavelet which has a compact support (that is it has a finite length). It performs correlation and windowing at the same time. This can be illustrated using Figure 2.1 similar to the one used by Polikar (2002).

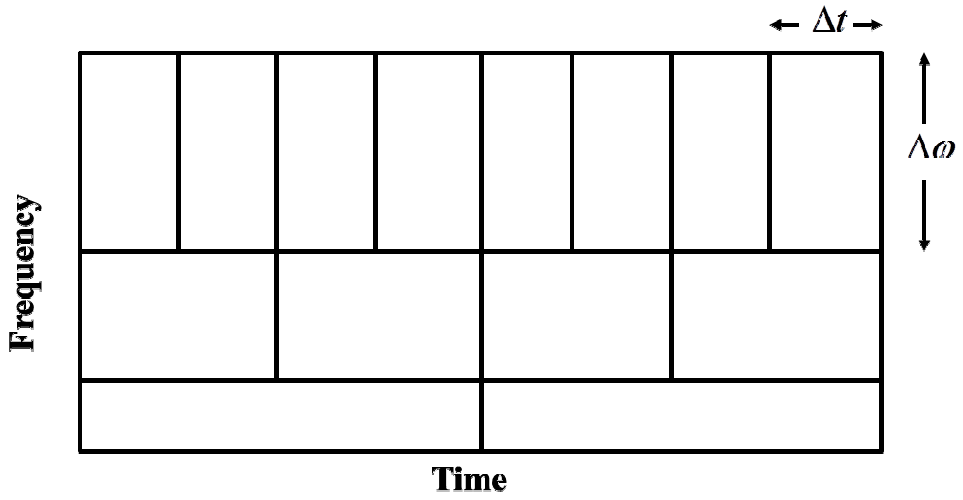

Figure 2.1: The vertical and horizontal dimensions of the figure represent frequency and time, respectively, where frequency increase upward and time to the right.

The horizontal dimension of each cell is Δt and the vertical dimension is $\Delta\omega$ and the area is given by $\Delta t\Delta\omega$. Although the dimensions of the cells change, the area is constant and represents a single value of the wavelet transform. For high frequencies (i.e. small scale) the horizontal dimension of the cells are shorter which correspond to shorter window length. In this case the signal is better resolved in time and poorly resolved in frequency. For low frequencies (large scale) the horizontal dimensions are longer which correspond to longer 'window' length. In this instance the signal is better resolved in frequency and poorly resolve in time. Wavelet analysis is designed to give good time resolution and poor frequency resolution at higher frequencies and vice versa.

2.5 Cross-spectral Density and cross wavelet transform

The cross-spectral density (CSD) uses the Fourier transform while cross wavelet transform uses the wavelet transform to quantify the frequency components that are common between two signals. For the CSD, consider two signals $x(t)$ and $y(t)$, with Fourier transforms given by $X(\omega)$ and $Y(\omega)$. Their corresponding CSD is given by

$$S_{xy} = \frac{X_n \times^* Y_n}{\omega_0} = A_{xy}(\omega)\exp\left[i\phi_{xy}(\omega)\right]$$

Equation 2.12

The cross-spectrum amplitude $A_{xy}(\omega)$ quantifies the average product of the amplitudes of the spectral components in $x(t)$ and $y(t)$ at a specific frequency *f* while the cross-spectrum phase quantifies the average value of the phase shift between spectral components of two signals at that frequency. This information can be used to find the time lag for a particular component *f* between two signals. The time lag can be given by

$$\Delta t = \frac{\Delta\varphi}{360^o \times f}$$

Equation 2.13

where $\Delta\varphi$ is the phase shift in degrees. The cross wavelet spectrum of two signals $x(t)$ and $y(t)$ on the other hand, is given by

$$W^{XY} = W^{X} W^{Y*}$$

Equation 2.14

where W^{X} and W^{Y} are wavelet transforms of $x(t)$, $y(t)$ and * denote a complex conjugate. The cross wavelet power spectrum is given by $|W^{XY}|$. The phase difference between spectral components in the time series $x(t)$ and $y(t)$ is given by a complex argument $\tan^{-1}(W^{XY})$ (Grinsted et al., 2004).

2.6 Analytic signal

The analytic signal of the real function *f(t)* can be defined as a complex function which is given by the sum of the function itself and its quadrature function (Bracewell, 1986). According to Smith (2003) the Hilbert transform can be considered as an ideal filter consisting of the amplitude of one, at all frequencies and an infinite bandwidth, that introduces a phase shift of $+90^{o}$ on the negative frequency components and phase shift of -90^{o} on the positive frequency components. The phase shift of $+90^{o}$ can be introduced by multiplying the negative frequency components by $e^{j\frac{\pi}{2}} = j$, and the phase shift of -90^{o} can be introduced by multiplying the positive frequency components by $e^{-j\frac{\pi}{2}} = -j$. The Hilbert transform which is given by *Hi(t)* is referred to as the quadrature function of *f(t).* Therefore the analytic signal is given by

$$AS(t) = f(t) + jHi(t)$$

Equation 2.15

In Figure 2.2 the function *f(t)* is plotted along the real axis and its quadrature function along the imaginary axis. The analytic signal is the complex function which is represented by a helix that has amplitude pitch slowly contracting and dilating. It can be considered as a phasor with a slowly varying length and phase. The length and phase of the phasor represents the instantaneous amplitude and phase respectively. The rate of change of the phase represents the instantaneous frequency.

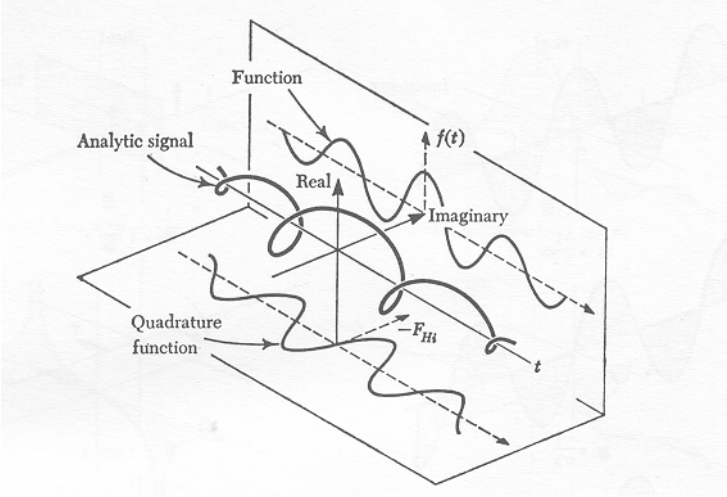

Figure 2.2: The function *f(t)* plotted along the real axis and the quadrature function F_{Hi} plotted along the imaginary axis (Bracewell, 1986).

The analytic signal is used to determine the time evolution of amplitude and phase of the selected frequency component of the signal. Since the method is applied on the quasi-monochromatic signals, the signals have to be filtered prior to the calculation of the analytic signal. To illustrate, consider a non-stationary process consisting of the signal $f(t)$ plus some noise given by

$$f(t) = \sum_{j=0}^{n-1} A_j(t)\, e^{+i\omega_j t} + \sum_{j=0}^{n-1} B_j(t)\, e^{-i\omega_j t}$$

Equation 2.16

where $A_j(t)$ and *B(t)* indicate a variation of amplitude while $\omega_j t$ indicate a variation phase of the j^{th} component with time. The signal is passed through a band-pass filter centered on the frequency component of interest ω_o and the filtered signal would be

$$f_f(t) = \sum_{j=k}^{l} A_j(t)\, e^{+i\omega_j t} + \sum_{j=k}^{l} B_j(t)\, e^{-i\omega_j t}$$

Equation 2.17

where k and l are the indexes corresponding to lowest and highest cut-off frequencies respectively.

The Hilbert transform of function $f_f(t)$ would be

$$Hi(t) = -i\sum_{j=k}^{l} A_j(t)\, e^{+i\omega_j t} + i\sum_{j=k}^{l} B_j(t)\, e^{-i\omega_j t}$$

Equation 2.18

Thus from Equation 2.15 the analytic signal is given by

$$\begin{aligned} \mathrm{AS}(t) &= \sum_{j=k}^{l} A_j(t)\, e^{+i\omega_j t} + \sum_{j=k}^{l} B_j(t)\, e^{-i\omega_j t} + i\left[-i\sum_{j=k}^{l} A_j(t)\, e^{+i\omega_j t} + i\sum_{j=k}^{l} B_j(t)\, e^{-i\omega_j t} \right] \\ &= \sum_{j=k}^{l} 2A_j(t)\, e^{+i\omega_j t} \end{aligned}$$

Equation 2.19

There is a gain of two at the positive frequency components and the negative frequency components are filtered out.

Having deduced the analytic signal, the variation of amplitude with time is given by

$$A(t) = \left| A_j(t) \right|$$

Equation 2.20

Particular care needs to be taken when extracting the phase information because of a $2n\pi$ ambiguity where *n* is an integer (Walker et al., 1992). The phase of the analytic signal is given by

$$\phi(t) = \omega_j t$$

Equation 2.21

The phase of the analytic signal has a 2π phase ambiguity which was rectified by adding multiples of 2π .Thereafter, the phase difference between the analytic signal and a pure sinusoid with central frequency ω_o is determined from the phase factor of Equation 2.22.

$$AS(t)\, e^{-i\omega_0 t} = \sum_{j=k}^{l} 2A_j(t)\, e^{+i\omega_j t}\, e^{-i\omega_0 t} = \sum_{j=k}^{l} 2A_j(t)\, e^{i(\omega_j - \omega_0)t}$$

Equation 2.22

where ω_0 is the central frequency of the filter.

Therefore the variation of phase with time is given by

$$\phi(t) = (\omega_j - \omega_0)t$$

Equation 2.23

The variation of the frequency with time can be evaluated from the rate of change of the phase, and the results yield

$$f_j(t) = \frac{\left(\frac{\partial \phi(t)}{\partial t} + \omega_0\right)}{2\pi}$$

Equation 2.24

2.7 High Order Spectra

A high order spectrum (HOS) is a technique that is used, among other things, to determine non-linear interaction between waves. Autocorrelation function and power spectrum are used to investigate the power in each spectral component while suppressing the phase information. However, HOS retains the phase information which then makes possible the detection and description of nonlinearities in the signals (Clark and Bergin 1997).

2.7.1 Bispectrum

Consider a real and random signal given by $x(t) = A_1 \cos(\omega_1 t + \phi_1) + A_2 \cos(\omega_2 t + \phi_2)$ and is passed through a quadratic non-linear system $Q(t) = ax^2(t)$ where a is a non-zero constant. The product will contain, among others, secondary components with frequencies and phases given by $(2\omega_1, 2\phi_1), (2\omega_2, 2\phi_2), (\omega_1 + \omega_2, \phi_1 + \phi_2)$ and $(\omega_1 - \omega_2, \phi_1 - \phi_2)$. The phenomenon that produced such phase and frequency relationship is called a quadratic phase coupling and indicates the occurrence of non-linear interaction between the primary waves.

Bispectrum is a two dimensional Fourier transform of a third order cumulant and it falls under the category of HOS, is used to detect the quadratic phase coupling. The bispectrum is computed by first dividing the time series into K segments with length M. Mathematically the bispectrum of the k^{th} segment is given by (Beard et al., 1999)

$$B_k(\omega_1,\omega_2)=\lim_{T\to\infty}\frac{1}{T}E\{X_k(\omega_1)X_k(\omega_2)X_k{}^*(\omega_1+\omega_2)\}$$

Equation 2.25

and in turn

$$X_k(\omega_1)X_k(\omega_2)X_k{}^*(\omega_1+\omega_2)=|X_k(\omega_1)||X_k(\omega_2)||X_k{}^*(\omega_1+\omega_2)|e^{j\phi(\omega_1,\omega_2)}$$

Equation 2.26

where $E\{\}$ is the expectation, T is the duration of the time series, $X(\omega)$ is the fast Fourier transform (FFT) of $x(t)$, * denote complex conjugate and $\phi(\omega_1,\omega_2)$ is known as the biphase and is given by $\phi(\omega_1,\omega_2)=\phi(\omega_1)+\phi(\omega_2)+\phi(\omega_1+\omega_2)$. Bispectrum is determined by computing 2-D FFT of each segment using Equation 2.25 and thereafter averaging across all segments. If spectral components within the segment have random phases, the bispectrum will be zero unless, there exists spectral components with frequencies ω_1,ω_2 and $\omega_1+\omega_2$ whose phases are coherent. This means, according to Beard et al. (1999), the bispectrum may not be zero provided that the phases of these components exhibit a quadratic phase coupling, i.e. there are spectral components with frequency and phase relationship given by $(\omega_1,\phi_1),(\omega_2,\phi_2)$ and $(\omega_1\pm\omega_2,\phi_1\pm\phi_2)$. So in essence, bispectrum is used to detect quadratic phase coupling.

Spectral components with large amplitudes but rather less coupled may overshadow highly coupled components with small amplitudes. In this case bicoherence, which is the normalized form of the bispectrum is used to determine quadratic phase coupling as it has the ability to exaggerate small but high coupled components.

Furthermore, one needs to be cautious when using bispectrum as a detector of the quadratic phase coupling which indicate non-linear interaction. Spontaneously excited waves have random phase, and thus, after averaging, yield zero bispectrum. However, it is possible that averaging may result in a non-zero bispectrum if the spontaneously excited waves have a phase relationship which is merely constant. In the atmospheric waves this phenomenon normally occurs during non-linear interaction among the tides alone as they have a similar source of excitation.

3 Instrumentation

A brief description of the instrumentation used to collect the data that for this study will follow. Mesospheric wind velocity data from the SuperDARN HF radar and the meteor radar were used to study the dynamics of the MLT region while the coupling effect between the neutral atmosphere and the ionosphere was studied using the magnetic field data recorded by the magnetometer at SANAE. HF and meteor radars deduce mesospheric winds using the reflected radio waves from meteor trails, thus a brief overview of the meteors will now be provided.

3.1 Meteors

A meteoroid is a small sized object that enters the Earth's atmosphere from outer space. These particles are actually debris from comets, asteroids and from the formation of planets and moons (Sandford 2008). A meteor on the other hand is a visible path of the meteoroid as it enters the Earth's atmosphere. The word 'meteors' was derived from the Greek word meaning 'things up in the air' and are sometime called 'falling stars'. They have been observed to move at the velocity range 12-72 km/s relative to the Earth's rotational speed and at an altitude range 75-100 km (Stober and Jacobi 2007). As the meteoroid travels through the atmosphere, friction with air particles cause sublimation, leaving a cylindrical trial of ionized ions and electrons called a meteor trial. After the meteor trails have formed, they get dissipated by, among other processes, ambipolar diffusion, turbulence and eddy diffusion. This diffusion causes the radial expansion of the meteor.

Transmitted signals from the radar are reflected off individual electrons of the trail through Thompson scattering. Backscattered signals from individual electrons consist of random phase but the alignment of electrons in the meteor trail introduces strong coherency in the signal (McKinley 1961). Since the transmitter and the receiver are at the same site, backscattered signals are received only if the trails are orientated perpendicular to the radio waves, which is a rare case. Thus a small fraction of the transmitted power is received by the radar since the trails which are not orientated perpendicularly reflect signals away from the radar. The number of reflected signals from different parts of the cross section of the trail contribute to the power of the back-scattered wave. Two types of meteor trails exist which are called underdense and overdense meteors and they are classified according to their electron density.

Underdense trails (with electron line density $\leq 10^{14}$ electron/m) are numerous and short-lived such that radio waves reflected from them last no more than few tenths of a second. The signal

from this trail is characterized by sudden increase in signal power that last for few hundredths of a second, followed by an exponential decay. The distinction between the backscatter from the underdense trail and other targets is made possible by the characteristic Lorentzian shape of power from the underdense signal shown in Figure 3.1. Consequently, most meteor radars record backscattered signals from underdense trails because of confidence that the reflected signal are from the meteor trails.

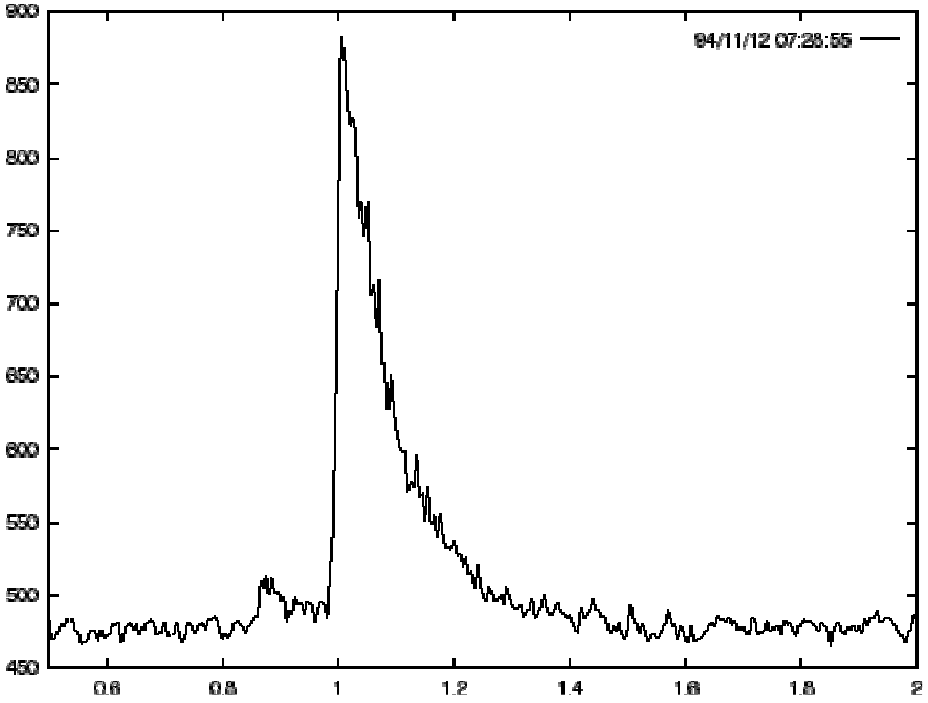

Figure 3.1: The power from the typical underdense meteor trail where the x-axis represents time while the Y axis represents power. Sourced from http://www.imo.net/radio/reflection.

In contrast, overdense meteor trails (with electron line density $\geq 10^{14}$ electron/m) are brighter, fewer and radio waves reflected from them can last longer. During this time the trail can suffer a severe distortion from atmospheric winds. This may result in unpredictable and irregular backscattered signals as shown in Figure 3.2. This is because backscattered signals are reflected even if the trail is no longer suitably orientated for specular reflection.

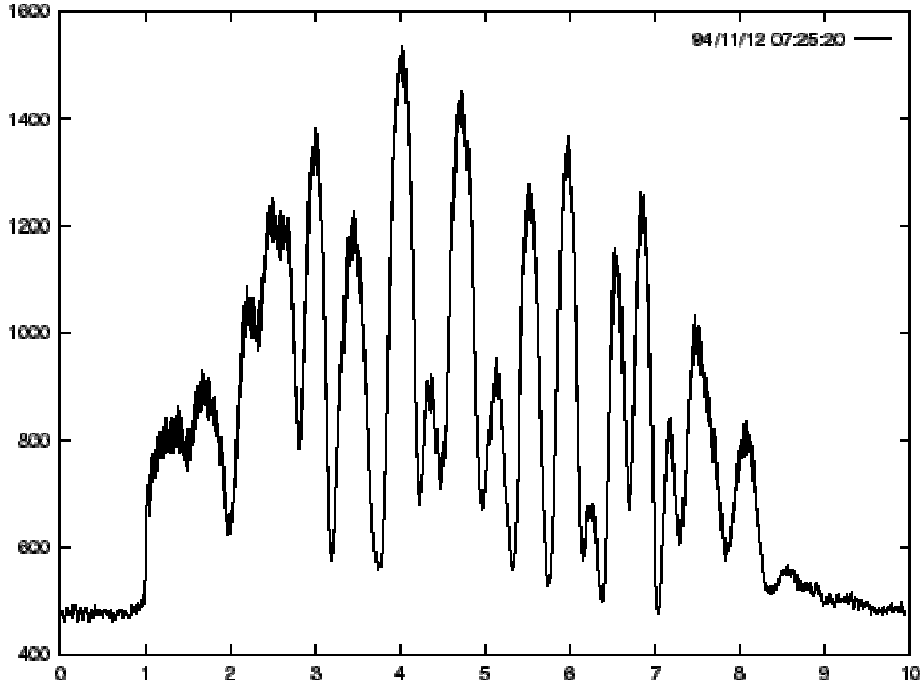

Figure 3.2: The power from the typical overdense meteor trail where the x-axis represents time while the Y axis represents power. Sourced from http://www.imo.net/radio/reflection.

The diurnal variation of meteors is characterized by maximum meteors at dawn and minimum at dusk. This variation is a consequence of a natural relative motion between the Earth and meteors. At dawn the radar detects all meteors i.e. those that are travelling slower and faster than the Earth's rotational speed. However, at dusk meteors have to catch up with the Earth's rotation to be detected, and consequently the radar will only detect meteors that are travelling faster than the Earth's rotational speed.

3.2 Meteor radar

The mesospheric wind velocity (zonal and meridional) data used to investigate in situ nonlinear interaction between semidiurnal tide and planetary wave were recorded from meteor radar located at Rothera (68S, 68W), Antarctica. The radar measures back-scattered echoes from meteor trails left by ablating meteors in the mesospheric region. A detailed description of operation of this radar can be found in Sandford (2008).

3.2.1 Brief description of the meteor Radar

The meteor radar is a commercially-produced SKYiMET meteor-radar system which consists of one 3-element Yagi transmitter and five 2-element receivers spaced so as to illuminate a larger

portion of the sky. A detailed technical description of this radar is given in Hocking et al. (2001). The transmitter is capable of producing a peak power of 6 kW at an operating frequency of 32.5 MHz. The receivers are spaced by 2 and half wavelengths and 2 wavelengths along two orthogonal axes and function as an interferometer. One of a typical receiver is shown in Figure 3.3.

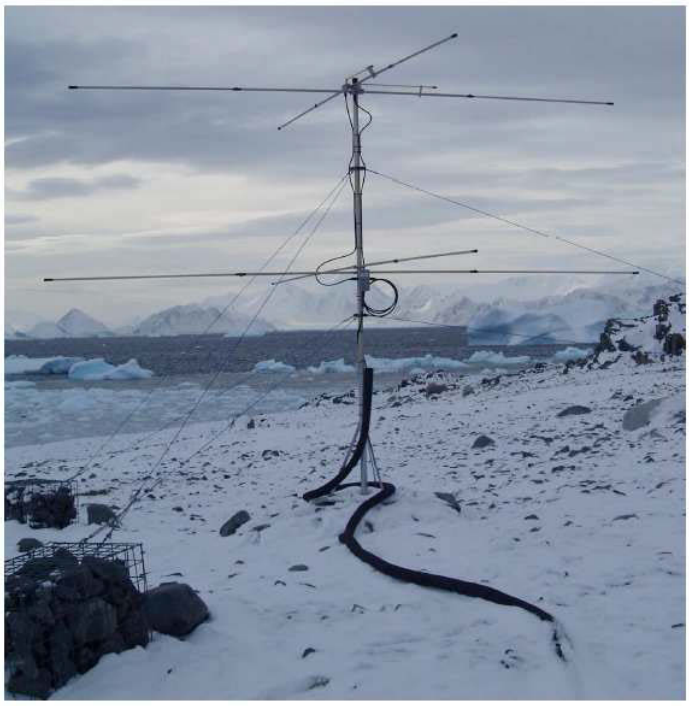

Figure 3.3: Picture of one of the meteor radar receivers. Sourced from Sandford (2008).

3.2.2 Observation and data

The height from which the back scattered radio waves are reflected can be determined using the information from the receivers. Using the phase difference between the echoes arriving at each receiver, the zenith and azimuthal angle of arrival can be determined. Using this information and the range information, the height of the meteor trail can be determined. This radar receives backscattered radio waves from six different altitudes centered at 80.4, 84.6, 87.5, 90.4, 93.4 and 97.6 km. Assuming that meteor trail drift with the wind, drift velocity of the meteor tail is then considered to be equal to that of the wind.

Using the Doppler shift frequency determined from the signals reaching the receivers, radial velocity can be determined from

$$V_{rad} = \frac{\Delta f c}{f}$$

Equation 3.1

where Δf is the Doppler shift frequency, c is the speed of light and f is the radar operating frequency. The zenith angle and the radial velocity are then used to determine the horizontal component of the velocity from

$$V_H = V_{rad} \sin \varphi$$

Equation 3.2

where φ is the zenith angle. The azimuthal and horizontal component of the drift velocity are fitted using least-square fit to determine the zonal and meridional wind velocities (Sandford et al., 2010).

3.3 SuperDARN HF radar

Having discussed the meteor radar, discussion on the Super Dual Auroral Radar Network (SuperDARN) HF radars is given here. This is a collaborative network of HF radars that monitor the ionospheric plasma convection over the Northern and Southern polar regions. A detailed description of these instruments is presented by e.g. Greenwald et al. (1995); Hall et al. (1997).

3.3.1 Brief description of the HF radar

The original design of the SuperDARN HF radar antenna array at SANAE consisted of 16 booms each supporting a log-periodic antenna (Greenwald et al., 1995). These structures were unfortunately taken down by a storm in 2008. In the newly designed antenna arrays installed at SANAE shown in Figure 3.4, the antenna section of folded dipole is supported by linear poles with reduced surface area and hence better tolerance to wind storms. Signals from these antennas are phased using an electronically-controlled time-delay element that allows the beam to be steered in 16 directions. The width of each beam depends on the radar operating frequency, and ranges from 2.5^o at 20 MHz to 6^o at 8 MHz. The nominal sector covered by one complete scan of the HF radar is about 52^o. The dwelling time of the beam in one direction is about 6 s resulting in a time resolution of one complete scan to be just under two minutes and

the field of view being approximately 2000×2000 km^2. The analysis of the returned signal from the irregularities allow the determination of line of sight Doppler velocity, backscatter power, and spectral width as shown in Figure 3.5 for up to 75 range gates along each beam where each range gate is equal to 45 km. This implies that the measurement can be made from about 180 km to more than 3000 km in range.

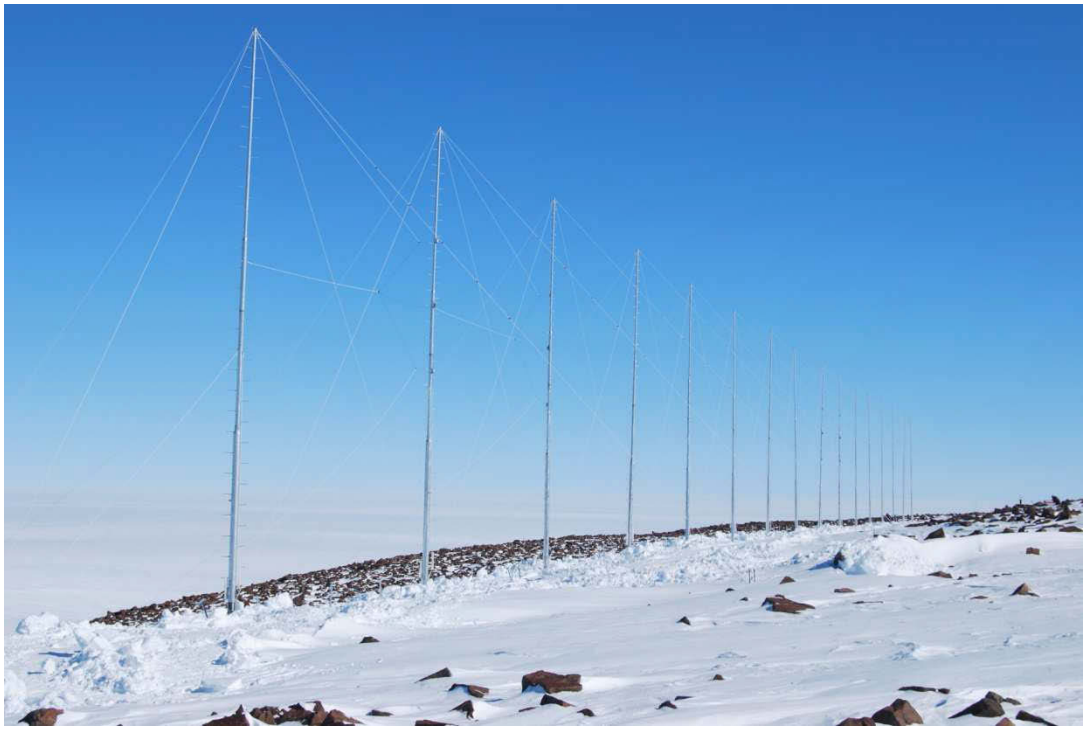

Figure 3.4: A new design of the SuperDARN HF radar at SANAE erected in 2009.

3.3.2 Data acquisition

The operation of the SuperDARN HF radars is controlled according to a protocol signed by representatives of all radars and the terms of the protocol are explained in Walker (2002); Mthembu (2007). The SuperDARN HF radars use a variety of multipulse transmission sequences consisting of 5 to 7 pulses transmitted over a 100 ms interval (Greenwald et al., 1995). The return signal from the irregularities is sampled and processed to produce multilag autocorrelation functions (ACF's) as a function of range. Walker (2002) has explained in more detail how the ACF's are calculated. The ACF's are fitted to determine the backscatter power, the line of sight Doppler velocity and the spectral width for each range for which there are significant returns.

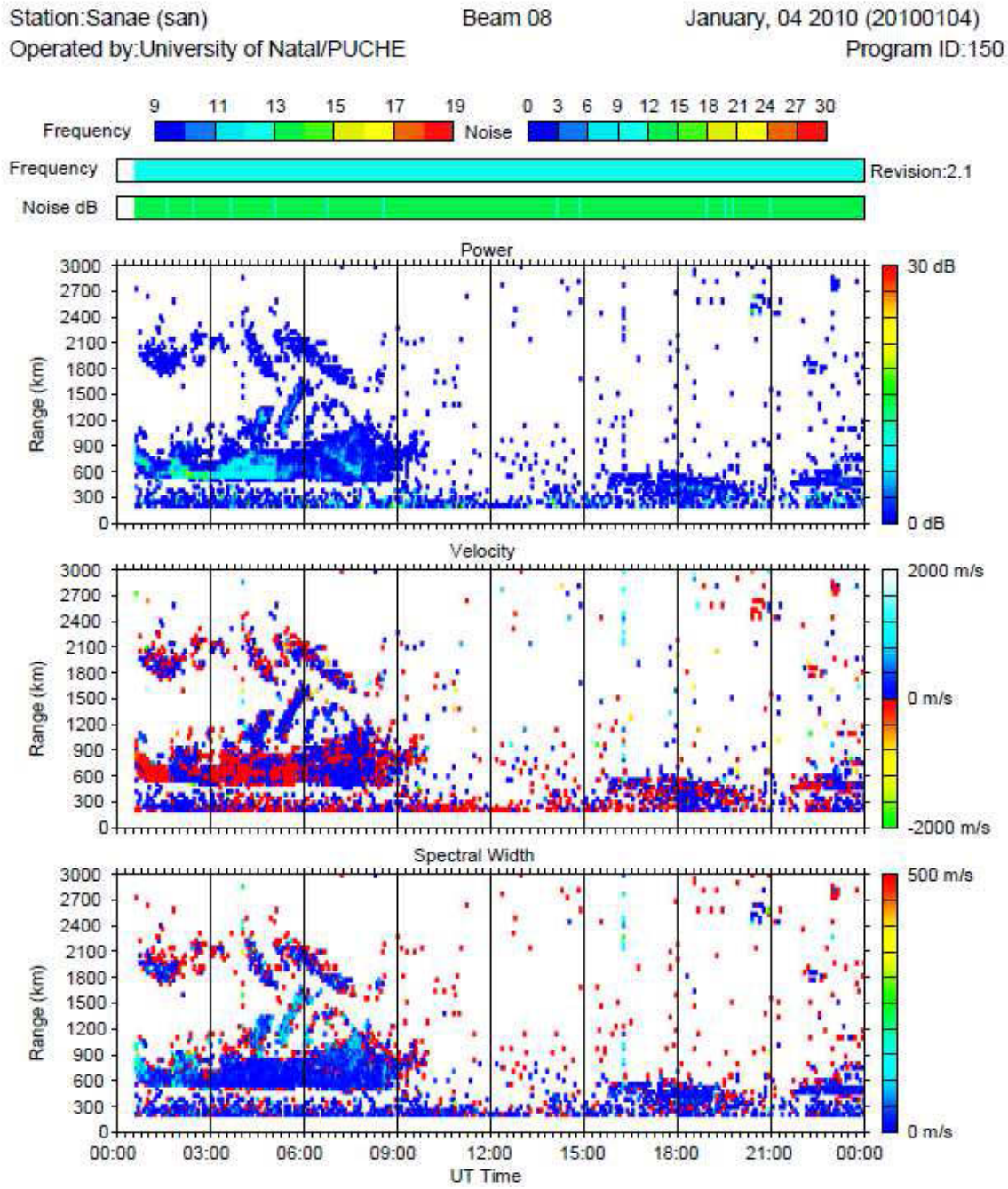

Figure 3.5: Summary plot of the backscatter power, line of sight Doppler velocity and the spectral width produced from the data received from SANAE HF radar located at Antarctica. Obtained from http://superdarn.jhuapl.edu/index.html.

SuperDARN HF radars were primarily used to study plasma irregularities in the *E* and *F* regions of the ionosphere. However Hall el al. (1997) discovered that these radars can also be used to measure neutral atmospheric winds in the MLT region. They identified that the HF radars receive near (< 500 km) range echoes which have a 'grainy' appearance as shown in Figure 3.5. They later referred to these echoes as 'grainy near-range echoes' (GNRE) and attributed them to

meteor trails. A Doppler shift of the echoes are used to deduce the speed of the meteor trails which is then considered as the speed of the neutral wind since the trail drifts with the neutral wind. HF radars are unable to determine the height at which the backscatter echoes are reflected, thus a nominal height of about 90-95 km is assumed because most meteors are observed approximately at these altitudes (e.g. Nakamura et al., 1991; Hussey et al., 2000; Sandford et al., 2010). The horizontal components of the mesospheric winds are derived from the line of sight Doppler velocity exploiting its ranging and azimuthal scanning property. The meridional component of the winds is estimated by calculating the weighted average of the velocity from the beams that point mostly towards the geographic pole. The zonal component, is estimated by applying the beam-swinging algorithm to the horizontal component of the winds (Matthews et al., 2006).

To optimize accuracy of estimated winds, meteor detection rate should be enhanced but yet reducing as much as possible back scattered echoes that are not from meteor trails. As the SuperDARN HF radars were originally designed to measure ionospheric irregularities (Greenwald et al., 1995), ionospheric echoes are present in the back scattered echoes. Therefore a criterion used to minimize such echoes is to restrict back scattered echoes to those from near range gates. Matthews et al. (2006) investigated the dependance of the radar's sensitivity to meteor echoes by variying the operating frequency from 9 to 20 MHz. It was discovered that the meteor detection rate is enhanced as the frequency decreases. This is due to the fact that decrease in operating frequency results in an increase in beam width and hence large volume and more meteors will be sampled. The SuperDARN HF radars mostly samples underdense meteor echoes which have a power spectrum that is Lorentzian. Thus using the SuperDARN fitting model, which is also Lorentzian, results in a good estimate of the spectral width given by

$$\Delta v = \frac{\lambda}{4\pi\tau}$$

Equation 3.3

where λ is the radar wavelength and τ is the exponential decay constant which is in turn given by

$$\tau = \frac{\lambda^2}{32\pi D^2}$$

Equation 3.4

and D is the diffusion coefficient. Therefore the spectral width is also dependent on the decay constant. As a result the spectral width from underdense meteors is supposed to be limited to a certain narrow range. Thus this parameter is used to reject echoes that are from the near range gates but not back scattered from the meteor trails.

3.4 Fluxgate magnetometer

In the study on coupling effect between the neutral atmosphere and the ionosphere, magnetic field data recorded by fluxgate magnetometer was used as an ionospheric parameter. Wilson (2000) described fluxgate magnetometer in more detail and a brief description of the instrument will follow.

3.4.1 Description

A pictorial representation of fluxgate magnetometer is shown in Figure 3.6. It consists of a sensor which detects and then coverts small perturbations of magnetic field into a measurable signal. The sensor consists of small magnetically susceptible cores wrapped by two coils of wire whose direction is reversed i.e. the primary coils. The secondary coil surrounds the two cores and the primary coils. If an alternating current (AC) is passed through the primary coils, it causes a large varying magnetic field in each of the primary coils. The induced magnetic fields produce a voltage in the secondary coil. However if there is no external field the voltage detected in the secondary coil would be zero because the magnetic fields generated in the two cores have the same strength but are in opposite directions. In the presence of an external field the behaviour in the two cores differs by an amount which depends on the external field. Thus, fluxgate magnetometer measures the strength of any component of the Earth's magnetic field which is orientated parallel to the cores of the instrument.

Figure 3.6: The fluxgate magnetometer installed at SANAE, sourced from Wilson (2000).

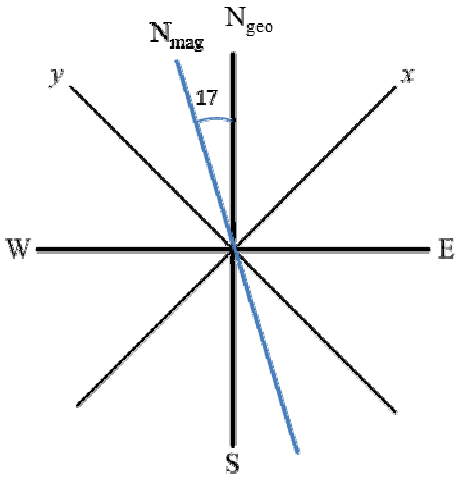

Figure 3.7: Geographic coordinate system and flux gate direction that represent the *x*- and *y*-component of the magnetic field. N_{mag} and N_{geo} indicate magnetic and geographic north respectively. Modified version sourced from Wilson (2000).

3.4.2 Geomagnetic Coordinate System

The fluxgate magnetometer has three sensors; one records the vertical *z*-component of the Earth's magnetic field. The other two sensors measure the *x*- and *y*-components of the field Wilson (2000). The *x*-component of the sensor is not aligned with the geographic north direction, but instead the *x*- and *y*-components are aligned 45° with respect to magnetic north which is in turn 17.223° west of geographic north as shown in Figure 3.7. This was done by rotating the sensor until the same output was obtained from the two sensors. As a result the

components of the magnetic field have only positive values which are convenient for electronic archiving.

4 Studies on long-term variation of atmospheric tides using Southern hemisphere SuperDARN HF radars

4.1 Introduction

The mesosphere-lower thermosphere (MLT) is the region which is very dynamic due to the influence of atmospheric waves including gravity waves, tides and planetary waves that are excited in the lower regions of the atmosphere. The present study concentrates on the MLT dynamics caused by the atmospheric thermal tides. This class of tidal waves is excited through the absorption of ultraviolet radiation by ozone in the mesosphere and stratosphere with periods that are harmonics of a solar day i.e. 6, 8, 12 and 24 h (Zhang et al. 2001). Upon excitation tidal waves propagate upward and their amplitude grows exponentially due to decrease in atmospheric density. Theoretical and observational studies (Sprenger and Schminder, 1969; Dartt et al., 1983; Greisiger et al., 1987; Fraser et al., 1989; Namboothiri et al., 1994; Bremer et al., 1997; Jacobi et al., 1997; Baumgaertner et al., 2005; Hagan et al., 1999; Labitzke, 2005; Iimura et al., 2010; Iimura et al., 2011) have shown that tidal amplitudes are further modulated by numerous mechanisms which result in the variation of tidal amplitudes at periods ranging from few days to several years. In the present study, the emphasis is on the annual as well as inter-annual variations of tidal amplitudes observed in the Southern hemisphere high latitude region.

A substantial amount of work has been done on the investigation of annual variation of tides in the northern and Southern hemisphere high latitude region (Portnyagin et al., 1993a, b; 2004, 1998; Burrage et al., 1995; Baumgaertner et al., 2005; Fraser et al., 1995; Hibbins et al., 2006; 2007, Hibbins and Jarvis, 2008; Riggin et al., 1999, 2003). Portnyagin et al. (1993a, b, 1998) investigated the variation of semidiurnal tide (SDT) at the South Pole and Scott base and their results showed maximum amplitude during summer and minimum during winter. Confirmation of these results was provided by Riggin et al. (1999) using MF radar data between 80 and 98 km at McMurdo and by Hibbins et al. (2006) at Halley using an imaging Doppler interferometer (IDI) data between 90 and 95 km. An investigation by Burrage et al. (1995) reported an autumn enhancement of SDT amplitude from satellite measurements and attributed this to migrating SDT. The enhancement was observed to be accompanied by a dramatic shortening of the vertical scale of the SDT which is in line with the refraction of the wave in the background wind. The results by Riggin et al. (2003) at approximately 86 km in the northern and southern

hemispheres and by Hibbins et al. (2007) from the MF radar data at Rothera (68°S, 68°W) also reported a fall equinox enhancement of the SDT amplitude.

Investigation of the seasonal variation of diurnal tides (DT) has been investigated by Fraser et al. (1995) using data from Mawson (68°S, 45°E) and Scott base (78°S, 168°E) at a height of 95 km. Their results show that the variation of DT amplitude is characterized by summer maximum and winter minimum. Similar results were also reported by Hibbins et al. (2006) using the IDI at Halley based on a comparative study of winds and tides measured by SuperDARN HF radar.

The long-term variations of tides that are commonly reported in the literature are those associated with quasi biennial oscillation (QBO) and 11-year oscillation. Based on the correlation analysis the tidal amplitude was found to be related to solar activity (e.g. Sprenger and Schminder, 1969; Dartt et al., 1983; Greisiger et al., 1987; Fraser et al., 1989; Bremer et al., 1997; Namboothiri et al., 1994; Baumgaertner et al., 2005). The results from earlier studies (Sprenger and Schminder, 1969; Dartt et al., 1983; Greisiger et al., 1987; Baumgaertner et al., 2005) reported a negative correlation between SDT amplitude and solar activity. A positive correlation was reported by Fraser et al. (1989) using the mid-latitude data from the southern and northern hemispheres. The results from Jacobi et al. (1997) using the same dataset as that used by Greisiger et al. (1987) but for different period showed no correlation between the tides and solar activity. Thus based on their results they proposed that correlation depends on the period of observation, moreover, longer datasets were proposed as suitable for this kind of investigation. A correlation analysis was also conducted by Iimura et al. (2011) using MF radars at Syowa and Andenes (69°N, 16°E). From their study, it was observed that the meridional component showed a negative correlation from ~ 88 km and above while positive correlation below 88 km was observed. Based on the above results, they concluded that correlation between tidal amplitudes and solar activity also depends on the height.

The phases of the QBO seem to have greater effect on the DT amplitude especially at lower latitudes. For example, Davis et al. (2013) investigated the variation of DT and SDT over Ascension Island (8°S, 14°W) and their results revealed a pronounced effect of QBO characterized by larger amplitudes of the DT during an eastward phase of the QBO. The numerical study by Hagan et al. (1999) also showed a significant effect of QBO on the MLT DT. Jarvis (1996) reported signatures of the QBO on the high latitude SDT while Baumgaertner et al. (2005) did not find any significant effect of QBO on the high latitude MLT wind and tides.

The long-term tendency of the tidal amplitude has previously been investigated by various researchers (Bremer et al., 1997; Merzlyakov and Portnyagin, 1999; Jacobi et al., 2005;

Portnyagin et al., 2006; Merzlyakov et al., 2009). However, earlier studies have been conducted using linear regression on entire datasets (e.g. Bremer et al., 1997; Merzlyakov and Portnyagin, 1999; Jacobi et al., 2005). The analysis conducted by Bremer et al. (1997) revealed a negative trend while the analysis conducted by Jacobi et al. (2005) on the same but later dataset revealed positive trend. Therefore this has led to the discovery of a new method (Portnyagin et al., 2006; Merzlyakov et al., 2009) which analyses the series of piecewise trends within the long dataset. This method can determine the break points and changes in both sign and strength of the trends.

Mbatha (2012) used wind velocity data from Halley and SANAE SuperDARN HF radars to study the seasonal behaviour of mean winds, climatology of planetary waves over SANAE and the coupling effect between the stratosphere and the MLT region. Detailed results from the study can be found in Mbatha (2012) but the summary of his findings were: The zonal winds were found to be mostly eastward with maximum occurring during solstice months. The meridional winds were found to be weaker than the zonal winds with stronger northward winds during October and March. The study also revealed summertime planetary wave activity with periods of approximately 5, 10 and 16 days and with zonal wavenumber of ± 3. The coupling effect between the stratosphere and the MLT region conducted with data from 2001 to 2003 revealed weaker planetary wave coupling while stronger planetary wave coupling was observed in 2002. The present study digresses and concentrates on the climatology of tides, particularly to the investigation of the long-term variability of tidal amplitudes at a timescale ranging from 1 year to 11 years.

A description of the data used and method of analysis is given in Section 4.2. Thereafter, the results are presented in three sections where Section 4.3.1 presents the seasonal variation of both amplitudes and phases of DT and SDT, Section 4.3.2 presents the inter-annual variation of DT and SDT at periods close to that of QBO and 11-year solar cycle and in Section 4.3.3, trend analysis is investigated. A summary of the results is presented in Section 4.4.

4.2 Data and method of analysis

The wind velocity data collected from the SuperDARN HF radars located at SANAE, Halley and Syowa were used in this study and Figure 4.1 shows the location and their fields of view. Due to poor quality of the data from Syowa South, the entire analysis in this thesis is conducted with data from Syowa East. The measurements of meteor winds are restricted to the near range gates, extending no further than 500 km from the radar. Although local effects play a role in the difference between the variations of tides at different locations, similarities are expected from

results on tides at SANAE and Halley because they are closer and their fields of view partially overlap. Figure 4.2 presents the data coverage recorded by the HF radars from 1998 to 2007. The amount of hourly wind velocity recorded at Halley, SANAE and Syowa for the above time period is 84%, 73% and 76%, respectively.

Daily values of the tidal amplitude and phase were computed using the dynamic Fourier transform applied to a 10-day data window which was progressively shifted forward by one day. For a computed spectrum, amplitude and phase corresponding to DT and SDT were selected and attributed to a "central day" taken to be day 5. This procedure was repeated until the end of the annual data which was padded at the beginning by five days' worth of data from the previous year and at the end by five days' worth of data from the following year. The data gaps shown in Figure 4.2 were linearly interpolated where the gap was not longer than 30% of corresponding 10-day data window. The monthly means were then computed using vector averages if there were more than 70% of the data in the particular month.

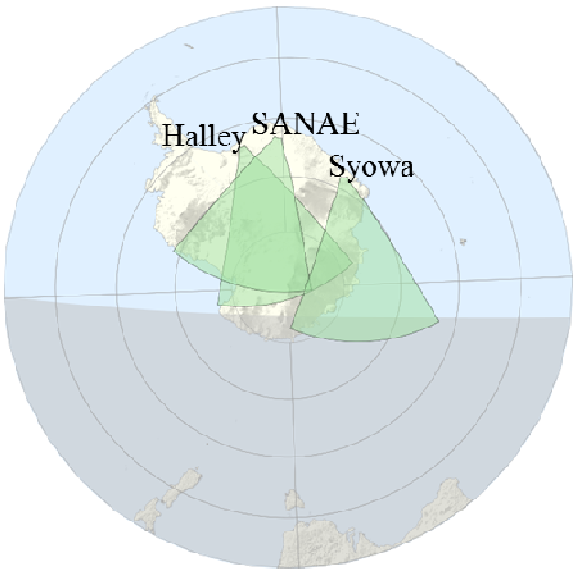

Figure 4.1: The geographical location and the field of view of the SuperDARN HF radars.

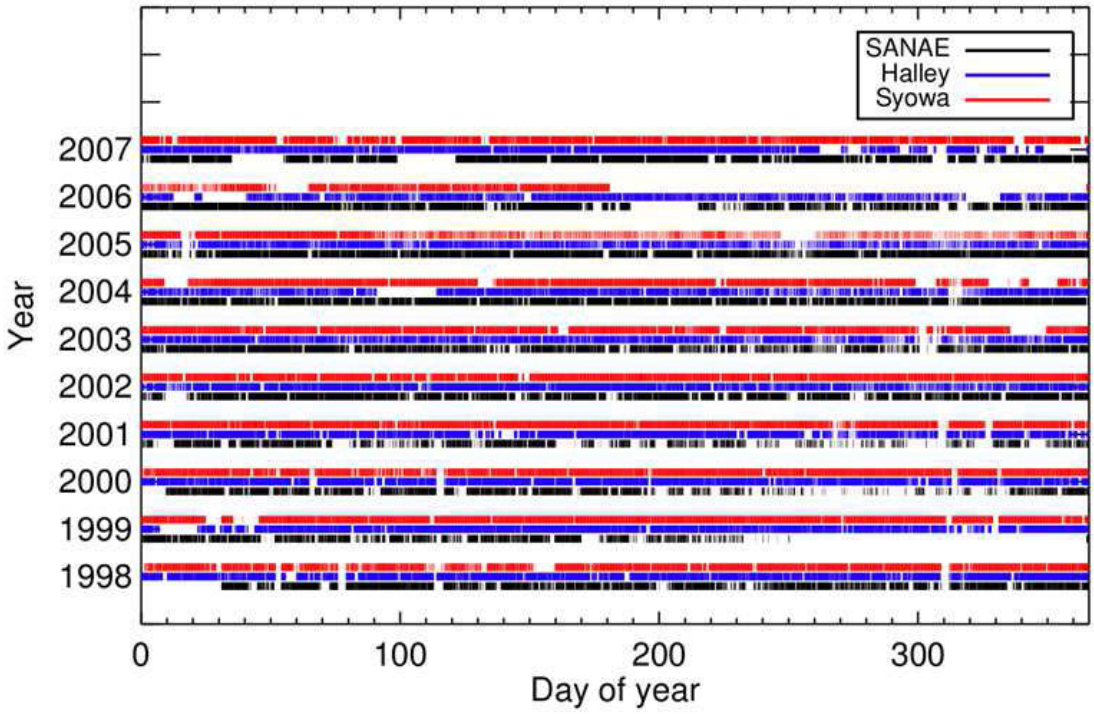

Figure 4.2: Data coverage of the SuperDARN HF radars between 1998 and 2007 at Halley, SANAE and Syowa.

The variability of tides is sometimes attributed to forcing mechanisms. To investigate this, ERA-Interim parameters like specific humidity and ozone volume mixing ratio obtained from European Center for Medium Range Weather Forecasting (ECMWF) were used. The data can be downloaded from http://data-portal.ecmwf.int/data/d/interim_daily/levtype=pl/. The daily averages of these parameters are computed from the data obtained at every 6-hour intervals.

4.3 Results and discussion

4.3.1 Seasonal variation of tides

In this section, the focus is on the climatology of tides rather than that of winds. The perspective of the climatology of winds from SANAE and Halley is presented in Mbatha (2012). Presented in Figure 4.3 and Figure 4.5 are the seasonal variations of amplitude and phase of the DT and SDT for the meridional component representing the overall monthly mean variation for the period from 1998 to 2007. The overall monthly means were computed using vector averaging provided there is more than 70 % of data of a particular month in the entire period. The zonal component of the wind velocity derived from the SuperDARN HF radars is less accurate than the winds from the meridional component due to the beam orientation and the field of view

(Jenkins and Jarvis, 1999; Hibbins and Jarvis 2008). This is because the zonal component is computed from the line of sight Doppler velocity by exploiting the swinging property of the beam into 16 directions. Thus results from the zonal component are excluded in this analysis. The variation of both tidal components resembles each other more at Halley and SANAE than at Syowa. The error bars are computed as standard error of a mean and represent the inter-annual variation.

4.3.1.1 Diurnal tide

The seasonal variation of the amplitude of the DT shown in the top panel of Figure 4.3 is characterized by maximum amplitude in summer and minimum amplitude in winter. At almost all stations, the DT reaches maximum amplitude of about 8 m s^{-1} in summer (January) and decreases to 4 m s^{-1} in winter (June). The DT amplitude at Syowa is stronger in winter with typical amplitudes of about 6 m s^{-1} and reaches maximum amplitude of ~10 m s^{-1} in January. The different behavior of DT at Syowa compared to that at Halley and SANAE may be due to mode coupling between migrating and non-migrating diurnal components (Riggin et al., 2003). Hagan et al. (1997) reported that mode coupling between the migrating and non-migrating diurnal tide excited by latent heat release, although smaller than migrating tide, the non-migrating component may produce longitudinal variability in the MLT region. The phase of the DT at Halley and SANAE is around 00:00 UT with the phase at Halley leading by approximately 1 h in spring and summer while in-phase in fall and winter. The phase of the DT at Syowa is almost constant around 23:00 UT which of course is different from the phase at Halley and SANAE by one hour.

The behavior of the DT amplitude is in line with results from other high latitude Southern hemisphere studies. Fraser et al. (1995) investigated the behavior of the DT amplitude using several years of data from Mawson (68°S, 45°E) and Scott base (78°S, 168°E) at a height of 95 km. Their results showed a similar behavior for both meridional and zonal components. Hibbins et al. (2006) using an imaging Doppler interferometer (IDI) at Halley reported summer maximum and winter minimum of the DT amplitude at 95-105 km. Hibbins and Jarvis (2008) conducted a comparative study of winds and tides measured with the IDI and the SuperDARN HF radar at Halley from 1996 to 2006. From their results, the summer maximum and winter minimum of the DT amplitude was again apparent.

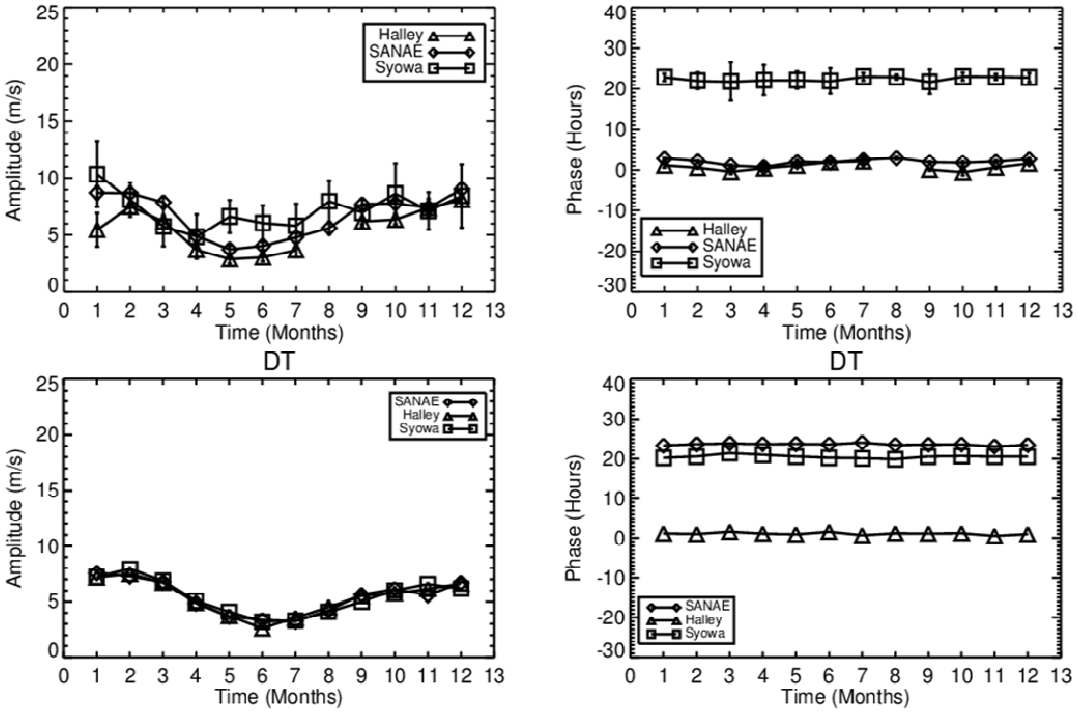

Figure 4.3: The top panel shows the meridional annual variation of monthly means of the amplitude (left) and phase (right) of the diurnal (DT) recoded by HF radars, representing data for 1998-2007. The bottom panel shows amplitude and phase of the DT deduced from the Global Scale Wave Model for 2009 (GSWM-09). The monthly means from the model are averaged over the height range 85-95 km.

The seasonal variation of the amplitude and phase of the DT derived from the global wave scale model 2009-version (GWSM-09) is presented in bottom panel of Figure 4.3. The amplitude and phase are derived from geo-coordinates (75°S, 25°W), (72°S, 5°W) and (69°S, 40°E) which are closer to the radar locations at Halley, SANAE and Syowa, respectively. Moreover, the parameters are averaged over a height range 90-95 km. This was done following the comparative study conducted by Hibbins and Jarvis (2008) at Halley using SuperDARN HF radar data and IDI data which indicated that winds and tides were best correlated at the height range 90-95 km. The variation of amplitude of the DT predicted by the model is similar to that from the observation. The DT show maximum amplitude (8 m s^{-1}) in summer and minimum amplitude in winter (4 m s^{-1}). The maximum (February) and minimum (July) predicted by the model are shifted by 1-2 months. The phase of the DT predicted by the model at Halley is constant and in phase around 0:00 UT while the phases of the DT at Syowa and SANAE are constant around 20:00 UT. The model results of the DT phases at SANAE and Halley are in agreement with the observational results. The phase of DT predicted by the model at Syowa is 3 hours ahead of the observed DT phase.

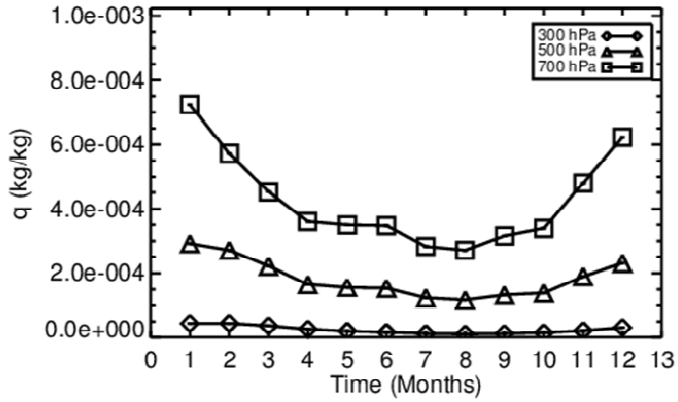

Figure 4.4: The zonal mean annual variation of monthly means of the specific humidity averaged over 69°- 75°S representing data for 1998-2007.

The DT is excited through the absorption of solar energy by water vapor in the troposphere as it contains 99% of the total water vapor in the atmosphere (Zhang et al., 2010). After excitation the DT propagates upward and its amplitude grows exponentially due to decrease in atmospheric density. By the time it reaches the MLT region, its amplitude is significantly larger. It has been reported that a forcing mechanism is one of the contributing factors that affects the variation of the DT amplitude in the MLT region. Thus, I investigated zonal mean seasonal variation of the specific humidity averaged over 69°S to 75°S as a possible source of the observed seasonal variation of DT amplitude using data from 1998 to 2007 and the results are shown in Figure 4.4. The variation of specific humidity at 300, 500 and 700 hPa is similar to the variation of the DT amplitude in the MLT region, and this indicates a possible link. The investigation by Lieberman et al. (2007) using the NASA Water Vapor Project (NVAP) IR heating revealed that the migrating component of the DT in the MLT region was excited by water vapor heating.

4.3.1.2 Semidiurnal tide

The SDT amplitudes presented in top panel of Figure 4.5 are in general stronger than that of the DT and this is in accordance with the results obtained by e.g. Manson et al. (1989); Manson and Meek (1991). This is due to the fact that the diurnal tide tends to be trapped at latitudes higher than 30°, on both hemispheres, as its period in this region is longer than the inertial period. The seasonal variation of the SDT amplitude at Halley and SANAE is described by summer maximum/winter minimum. Superimposed on this variation is an enhancement of SDT during fall equinox. The SDT at Syowa depicts the same variation, however the fall equinox enhancement is less pronounced. The phase of the SDT at Halley and SANAE are almost constant around 0:00 UT throughout the year with the phase at Halley leading. The phase

difference between Halley and SANAE is about 1 h at the beginning of the year and increases to about 2 h at the end of the year. The phase of SDT at Syowa is almost constant around 10:00 UT throughout the year.

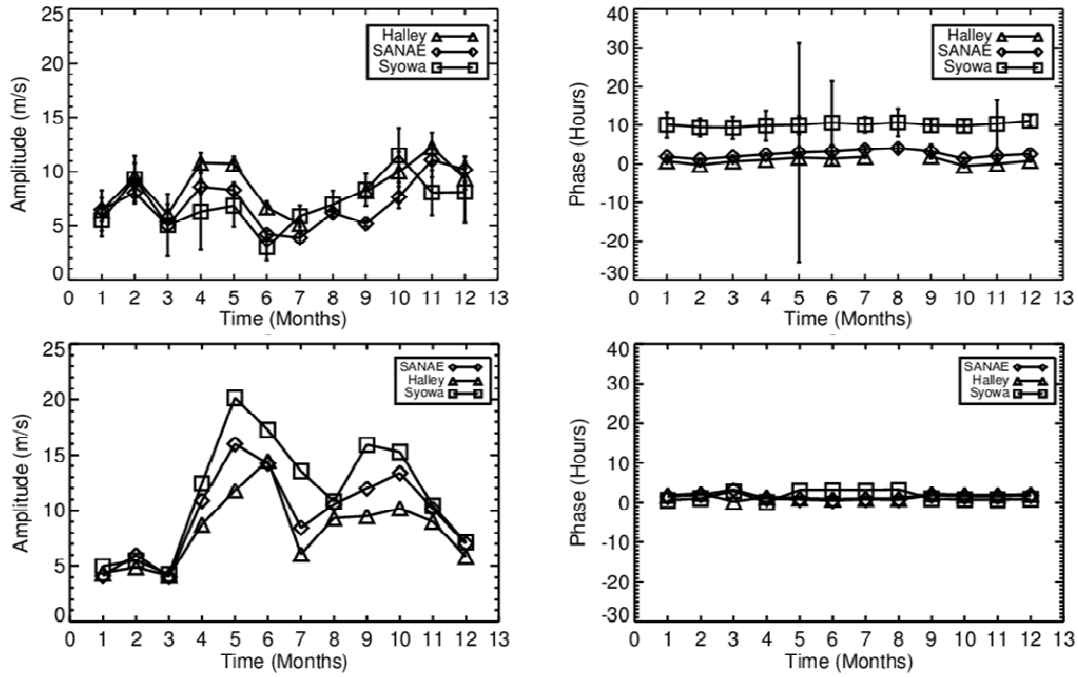

Figure 4.5: Same as Figure 4.3, but for the semidiurnal tide (SDT).

Ground-based investigation conducted by Portnyagin et al. (1993a, b, 1998) at the South Pole and Scott Base around 95 km and by Hibbins et al. (2006) at Halley using IDI data between 90 and 95 km reported maximum amplitude in summer and minimum amplitude in winter. Riggin et al. (1999) using MF radar data between 80 and 98 km at McMurdo further reported maximum amplitudes during summer and weak amplitude for the rest of the year. Riggin et al. (2003) on the other hand reported the fall equinox enhancement of the SDT amplitude around 86 km in the northern and Southern hemisphere high latitude. Previously, Burrage et al. (1995) also reported similar behavior of the SDT amplitude using the satellite measurement and attributed this to the migrating SDT. This autumn peak was accompanied by a dramatic shortening of the vertical scale of the SDT which is in line with the refraction of the wave in the background wind. The HF radars lack the necessary height resolution and thus wave refraction could not be investigated in this study.

The behavior of the SDT predicted by the GWSM-09, presented in the bottom panel of Figure 4.5 is similar to the observational result, but the predicted peak amplitudes in the fall are over estimated by the factor of 2. Contrarily, Fritts et al. (2012) found, using the meteor radar data at Antarctica (62°S), that the SDT amplitudes predicted by GSWM-09 are ~3 to 5 times less than

observed SDT amplitudes. It has been noted that the GSWM does not take into account the nonlinear interaction between migrating tides and stationary planetary waves (Grieger et al., 2004; Lieberman et al., 2004; Hagan et al., 2009; Zhang et al., 2010). Furthermore, possible nonlinear interaction between SDT and planetary wave at high latitude Southern hemisphere were reported as one of the contributing factors that cause tidal amplitude variation (Angelats-i-Coll and Forbes 2002; Baumgaertner et al., 2005; Mthembu et al., 2013). Thus, the discrepancy in the magnitude of the model and observational SDT amplitude may be due to a nonlinear interaction between a migrating SDT and stationary planetary wave. The SDT phases predicted by the model at all stations are constant around 0:00 UT. The observed phases of the SDT at SANAE and Halley are in agreement with those predicted by the model while there is two hours difference between the observed and the predicted SDT phase at Syowa.

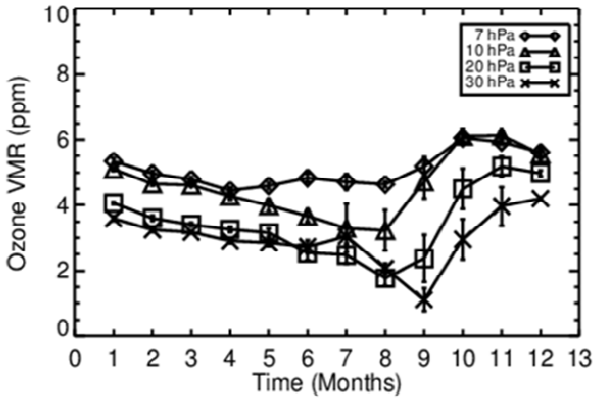

Figure 4.6: The zonal mean annual variation of monthly means of the ozone mixing ratio averaged over 69°-75°S representing data for 1998-2007.

The SDT is excited through solar energy absorption by ozone in the mesosphere and stratosphere, thus ozone could contribute towards SDT variation. For this investigation, seasonal variation of ozone mixing ratio from selected pressure levels (~25-40 km) representing data from 1998 to 2007 is presented in Figure 4.6. The ozone mixing ratio is almost constant during other seasons but peaks during summer. This peak coincides with the summer enhancement of SDT amplitude observed at Halley and SANAE in Figure 4.5. These results seem to suggest that the seasonal variation of the SDT amplitude, at least during this time, may be affected by a forcing mechanism. Therefore, while the enhancement of SDT amplitude during fall equinox may be related to refraction of the wave in the background wind, the summer enhancement could be related to the variation of ozone in the stratosphere.

Seasonal variation of SDT could also result from non-linear interaction between planetary waves and migrating semidiurnal tides. Angelats-i-Coll and Forbes (2002) presented results

over the South Pole showing that non-linear interaction between planetary wavenumber 1 and migrating semidiurnal tide results in the formation of non-migrating semidiurnal tide with wavenumber 1. Baumgaertner et al. (2005) presented the seasonal variation of the SDT recorded by medium-frequency spaced antenna (MFSA) at Scott Base (78°S, 167°E) and planetary wave deduced from geopotential height data using NCEP/NCAR reanalysis at 78°S and 78°N. Their results showed a similar variation between SDT amplitudes and planetary wave amplitudes. Based on the results by Angelats-i-Coll and Forbes (2002), Baumgaertner et al. (2005) reached a tentative conclusion that the observed seasonal variation of SDT may be the result of non-linear interaction with planetary waves. Non-linear interaction between planetary waves and semidiurnal tide is also presented by e.g. Jocobi (1999); Pancheva and Mitchell (2004); Mthembu et al. (2013) as a possible source of SDT variation.

4.3.2 Inter-annual variation

Further to investigation of the seasonal variation of tides, the inter-annual variation of tides was investigated and their results are presented in Figure 4.7. This figure shows monthly means of tidal amplitude computed as the vector average if there were more than 70 % of data available in a particular month. On inspection, some of the features clearly stand out, for example, the SDT at Halley is generally dominant over the DT while they are of comparable magnitude at Syowa. Both components reveal the annual oscillation characterized by maximum amplitudes in summer. Semi-annual oscillation is also observed from the DT and SDT at Syowa from 1999 to 2003 as well as from the SDT at Halley from 2001 to 2003. These observations were not apparent at SANAE because of large gaps in the data.

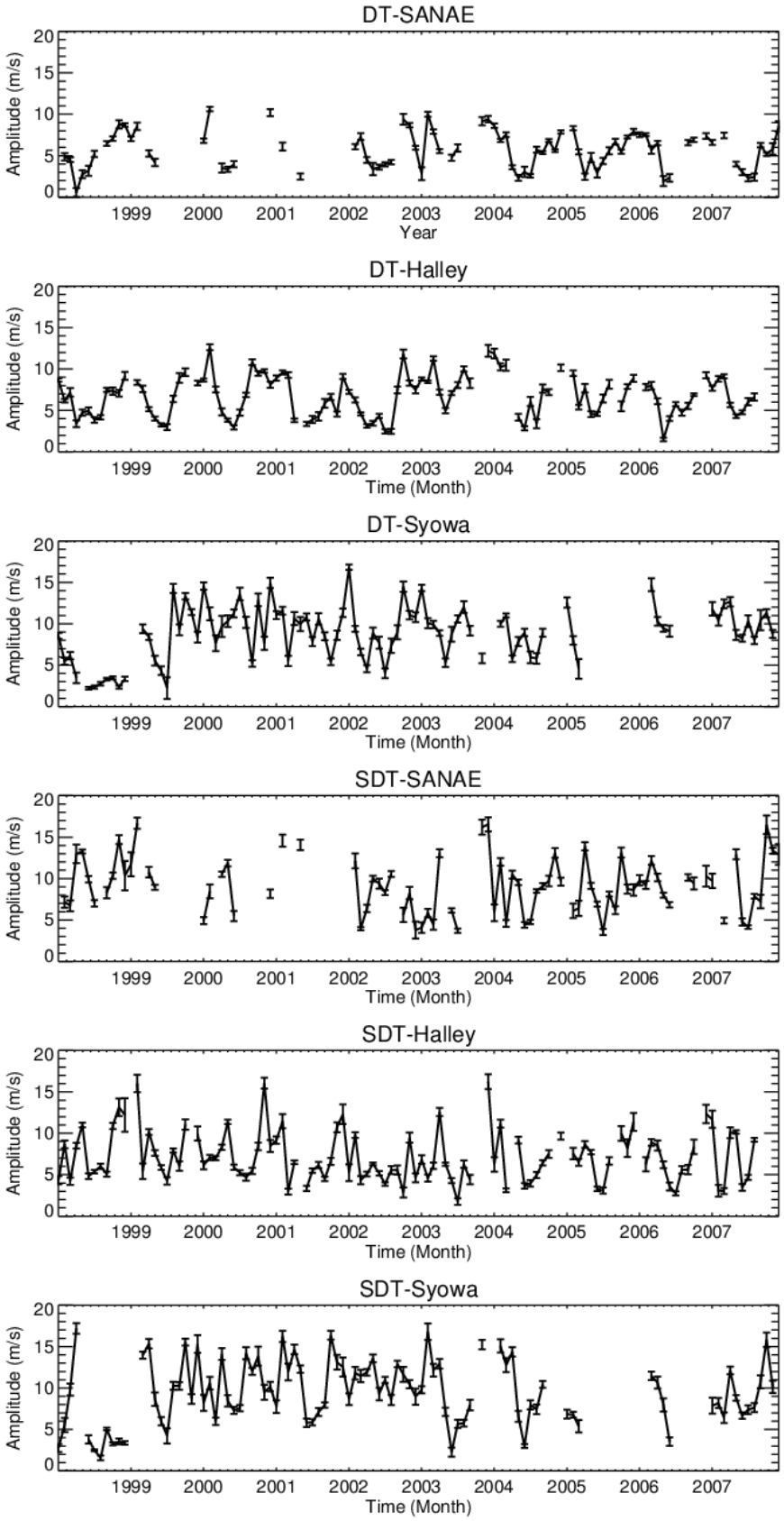

Figure 4.7: Meridional inter-annual variation of tidal amplitudes. The errors bars represent the standard error of the mean.

To investigate other hidden oscillations, a spectral analysis was performed on the monthly means of tidal amplitude from Figure 4.7 and the results are presented in Figure 4.8 (a) and (b). The time series from SANAE have numerous data gaps in the first half of the observation period, as a result the spectral analysis was performed on the data from 2002 to 2007 (results were not shown). Smaller data gaps were filled using linear interpolation. Both components at Halley and Syowa show significant peaks at 1 and 2 cycles per year (CPY) which correspond to 1- and 0.5-year oscillations. These oscillations are possibly related to the seasonal variation mentioned in Section 4.3.1. The DT and SDT at Syowa show a peak near 0.6 CPY possibly corresponding to quasi-biennial oscillation (QBO) and the DT at Halley and Syowa show a peak near 0.2-0.3 CPY (3-5 year oscillation). The SDT at Halley and Syowa show a peak near 0.1 CPY which might be connected to the 11-year solar cycle.

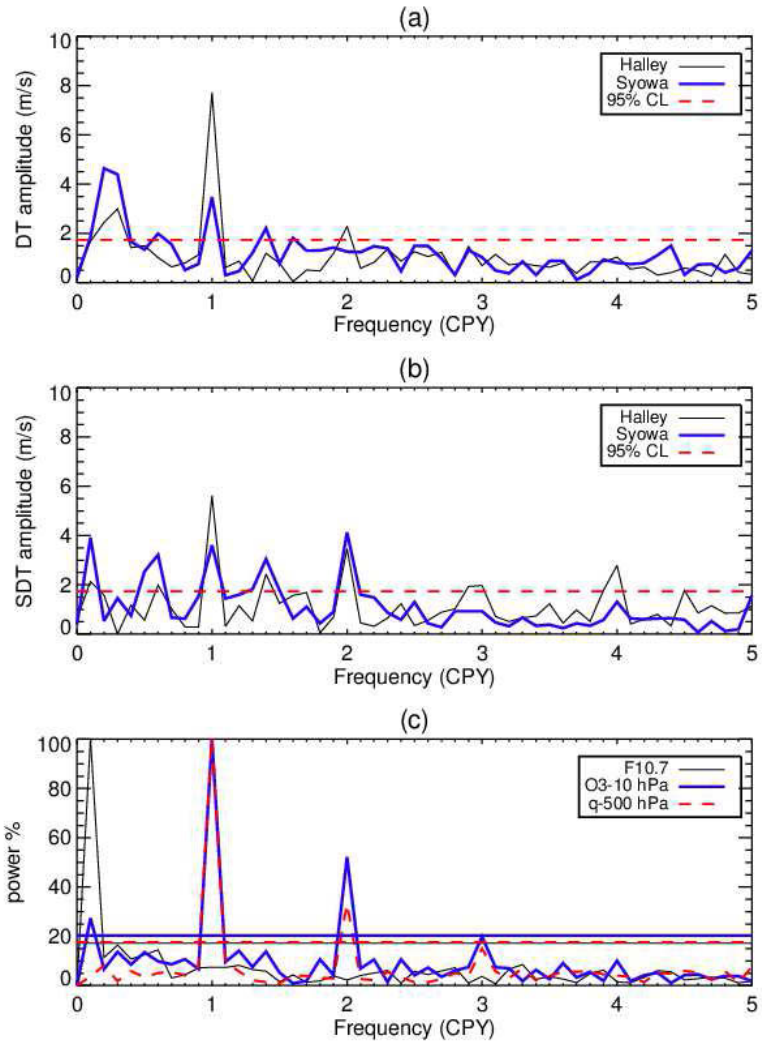

Figure 4.8: Fourier transform of (a) DT, (b) SDT amplitude from meridional wind and (c) specific humidity recorded from 500 hPa (q-500), ozone mixing ratio (O3) from 10 hPa and solar activity (F10.7). The horizontal lines represent 95% confidence levels.

Presented in Figure 4.8 (c) is the spectral analysis of solar activity, ozone mixing ratio and specific humidity. The solar activity and ozone mixing ratio at 10 hPa show the peaks near 0.1 CPY. Furthermore, the specific humidity at 500 hPa and ozone mixing ratio show peaks at 1 and 2 CPY. The existence of common peaks between tidal amplitudes as well as in solar activity, ozone and specific humidity may signify a connection. For further examination, 11-year oscillation in the SDT amplitude, solar activity and ozone mixing ratio was investigated next. The spectra analysis showed no signature of the 11-year oscillation in the DT, thus was not investigated.

4.3.2.1 The 11-year Oscillation

For the investigation of solar activity as a possible source of the 11-year oscillation of the SDT, short-term variability of the monthly means of the SDT and solar activity was removed by computing a 24-month moving average of the SDT and solar activity. The solar activity is represented by the F10.7 index expressed in solar flux units (s.f.u) which is a measure of the solar radio flux per unit frequency at a wavelength of 10.7 cm. The SDT amplitude and the F10.7 solar flux were scatter plotted (not shown) and separated according to westward and eastward phases of the QBO. The separation according to QBO phases was done following the assertion by Labitzke (2005) that it enhances the observation of the impact of solar activity. The phases of the QBO used in this analysis were those computed by Ho et al. (2009) using the National Centers for Environmental Prediction-National Center for Atmospheric Research (NCEP-NCAR) reanalysis data. The phase is represented by an index calculated using the vertical wind shear between 50 and 70 hPa of the zonally and monthly averaged zonal wind. The results of the scatter plot (not shown) indicated that there was extremely poor correlation between the SDT amplitude at SANAE and Halley during both phases of the QBO while the results at Syowa showed a strong positive correlation during both phases of the QBO. The significance of these results was tested statistically using regression analysis and the results are presented in Table 4.1. The null hypothesis in the analysis was that there is no correlation between the SDT amplitude and solar activity. The 0.05 significance level was chosen to either reject or accept the null hypothesis. Statistical significant correlations are indicated with bold values in the Table 4.1. From the table, it is apparent that the correlation is significant at Syowa during both phases of the QBO.

Table 4.1: The results for the correlation coefficient (r) correlation of determination (r^2) and the probability (p-value) from the correlation analysis between SDT amplitude and solar activity separated into westward and eastward phase of QBO.

Westward phase of QBO			
Stations	Coefficients		
	r	r^2 (%)	p-value
SANAE	-0.01	0.0	0.96
Halley	0.06	0.3	0.66
Syowa	**0.56**	**32**	**0.00**
Eastward phase of QBO			
SANAE	-0.27	7.2	0.08
Halley	-0.01	0.0	0.95
Syowa	**0.62**	**38**	**0.00**

The relationship between SDT amplitude and solar activity was further investigated by plotting the time variation of the 24-month moving average of the SDT (left axis) and solar activity (right axis) as presented in Figure 4.9. Within the observation window the solar activity increased from 1998 and reached maximum in 2002 and thereafter decreases to a minimum around 2007. Despite the data gap, the variation of SDT at Syowa seems to be in-phase with that of the solar activity while the anti-phase behavior is observed at SANAE. The variation of SDT at Halley is out of phase with that of the solar activity. Spectral analysis of the 24-month moving average of SDT and solar flux shows that the phase difference between the 11-year oscillation of solar activity and that of SDT at Halley (Syowa) is ~3 (0.7) years. The phase difference at SANAE could not be determined because of the poor quality of data.

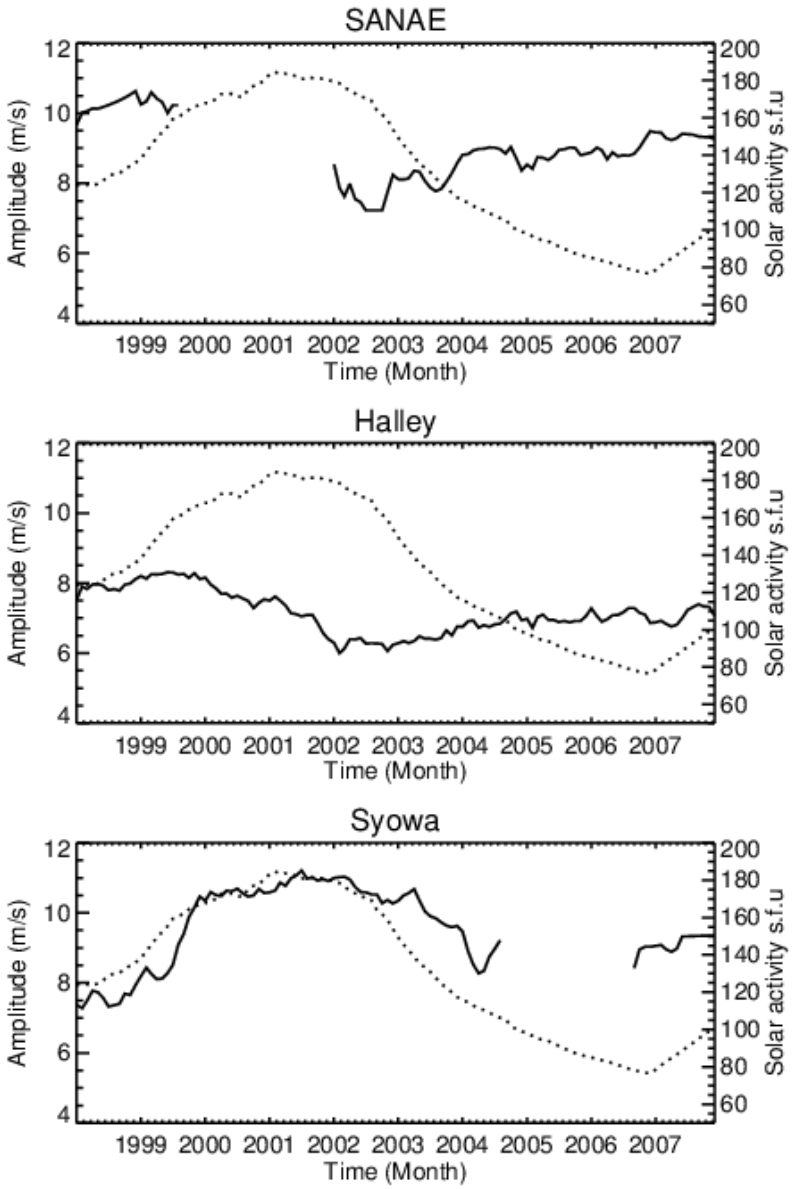

Figure 4.9: The time variation of the 24-month running average of the SDT amplitude from meridional wind (solid) and solar activity (dotted).

Numerous studies conducted in the Northern hemisphere revealed negative correlation between the SDT and solar activity (Sprenger and Schminder, 1969; Dartt et al., 1983; Greisiger et al., 1987; Bremer et al., 1997; Namboothiri et al., 1994). However, Jacobi et al., (1997) used the same dataset as that used by Greisiger et al., (1987), but for a different period, and found no relationship between tides and solar activity. From their study, they proposed that correlation depends on the period of observation and longer datasets are required for this kind of correlation analysis. The study conducted by Fraser et al. (1989) using the mid-latitude data from southern and Northern hemisphere revealed a positive correlation between the SDT and solar activity. Later Baumgaertner et al. (2005) used MF radar data from Scott Base and found a weak

negative correlation between the SDT and solar activity. The negative correlation from the present analysis at SANAE is in agreement with the earlier results from Sprenger and Schminder (1969); Dartt et al. (1983); Greisiger et al. (1987); Bremer et al. (1997); Namboothiri et al. (1994); Baumgaertner et al. (2005). However, the positive correlation at Syowa agrees with the results obtained by Fraser et al. (1989). Recent results from Iimura et al. (2011) presented the relationship between the SDT and solar flux using MF radars at Syowa and Andenes (69°N, 16°E). Their results at Syowa revealed a negative correlation in the zonal component of the SDT from 70 to 95 km. The meridional component showed a negative correlation from about 88 km and above while positive correlation was observed from about 88 km and below. The results of the present study at Syowa are in agreement with their results from 88 km and below. An investigation by Iimura et al. (2010) using the MF radar data from Hawaii (22°N, 160°W) indicated that the phase difference between the 11-year oscillation of SDT and solar activity was about 3 years, which from the present study, is in line with the results obtained at Halley.

A possible connection between the 11-year oscillation observed in the stratospheric ozone mixing ratio measured at 10 hPa and the SDT amplitude was investigated using the same method applied in the investigation of the solar activity. The results of the scatter plot of the SDT amplitude and ozone mixing ratio (not shown) and the results of the regression analysis presented in Table 4.2 show a weak significant negative correlation at SANAE and a strong negative correlation at Halley. On the contrary the results at Syowa show an insignificant negative correlation. Figure 4.10 presents the time variation of the 24-month moving average of the SDT amplitude and ozone mixing ratio at 10 hPa. The variation of ozone was minimum during the year 2000 and maximum near 2005. Despite the gap, the variation of SDT amplitude at SANAE seem to follow that of the ozone mixing ratio while opposite behavior is observed at Halley. Out of phase variation between the ozone mixing ratio and the SDT amplitude at Syowa is observed. The phase difference between the 11-year oscillation of the ozone mixing ratio and that of SDT at Halley (Syowa) is ~7(3) years. It is also worth noting that the 11-year oscillation of the solar activity is out of phase with that in the stratospheric ozone by about 4 years.

Table 4.2: The results for the correlation coefficient (r), correlation of determination (r^2) and the probability (p-value) from the correlation analysis between SDT amplitude and ozone mixing ratio.

Stations	Coefficients		
	r	r^2 (%)	p-value
SANAE	**-0.45**	**20**	**0.00**
Halley	**-0.56**	**32**	**0.00**
Syowa	-0.23	5	0.02

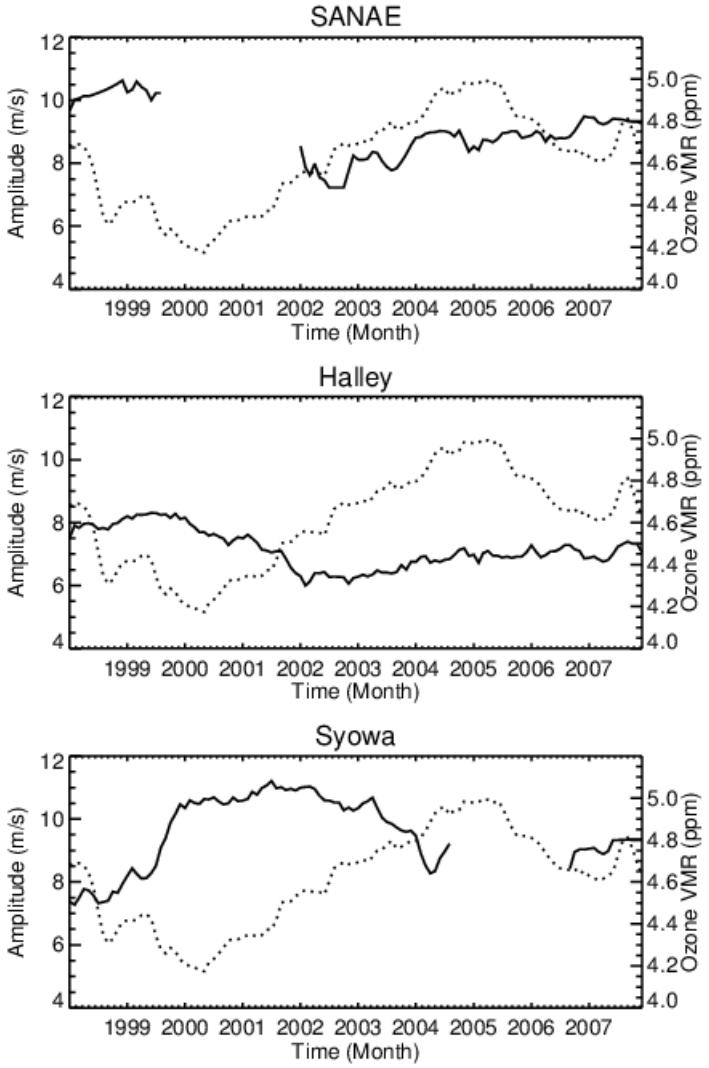

Figure 4.10: The time variation of the 24-month running average of the SDT amplitude from meridional wind (solid) and ozone mixing ratio at 10 hPa (dotted).

The mechanisms that attempt to account for the negative correlation is presented in Baumgaertner et al. (2005). The results presented by Li et al. (2008) revealed a positive correlation between solar flux as well as stratospheric temperature and ozone. Since the SDT is excited through the absorption of solar ultraviolet (UV) radiation by ozone in the stratosphere and mesosphere, SDT amplitude is expected to maximize during the period of solar maximum. After excitation, SDT propagates upward and its amplitude increases due to decrease in atmospheric density (Chapman and Lindzen, 1970). However, increase in stratospheric temperature and ozone during solar maximum leads to increase in density and pressure at higher altitudes which in turn lessens the SDT amplitude.

Although the negative correlation between the SDT amplitude and solar activity is observed at SANAE, present results show that the 11-year oscillation of the solar activity is negatively

correlated with that in the stratospheric ozone (Figure 4.9 and Figure 4.10). This is inconsistent with the assumption made in the mechanism presented by Baumgaertner et al. (2005) also inferred by Li et al. (2008). Moreover, this mechanism could not explain the in-phase relationship between solar activity and SDT observed at Syowa as well as out of phase relationship observed at Halley. Therefore the mechanism responsible for the 11-year oscillation of SDT amplitude is not yet fully established but it has been noted that the SDT variation is dependent on numerous factors including the period of observation (Jacobi et al. 1997), geographic location (Baumgaertner et al. 2005), altitude (Iimura et al. 2011), and possibly the length of data analysed, as in our study.

4.3.2.2 Other oscillation

The peak near 0.2-0.3 CPY revealed by the DT amplitude at Halley and Syowa shown in Figure 4.8 corresponds to a ~5-year oscillation. This ~5-year oscillation was also reported by Iimura et al. (2011) in the MLT SDT and DT, by Tung and Yang (1994) in the column ozone and by Mayr et al. (2007) in the NCEP reanalysis data. The analysis of 40 years' worth of zonal wind data conducted by Mayr et al. (2007) revealed a 5-year modulation of annual oscillation (AO) of winds that was large during the period when the QBO was more pronounced. The 10 years' worth of data used in our analysis poses a limitation for such analysis.

The peak near 0.6 CPY (1.6 year oscillation) shown by the DT and SDT at Syowa was investigated as to whether or not it is related to the known effect of QBO phase. For this investigation monthly means from all stations were separated according to the eastwards and westward phase of the QBO. Composite months were then computed and presented in Figure 4.11. SANAE data have numerous gaps which make comparison unclear. In general, no clear effect of the QBO was observed at Halley and Syowa, however a weak effect on the DT at Halley in April-August and on the SDT at Syowa in July-September was observed. Larger amplitude of the DT at Halley was observed during the westward phase of the QBO while large amplitude of the SDT was observed during the eastward phase of the QBO. However these results are not so significant. The signature of the QBO effect on the SDT at high latitude (65°S, 64°W) was reported by Jarvis (1996). However, Baumgaertner et al. (2005) found no significant effect of QBO on the high latitude MLT wind and tides studied using the MF radar which agrees with the results from our analysis. The explanation of the SDT could be a possible dominance of the non-migrating component which, according the Hagan at al. (1996) is less affected by the change in the QBO phase. This is based on the results by Riggin et al. (1999) which revealed the existence of migrating and non-migrating components at latitude around 60°S.

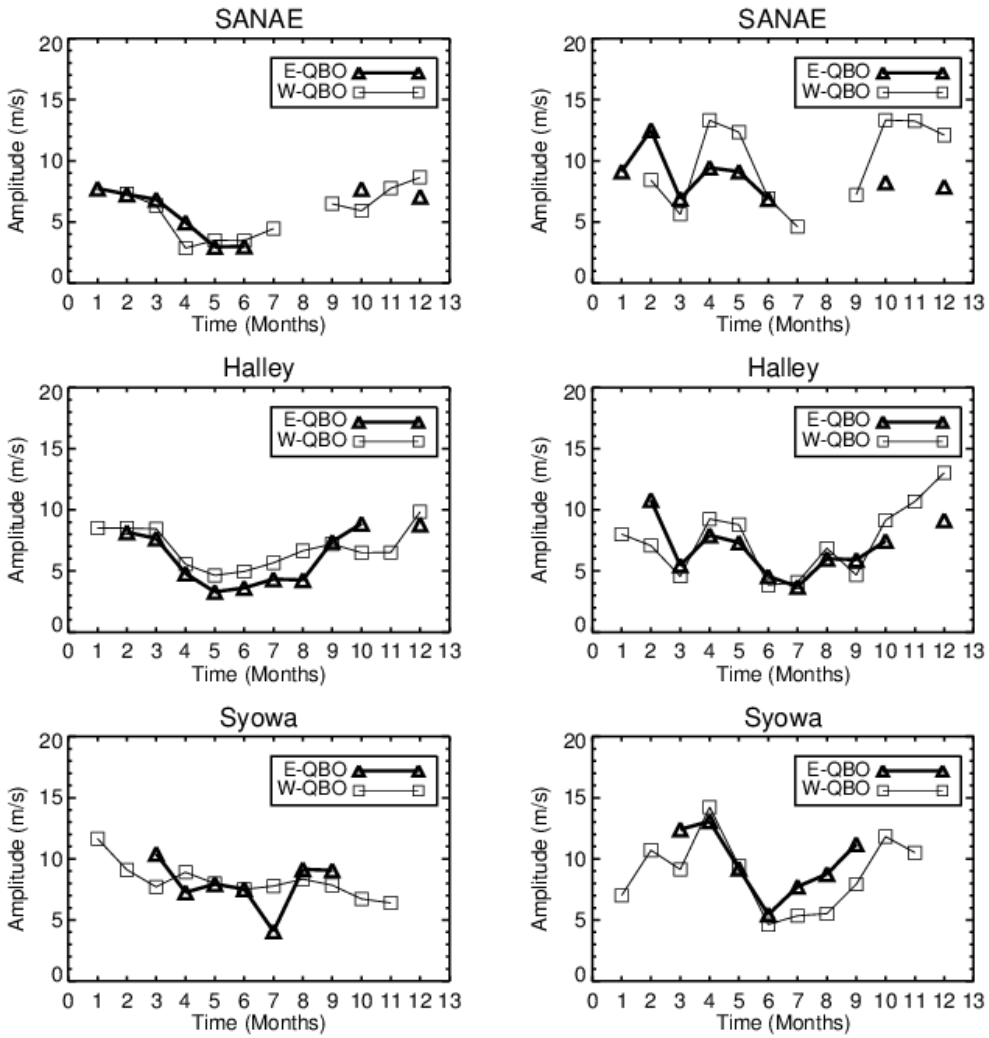

Figure 4.11: Meridional amplitude of DT (left) and SDT (right) separated according to eastward (bold) and westward phase of the QBO.

4.3.3 Trends

An investigation of long-term trends of tidal amplitudes has previously been undertaken using longer datasets of ~40 years (Bremer et al., 1997; Merzlyakov and Portnyagin, 1991; Middleton et al., 2002; Portnyagin et al., 2006). However, shorter datasets (~10 years) have also been used in this kind of analysis (Baumgaertner et al., 2005). Hence in the present study trend analysis was conducted based on the limited 10 years of data, using the 24-month running average of monthly values of tidal amplitudes. The annual vector means of DT and SDT amplitude were computed and presented in Figure 4.12. From Figure 4.12, it is apparent that the amplitudes show two different trends with the break point coinciding with the solar maximum in 2001-2002. At SANAE and Halley the tidal amplitudes were then separated into two sets which were 5 years long representing the amplitude before (1998-2002) and after (2003-2007) solar maximum. At Syowa the amplitudes before the solar maximum ranged from 1998 to 2000 and

those after the solar maximum were from 2001-2004. The trend analysis was conducted using ordinary least-squares (OLS) regression and the results of the slopes and p-values are presented in Table 4.3. The significance of the slope was statistically tested. The null hypothesis in this case is that there is a significant change in amplitude with time and the 0.05 significance level was again used to reject or accept the null hypothesis. The trend analysis in this study will be based on statistical significant slopes (with p-values less than 0.05) which are indicated as bold values in Table 4.3. The amplitude of the DT shows a positive trend before the solar maximum at Syowa and a negative trend at SANAE, Halley and Syowa after the solar maximum. The amplitude of the SDT at SANAE and Halley shows a negative trend (but insignificant at SANAE) before the solar maximum and a positive trend afterwards. Contrarily, the SDT amplitude at Syowa reveals a positive trend before the solar maximum and a negative trend afterwards. Trend analysis was also conducted using the amplitude separated according to the seasons i.e. summer, fall, autumn, winter and spring are represented by December-February, March-May, June-August and September-November respectively. The results were not presented here however they do not differ from the trend analysis of the annual means.

Table 4.3: The results for the slope (b) and the probability (p-value) from the trend analysis of the DT and SDT amplitude.

	DT			SDT	
Stations	b ($ms^{-1}yr^{-1}$)	p-value	Years	b ($ms^{-1}yr^{-1}$)	P-value
SANAE	0.01 **-0.18**	0.91 **0.04**	1998-2002 2003-2007	-0.69 **0.25**	0.17 **0.04**
Halley	-0.01 **-0.37**	0.93 **0.04**	1998-2002 2003-2007	**-0.44** **0.15**	**0.04** **0.05**
Syowa	**0.99** **-0.37**	**0.02** **0.05**	1998-2000 2001-2004	**1.50** **-0.69**	**0.03** **0.05**

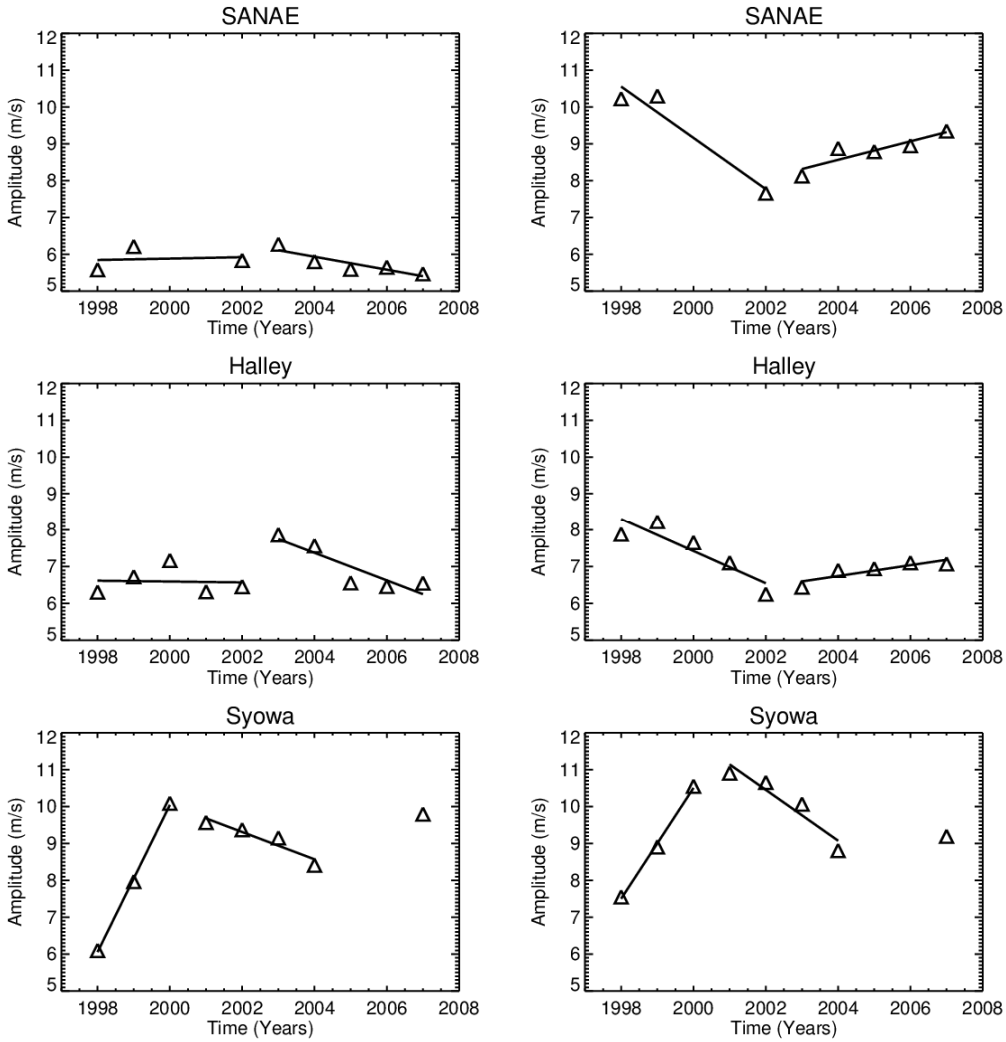

Figure 4.12: Meridional annual averages of DT (left) and SDT (right) amplitude. The solid line represents the best-fit line computed using OLS regression.

Several studies (Bremer et al., 1997; Merzlyakov and Portnyagin, 1999; Jacobi et al., 2005; Middleton et al., 2002; Baumgaertner et al., 2005) have been conducted to investigate the long-term trends of tidal amplitudes. In these studies trend analysis was conducted using the entire dataset in question. Portnyagin et al. (2006) realized that there are possible break points and changes in trends within the particular time interval. This was based on the trend analysis conducted by Bremer et al. (1997) where negative trends of annual zonal wind were obtained. However, results from the later dataset by Jacobi et al. (2002) reveal positive trend. Portnyagin et al. (2006), using the method proposed by Siedel and Lanzante (2004) and later Merzlyakov et al. (2009) using the method proposed by Wang and Zivot (2000) conducted trend analysis on the ~40 years' worth of data. Their methods were capable of determining break points and changes in trend with time. The data used in our analysis was short such that changes in trend were observed by inspection. Change in the annual trend of the SDT amplitude observed at

Halley from negative to positive were also observed by Portnyagin et al. (2006) at Obninsk. The break points of the tidal amplitude in our analysis coincide with the solar maximum which then could imply a possible link between tidal trends and solar activity. However it was mentioned in Section 4.3.1.2 that solar activity could account for the SDT observed at SANAE but not at other stations. Jacobi et al. (2005) attributed a negative trend of SDT to a decrease in ozone heating and increased carbon dioxide cooling in the middle atmosphere. Nonetheless, in our analysis, ozone cannot account for the opposite trends observed in the SDT amplitude at Halley and Syowa. Considering the warning by Percival and Rothrock (2005) that least-squares fit applied on a short dataset can incorrectly yield significant trends, any conclusion drawn from these results should be treated with caution until longer datasets are available.

4.4 Summary

The long-term variation of tidal amplitudes in the time scale of 1, ~2, ~5 and 11 years were investigated using the meridional component of the mesospheric wind velocity recorded by SuperDARN HF radars situated in the southern hemisphere. The annual variation of DT amplitude was found to be characterized by summer maximum and winter minimum. These results were found to be in agreement with those reported by other studies in the northern and Southern hemisphere as well as those deduce from GSWM-09. The phase of the DT at SANAE and Halley was found to be in agreement with that predicted by GSWM-09 while a 3 hour discrepancy was observed at Syowa. Tropospheric specific humidity was investigated as a possible source of DT amplitude variation. The results showed similar variation between two parameters which suggests specific humidity as a possible factor responsible for the DT amplitude variation.

The seasonal variation of SDT amplitude is characterized by larger amplitude in summer and smaller amplitude in winter, with an autumn enhancement superimposed on this variation. This variation agrees with that reported in the literature. According to the previous results the autumn enhancement in the SDT amplitude was accompanied by a dramatic shortening of the vertical scale of the SDT which is in line with the refraction of the wave in the background wind. The GSWM-09 also predicted the autumn enhancement. Results from the annual variation of the ozone mixing ratio at 10 hPa revealed the summer enhancement. Therefore the summer enhancement of the SDT amplitude could be the result of the ozone variability while autumn enhancement could be linked to the refraction of the wave in the background wind. The wind data used in this study do not have height resolution and therefore wave refraction could not be investigated.

Further investigation of the tidal amplitude revealed that, besides the seasonal variation, tidal amplitudes also have variations on timescales of ~2, ~5 and 11 years. Spectral analysis on the SDT amplitude at Halley and Syowa revealed the 11-year oscillation. Solar activity using the F10.7 solar flux was investigated as a possible source of this oscillation. Regression analysis on the 24-month running average of the monthly means of the SDT amplitude and solar flux revealed an insignificant correlation between the SDT amplitude and solar activity at SANAE and Halley during the eastward and westward phase of the QBO while significant positive correlation was observed at Syowa. Time variation of the SDT amplitude and solar flux further revealed negative correlation between SDT amplitudes at SANAE and solar flux as well as positive correlation at Syowa. Spectral analysis indicated that the phase difference between the 11-year oscillations of the SDT amplitude and solar flux at Halley is approximately 3 years while at Syowa it is about 0.7 years. The investigation of the 11-year oscillation in the ozone mixing ratio revealed negative correlation between SDT amplitudes at Halley and SANAE and an insignificant negative correlation at Syowa.

The negative correlation between the SDT amplitude and solar activity was reported by Baumgaertner et al. (2005). The stratospheric ozone and temperature are expected to be high during high solar activity. The SDT excited through the absorption of ultraviolet radiation by ozone during this period propagate upward and the amplitude grows exponentially due to decrease in atmospheric density. At the MLT region the SDT are expected to have large amplitudes. However, an increase in stratospheric temperature and the ozone during the solar maximum result in the increase in atmospheric density and pressure at higher altitudes and this in turn, diminishes the SDT amplitude. However, the current investigation shows a negative correlation between the ozone and solar activity which contradict the assumption made in the mechanism proposed by Baumgaertner et al. (2005). Furthermore, the mechanism presented by Baumgaertner et al. (2005) could not account for the in-phase relationship between solar activity and SDT observed at Syowa and out of phase relationship observed at Halley. This seems to suggest that the mechanism responsible for the 11-year oscillation observed in SDT amplitude and solar activity is not yet fully developed however it has been noted that the SDT variation is affected by factors including the period of observation (Jacobi et al., 1997), geographic location (Baumgaertner et al., 2005), altitude (Iimura et al., 2011), and possibly the length of data analyzed.

The ~5-year oscillation observed in SDT amplitude at Halley and Syowa was also reported in the literature, however, a longer dataset of winds are required for further investigation. The investigation of the effect of QBO phases, on the other hand, showed no significant impact on

the SDT amplitude. Previous results by Riggin et al. (1999) indicated that the high latitude SDT component is dominated by both non-migrating and migrating tides. Thus the lack of QBO effect was attributed to a possible dominance of the non-migrating tide which, according to Hagan at al. (1996), is less affected by the change in the QBO phase.

The trend analysis of the tidal amplitude was investigated using month mean values computed from the 24-month running mean of DT and SDT amplitudes. On inspection, it was noted that the trends of tidal amplitudes are changing, with the break point coinciding with the solar maximum. It was noted at SANAE and Halley that the trends of the SDT amplitude changes from negative to positive, in agreement with the results obtained by Portnyagin et al. (2006) at Obninsk. The trend observed on the SDT amplitude at SANAE and Halley is opposite to those observed at Syowa. Thus the results of the trend analysis obtained in the present study should be treated with caution following the assertion, by Percival and Rothrock (2005) that least-squares fit applied on a short dataset can incorrectly yield significant trends.

Some of the results from the study of the seasonal variation are in agreement with those reported in the literature. Moreover, evidence show that there are numerous factors that tend to influence the variation of tides at time scale longer than one year, however longer datasets are required for the investigation of tidal variation at such longer timescale.

5 Tidal variability during sudden stratospheric warming (SSW) studied using SuperDARN HF radars

5.1 Introduction

The sudden stratospheric warming (SSW) is a phenomenon that is characterized by a rapid enhancement of stratospheric temperature lasting for few days, occurs poleward from 60° latitude and at 10 hPa pressure level or below, and is followed by a deceleration and/or reversal of eastward winter winds (Schoeberl, 1978). An event where an enhancement of temperature of at least 25 K per week is registered below 10 hPa but without any reversal of zonal wind is classified as a minor warming (Schoeberl, 1978). However, if a sudden increase of temperature poleward of 60° latitude is associated with a reversal of winds from east to west and hence a splitting of the polar vortex then the event is classified as a major warming (Schoeberl, 1978; Andrews at al., 1987; Labizte and Naujokat, 2000). This phenomenon is attributed to an interaction of upward propagating planetary waves with zonal mean circulation (Matsuno, 1971). Planetary waves are excited in the tropospheric region, by among other sources, topography and instabilities associated with temperature variations, and they propagate up to the stratosphere and the MLT region, particularly in winter. Wave-mean flow interaction of planetary waves and zonal mean circulation in the middle atmosphere induces westward forcing during winter which then decelerates eastward winds or to a larger extent, reverses. Deceleration/reversal of eastward winds at high latitudes alters the filtering process of upward propagating gravity waves in the stratosphere by filtering out westward gravity waves while allowing more eastward gravity waves to propagate from their source region in the troposphere up to the MLT region (Sathishkumar and Sridharan, 2009). At the MLT region, gravity waves break due to various processes including convective instabilities thereby introducing an eastward forcing which restores the eastward winds. This process also affects the middle atmosphere meridional circulation by inducing a downward circulation in the stratosphere causing adiabatic heating and an upward circulation in the mesosphere resulting in adiabatic cooling (Liu and Roble, 2002; Coy et al., 2005). The observational evidence of stratospheric and mesospheric processes that accompany the SSW event was presented by various researchers (for e.g. Dowdy et al., 2004; Cho et al., 2004; Hoffmann, 2007; Mbatha et al. 2010).

Sridharan et al. (2009) investigated the behavior of tidal amplitude using the equatorial (8.7°N, 77.8°E) MF radar winds and their results show that the semidiurnal tide (SDT) amplitude was

enhanced during the 1998-1999 and 2005-2006 SSW events while the diurnal tide (DT) amplitude was smaller. The enhancement of the SDT amplitude coincided with the onset of the stratospheric warming. According to Randel (1993), during SSW, ozone concentration increases at lower latitudes while it decreases at higher latitudes. Thus, during these events the SDT amplitude variation was related to the variation of ozone. Lim et al. (2012) also investigated the behavior of the tidal amplitude during the SSW using equatorial (7.4°S, 35.6°W) winds measured from the meteor radar. According to their results the tidal amplitudes were small during the SSW and enhanced after the event. This behavior ruled out ozone and water vapor as possible causes of the tidal amplitude variability. Instead, they proposed latent heat released by convective activity in the troposphere and stratospheric ozone variability associated with extreme SSW events as a possible cause of the tidal amplitude variation. The investigation by Sridharan et al. (2012) using the equatorial (8.7°N, 77.8°E) MF radar wind revealed that the variability of tides is related to tidal forcing. The SDT amplitude in the MLT region during the SSW was enhanced when the ozone values were large. On the contrary, the DT amplitude during the same event was less than that of the SDT. The decrease of the DT amplitude was found to be related to the variation of water vapor in the troposphere.

The nonlinear interaction between tides and stationary planetary waves has been found to be a contributing mechanism responsible for tidal amplitude variations. The SDT is dominant at high latitudes and observational evidence of nonlinear interaction between the SDT and planetary waves has been presented before (Pancheva and Mitchell, 2004; Hibbins et al., 2007, Mthembu et al., 2013). The variability of tidal amplitudes during the SSW is also attributed to nonlinear interactions between SDT and planetary waves (Sridharan et al., 2009; Chang et al., 2009). Modeling studies conducted by Chang et al. (2009) before the warming revealed that the westward non-migrating semidiurnal (s=1) was anti-correlated to that of the westward planetary wavenumber s = 1 (PW_W1). During these wave events the migrating semidiurnal tide amplitude was found to decrease. This behavior is consistent with generation of the non-migrating semidiurnal tide from nonlinear interaction between migrating semidiurnal tide and PW_W1.

The first study on an investigation of the Southern hemisphere 2002 SSW conducted using the SANAE HF radar is presented in Mbatha et al. (2010); Mbatha (2012). This study concentrated on the dynamical processes of the MLT region which include the behaviour of the mean winds recorded by SANAE HF radar, the behaviour of planetary waves and the response of the thermal structure in the stratosphere and the MLT region caused by the SSW. Some of the results revealed the enhancement of the mean zonal and meridional winds throughout the 2002

winter period caused by the amplification of large planetary waves. The results further showed the reversal of the MLT wind about one week before the reversal of the stratospheric winds, in accordance with the results presented by Dowdy et al. (2004); Hoffmann et al. (2007). Among the observed planetary waves is the 14- to 16-day wave in the meridional winds with zonal wavenumber 1 which was also reported by Dowdy et al. (2004). Reported also in the study is an unusual enhancement in temperature which started in the mid-September as well as the cooling and temperature signature of inversion layers in the MLT region which took place just before the SSW. This behavior was attributed to energy deposition caused by breaking gravity waves in the mesosphere. The present study takes a different direction and concentrates on the behavior of the SDT prior to and post the 2002 SSW. In addition to the Fourier and wavelet transform utilized in Mbatha (2012), analytic signal and bispectrum are used in the current analysis.

The aim of the present study is to investigate the variability of the SDT amplitude from day 160-310 (the range also considered by Chang et al. (2009) in their modeling study), which includes the 2002 SSW event in the southern hemisphere. In this investigation the forcing mechanism and nonlinear interaction between the SDT and the planetary waves were investigated as possible sources of the SDT variation. Section 5.2 describes the data sets and method of analysis. Section 5.3 describes the observed SSW event and the possible causes of the SDT variability are investigated and Section 5.4 provides the summary of the results.

5.2 Data set and method of analysis

This study has been conducted using the SuperDARN HF radar winds collected from Halley, SANAE and Syowa. The SSW event was investigated using the zonal-mean temperature over 80°S at 10 hPa (~32 km) and zonal-mean zonal winds over 60°S at 10 hPa pressure levels from the National Center for Environmental Prediction and National Center for Atmospheric Research (NCEP/NCAR) reanalysis project available on-line (http:/www.cdc.noaa.gov/). It is a joint project between the NCEP and the NCAR which provides daily meteorological values on 2.5° latitude by 2.5° longitude obtained from different meteorological instruments.

The variability of SDT was first compared to the behavior of ozone. For this analysis, the ERA-Interim parameters such as ozone volume mixing ratio obtained from European Center for Medium Range Weather Forecasting (ECMWF) was used. Daily averages of this parameter were computed from the data obtained at 6-hour intervals.

5.3 Results and discussion

5.3.1 SSW event and variation of zonal winds at the MLT region

A detailed description of the 2002 SSW event is given by, among earlier researchers Dowdy et al. (2004); Mbatha et al. (2010), however a brief description is mentioned here. Figure 5.1 shows the variation of the zonal-mean temperature over 80°S at 10 hPa (~32 km) and the zonal-mean zonal winds over 60°S at 10 hPa pressure levels. The figure shows a sudden increase in temperature of about 35 K over a period of ~7 day from day 261. This phenomenon is accompanied by a reversal of stratospheric zonal mean wind on day 268 (25 September), thus this event is classified as a major SSW (Schoeberl, 1978). Three episodes of minor warmings are observed near days 235, 245 and 257. These events are classified as minor warming since they are not accompanied by a reversal of stratospheric winds (Schoeberl, 1978; Andrews et al., 1987; Sivakumar et al., 2006; Mbatha et al., 2010).

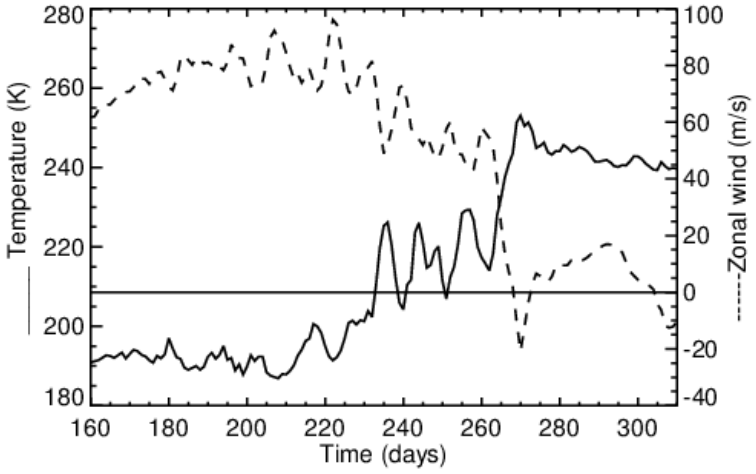

Figure 5.1: The stratospheric zonal mean wind over 60° S (dotted line) and temperature over 80° S (solid line) from NCEP reanalysis data for 2002.

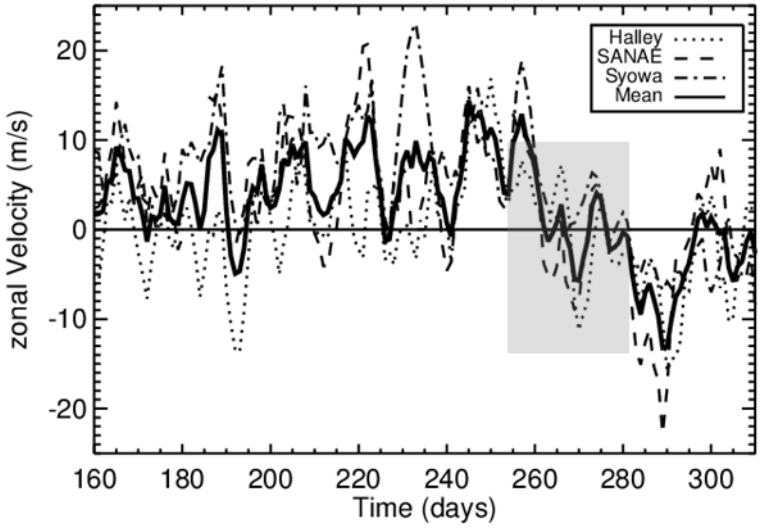

Figure 5.2: Daily averages of zonal winds recorded from Halley, SANAE and Syowa in 2002. Positive (negative) wind velocity represents eastward (westward) winds. The grey shade indicates the time just prior to and post sudden stratospheric warming (SSW).

Figure 5.2 presents daily averages of the MLT zonal winds for 2002 computed using a 4-day running window which was progressively shifted forward by one day. The data were derived from three Southern hemisphere SuperDARN HF radars located at Halley (75°S, 26°W), SANAE (72°S, 3°W) and Syowa (69°S, 36°E). Superimposed on the figure is an average behavior of wind from all stations (solid line in the figure). On average the eastward winds dominates from day 160 to 260 at all stations after which the zonal winds at SANAE show a reversal from east to west around day 260 which is 8 days before the reversal of stratospheric winds at 10 hPa. The westward winds persisted until day 273 and then returned to eastward. The zonal winds at Syowa show a very brief reversal from east to west which lasted for approximately one day and this took place about 5 days after the reversal of winds at SANAE however, a sudden decrease in wind speed at Syowa from ~20 m/s started on day 255. Zonal winds at Halley show an almost similar behavior with those at Syowa but the reversal took place one day after that at SANAE and the decrease in zonal winds from ~ 8 m/s started on day 255. The average behavior of the MLT zonal winds from all three stations (thick line) show that the east to west reversal took place around day 260. Dowdy et al. (2004) also consider the average behavior of zonal winds from Rothera (68°S, 68°W), Davis (68°S, 78°E) and Syowa (69°S, 40°E) and their results revealed the east to west reversal of winds were near day 261. The zonal winds returned to be eastward around day 270 after a brief eastward winds observed around day 264. These results are consistent with those documented in the literature (Dowdy et al., 2004; Hoffmann et al., 2007; Mbatha et al., 2010).

5.3.2 The SDT variability

SDT variability is investigated prior to and post the 2002 SSW event using data from day 160 to 310, the time interval considered by Chang et al.(2009). The variability of tides was first investigated by computing a dynamic Fourier transform of the winds from all three stations and the spectra are shown in Figure 5.3. The dynamic spectra were produced by computing the Fourier transform of a 10-day data window which was progressively shifted forward by one day. The computed spectrum was attributed to a "central" day of the particular data window taken to be day 5. The spectra show clear tidal activity with frequencies near 2 and 1 cycles per day (CPD) corresponding to SDT and DT, respectively, as well as intermittent burst of planetary wave activity at frequencies less or equal to 0.5 CPD. The zonal component shows that the strongest tidal activity was observed at Syowa while the meridional component shows that stronger tidal activity was observed at SANAE. Evident from the spectra is a clear weakened SDT activity during the presence of planetary waves. This behavior is noticeably observed in the zonal component at Syowa near day 200 as well as in the meridional component at SANAE and Halley near day 200 and 270. There are numerous mechanisms that could be responsible for this behavior such as those listed in Pancheva (2000). However, forcing mechanism and nonlinear interaction between tides and planetary waves are investigated in this study.

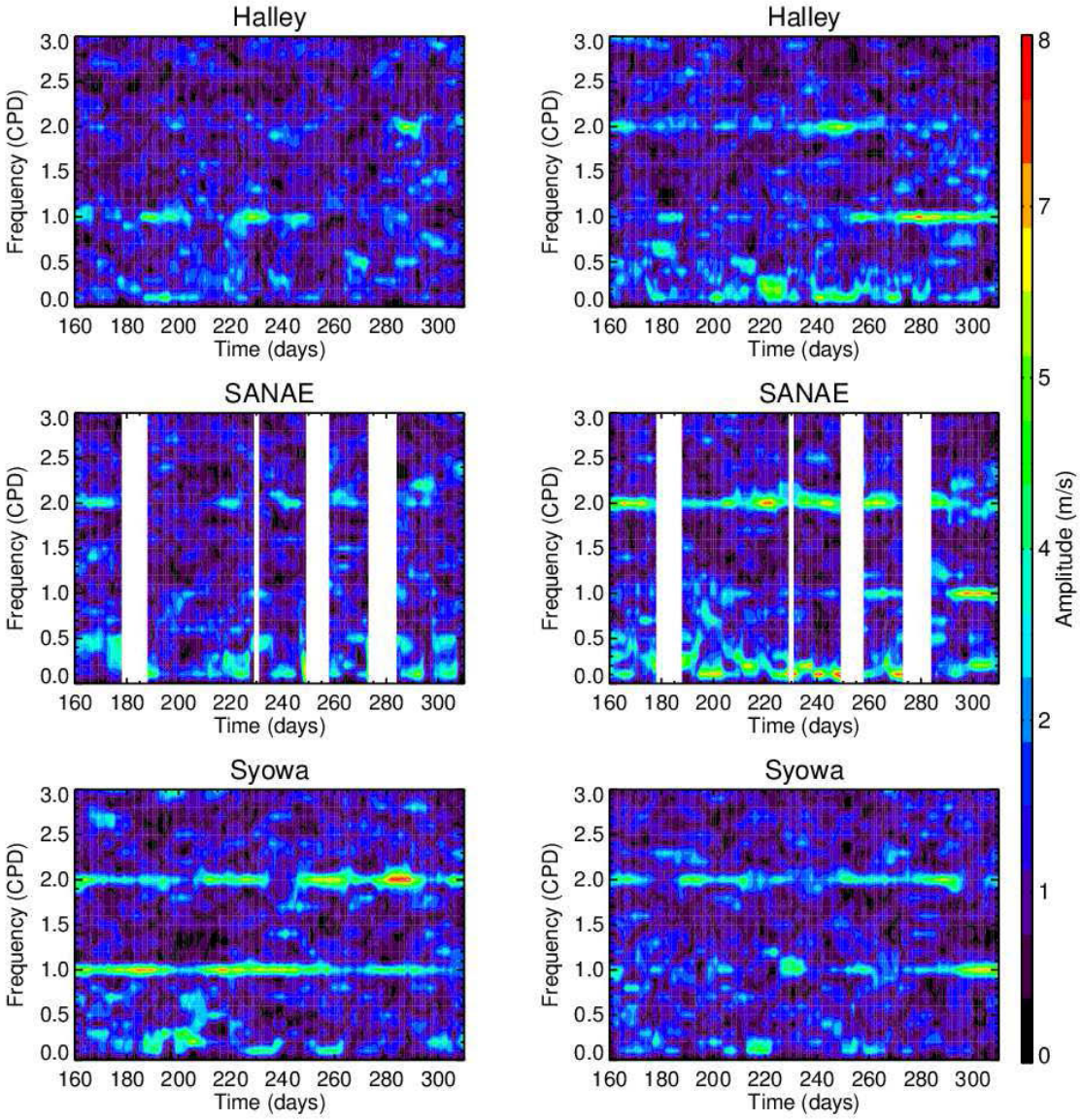

Figure 5.3: The dynamic spectra of zonal (left panel) and meridional (right panel) MLT winds from SuperDARN HF radars for 2002.

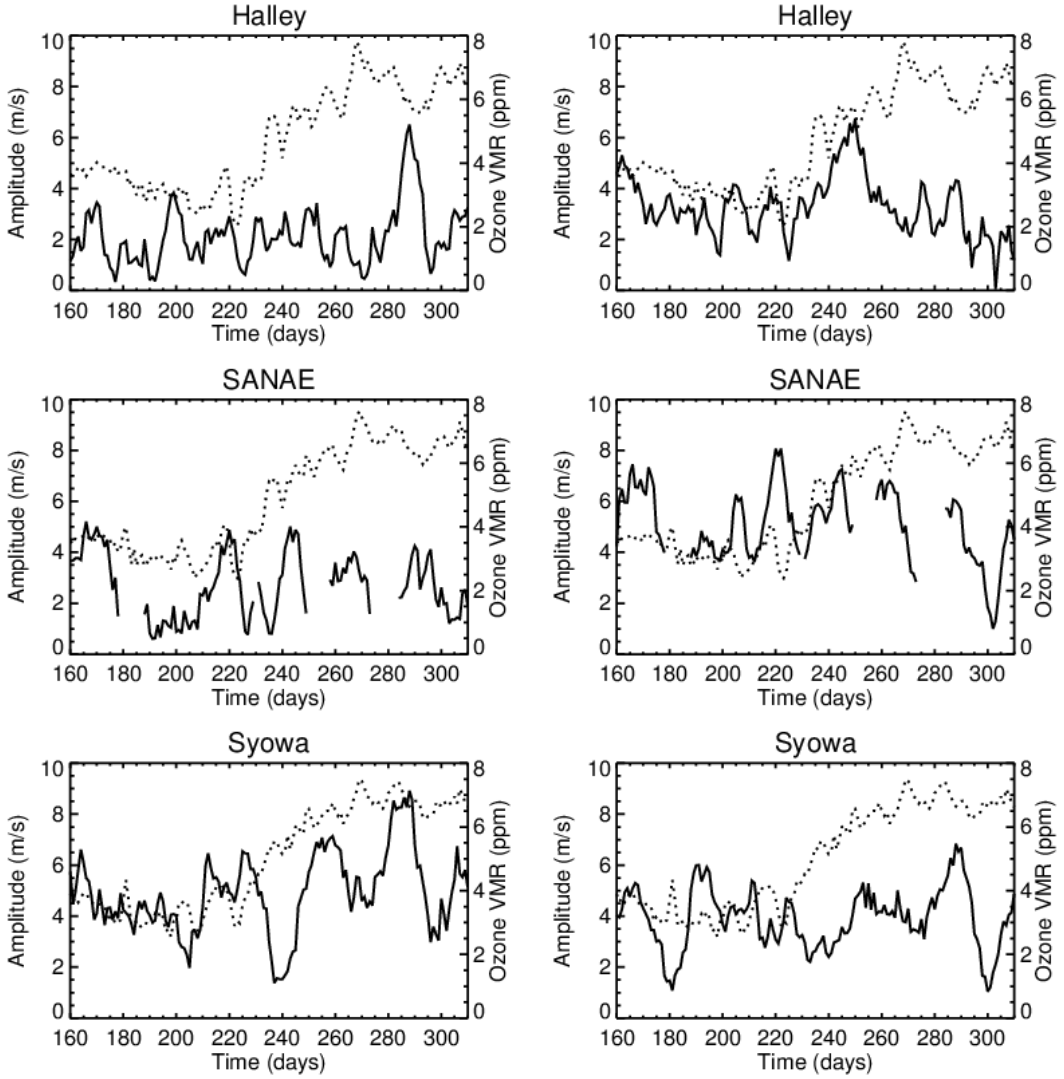

Figure 5.4: The SDT amplitude (solid line) from the zonal (left) and meridional (right) component. The dotted line represents the ozone mixing ratio at ~30 km (10 hPa) and near 75° S (top), 72° S (middle) and 69° S (bottom).

5.3.3 Forcing mechanism as possible source of the SDT variability

To start with, the forcing mechanism was investigated as a possible cause of the observed SDT variation. The SDT is generated the through absorption of ultraviolet radiations by ozone in the stratosphere and mesosphere. Owing to the availability of stratospheric data, stratospheric ozone behaviour was investigated as a possible source of the SDT variability (Müller-Wodarg et al., 2001; Mayr et al., 2005). Amplitudes of the SDT were extracted from Figure 5.3 in the zonal and meridional component and presented in Figure 5.4. Also shown in Figure 5.4 is the variation of ozone mixing ratio at 10 hPa (~32 km) near latitudes 75°, 72° and 69° S that are close to Halley, SANAE and Syowa, respectively. The ozone mixing ratio shows almost similar behavior for all three stations. This behavior is characterized by a slight decrease in ozone from

about 5 ppm near day 160, reaching a minimum of about 4 ppm around day 200 and thereafter rising to a maximum of about 8 ppm near day 260. Beyond this ozone decreases to about 6 ppm near day 290. The SDT amplitudes in the zonal component at Syowa and SANAE show a decrease in amplitude from day 160 reaching a minimum near day 180-200 thereafter increasing reaching maximum near day 220-230. On the other hand, the SDT in the meridional component at Halley decrease from day 160 reaching a minimum near day 200-220, thereafter increasing reaching maximum near day 250. Except for the enhancement in the SDT amplitude in the meridional component at SANAE near day 210 and 220, the SDT at both stations have similar behaviour from day 160 to 250. Thus at least for this time interval (day 160-250) and in these stations (Halley and SANAE in the meridional component as well as at SANAE and Syowa in the zonal component), the variation of SDT amplitude could possibly be attributed to the variation in ozone mixing ratio. The SDT amplitude in the meridional component at Syowa seems to behave differently from that at SANAE and Halley. This behavior may be caused by mode coupling between migrating and non-migrating components (Riggin et al., 2003). The longitudinal variability of tides in the MLT region caused mode coupling between the migrating and non-migrating diurnal tide which are excited by latent heat release was reported by Hagan et al. (1997).

For the time interval day 250 to 310 (which includes the SSW event) the variation of ozone is not correlated with that of the SDT amplitude from all stations and for both components. The SDT amplitude from all stations in the zonal component as well as in the meridional component at Syowa does not exhibit a clear trend in this time interval. However, the SDT amplitude in the meridional component at Halley and SANAE seem to decrease from around day 250 while the ozone mixing ratio continues in an upward trend. Sridharan et al., (2012) have investigated the behavior of SDT in the Northern hemisphere during the 2006 and 2009 SSW events. Lima et al. (2012), on the other hand, investigated the behavior of the SDT in the Southern hemisphere low latitude during the 2005-2006 SSW event and the results from both studies showed the enhancement of the SDT amplitude during the SSW events. As the SDT is produced by the absorption of ultraviolet radiation by ozone, Sridharan et al. (2012) attributed the enhancement of the SDT amplitude to an increase in ozone mixing ratio observed during the SSW event. However the present results are contradictory, indicating that at least for the time interval of day 250-310 a different mechanism, other than ozone variation, is responsible for the SDT amplitude variation.

The relationship between the SDT and the SSW is not yet confidently theoretically established. However, Sridharan et al. (2009) suggested that low latitude tidal variability during major SSW

could be attributed to a nonlinear interaction between the SDT and planetary waves. There are observational (Pancheva and Mitchell, 2004; Hibbins et al., 2007) and theoretical (Angelats-i-Coll and Forbes, 2002; Chang et al., 2009) evidence which link the variation of the SDT amplitude to nonlinear interactions between SDT and planetary waves. Thus, this mechanism is investigated as a possible cause of the SDT variability before, during and after the SSW event.

5.3.4 Nonlinear interaction as possible source of the SDT variability

The study will begin with the investigation of planetary waves in the MLT winds. Planetary waves in the MLT region are transient and their energy varies with time, thus wavelet spectrum (using the Morlet wavelet) was used to determine the spectral content due to its ability to locate the time of occurrence as well as temporal variation of their amplitudes. The Morlet wavelet transform is widely accepted in the scientific community and has been used by numerous researchers for investigating the spectral content of time series (Malinga and Ruohoniemi, 2007; Pancheva and Mitchell, 2004). The normalized wavelet spectra of the 2002 MLT winds from Halley, SANAE and Syowa are presented in Figure 5.5 from day 160 to 310 with the zonal winds on the left panel and meridional winds on the right panel. The 95% percent confidence level is indicated with a white contour. The figure shows the quasi-16 day waves (period range 12-19 days) in the meridional component from Halley (day 180-230 and near 270), SANAE (day 200-280) and Syowa (220-280). The period of the quasi-16-day wave at SANAE changes with time from 20 days near day 200 to 10 days near day 260. The meridional component at Halley and SANAE shows a quasi-23 day wave (period range 20-26 days) activity around day 280 to 310. The activity of the quasi-10-day wave (period range 6-11 days) is shown in the meridional component at SANAE around day 200 and Syowa around day 220. Another quasi-10-day wave activity is observed around day 240-260 at all stations. The zonal component shows the 16-day wave activity at SANAE from day 200 to 220 and a quasi-14-day wave (period range 9-16 days) at Syowa from day 220 to 260. The zonal component also shows a quasi-23 day wave activity around day 280 to 310 at all stations, but it is strongest at SANAE. A 10-day wave activity is observed in the zonal component at Halley and SANAE around day 200. The above mentioned waves were also observed by Mbatha et al. (2010). From now on, the investigation concentrate on the 16- and the 10-day waves in the meridional component as these wave activities are simultaneously observed at all station. Furthermore, this eases computation of zonal wavenumbers of the planetary waves.

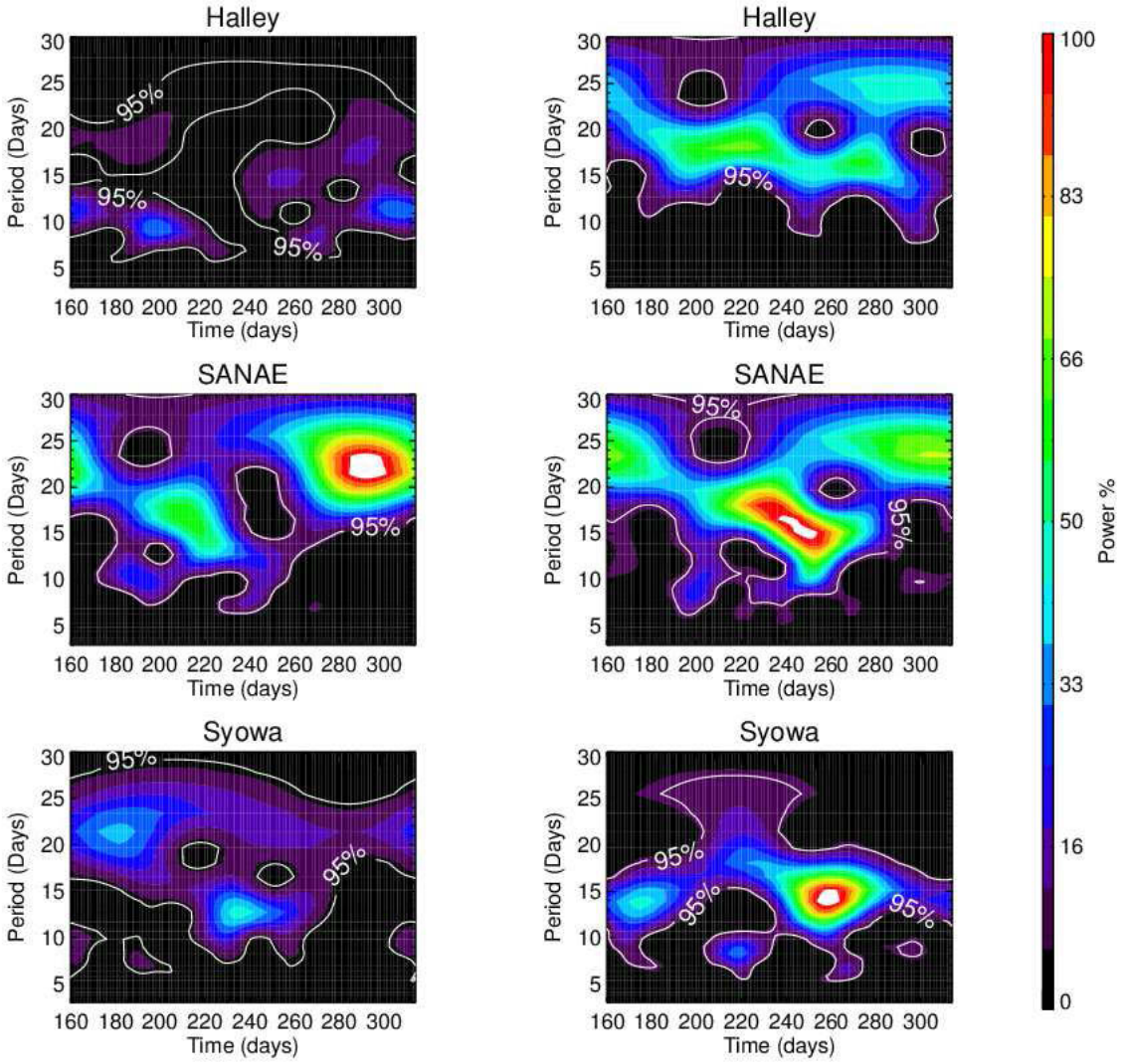

Figure 5.5: The normalized wavelet power spectra of the 2002 zonal (left panel) and meridional (right panel) MLT winds from Halley, SANAE and Syowa.

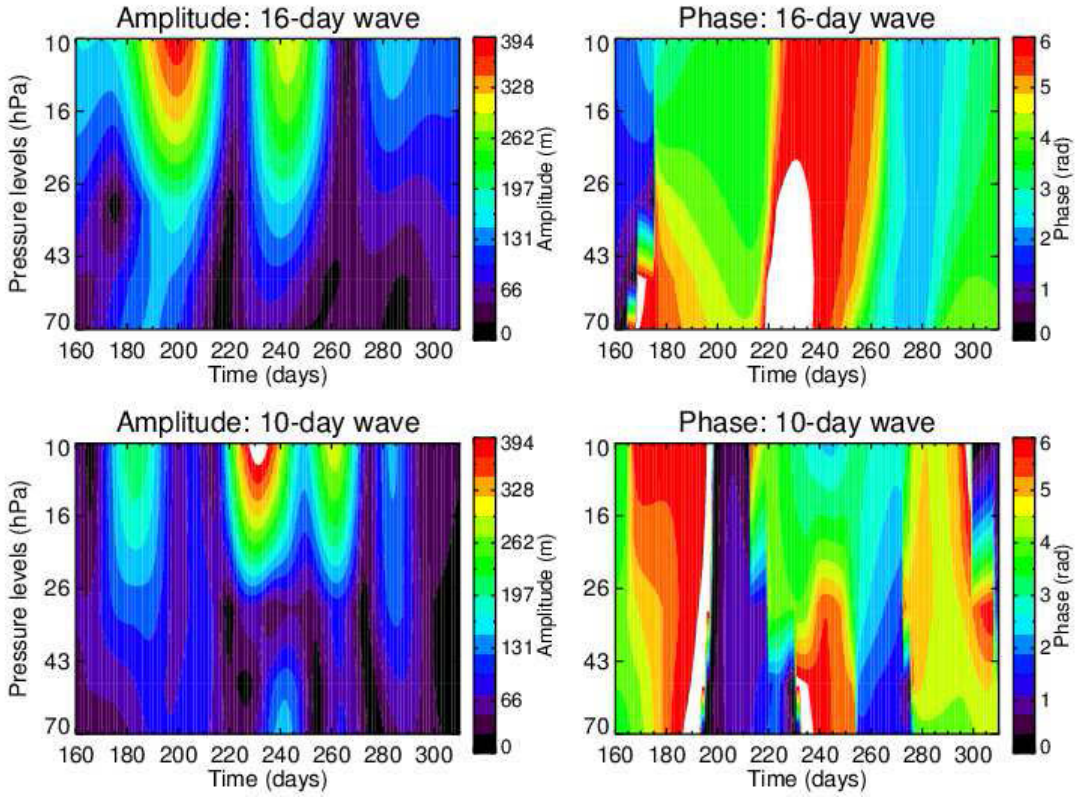

Figure 5.6: The amplitude (left) and the phase (right) of the 16-day wave (top) and the 10-day wave (bottom) computed from the geopotential height.

The planetary waves are excited in the tropospheric region and propagate up to the stratosphere and the MLT region, particularly in winter. Thus, the 16- and the 10-day waves observed in the MLT region were also investigated in the stratosphere using the geopotential height from the NCEP reanalysis data over 60° S. The 16- and the 10-day waves were investigated by computing their instantaneous amplitude and phase using an analytical signal which is given by $AS(t) = f(t) + jHi(t)$ where $f(t)$ is a real function and $H(t)$ is the Hilbert transform (Brook and Wyne, 1998). The analytical signal provides a temporal evolution of amplitude and phase of a particular spectral component. Since this method works well with monochromatic signals, the data were band pass filtered around the periods of 10 and 16 days using an FFT filter with a bandwidth of 6 and 8 days (i.e. 7-13 days for the 10-day wave and 12-20 days for the 16-day wave) respectively. A similar kind of bandwidth was also considered by Luo et al. (2002); Day and Mitchell (2010b) in their investigation of the 16-day planetary wave. The instantaneous amplitude and phase were computed as the amplitude and phase of the analytical signal and presented in Figure 5.6. The top panel shows the 16-day wave activity near day 180-200, 240 and 270-310. The bottom panel on the other hand shows the 10-day wave activity near day 180, 240, 260 and 290. The phase of the 16-day wave falls with height near day 180-200 and 240,

indicating an upward propagation. The phase gradient of the 10-day also falls with height near day 240 which indicate that it is propagating upward. Therefore the planetary waves observed in the stratosphere have possibly propagated upward and manifested in the MLT region.

The occurrence of nonlinear interaction between SDT and planetary wave is investigated by proving the validity of phase, frequency and wavenumber relationship (Pancheva and Mitchell, 2004; Mthembu et al., 2013). The phase and frequency relationship has been established using bispectrum and is described in Section 5.3.4.1 while the wavenumber relationship is proved by computing the zonal wavenumbers of the 16-, 10-day planetary waves, SDT and secondary waves in Section 5.3.4.2 and 5.3.4.3. Additional evidence of the non-linear interaction is presented in Section 5.3.4.4.

5.3.4.1 SDT amplitude modulation and Bispectrum

The interaction between upward propagating transient planetary wave and zonal mean circulation results in the formation of SSW event (Matsuno, 1971). Moreover these planetary waves may modulate tidal amplitude at periods corresponding to that of planetary waves. The SDT amplitude modulation in the 2002 winds was investigated by computing wavelet spectra of their daily values from Figure 5.4, and the results are presented in Figure 5.7. This figure shows modulation of the SDT amplitude at period around 16 days at Halley, SANAE and Syowa near day 180-220. The modulation of the SDT amplitude at 10 day periodicity is observed near day 240-260 at all stations. The 10-day modulation is also observed near day 300 at Halley and Syowa. The quasi-20-day modulation is seen at Halley near day 200, SANAE near day 270 and Syowa near day 290. The modulation of the SDT amplitude at 16-day periodicity near day 180-220 and that at 10-day periodicity near day 240-260 coincides with the 16- and 10-day planetary wave activity as observed in Figure 5.5, thus these events are investigated further. This indicates a possible nonlinear interaction between the SDT and the 16- as well as the 10-day wave which in turn may provide an explanation of the SDT variation during these events.

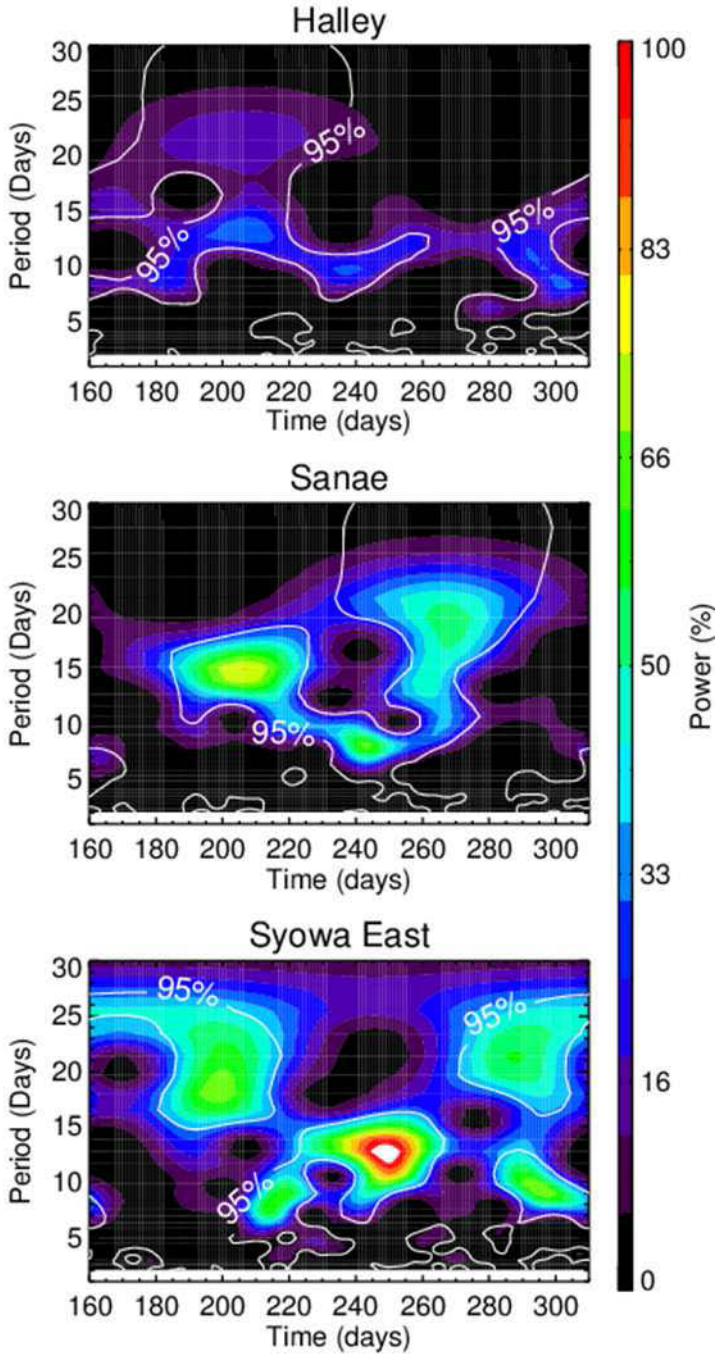

Figure 5.7: The normalized wavelet power spectra of the SDT amplitude showing the SDT modulation in the meridional MLT winds from Halley, SANAE and Syowa.

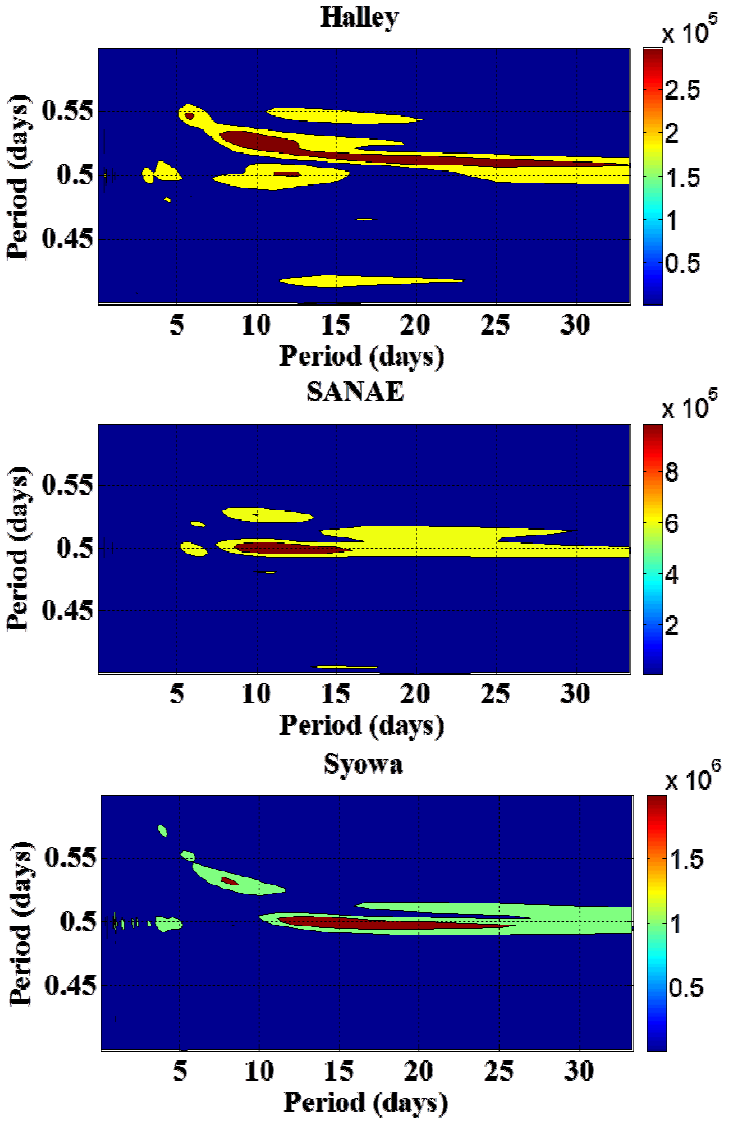

Figure 5.8: The bispectra computed from the 2002 meridional winds for time interval day 180-280.

Nonlinear interaction between the primary waves yields secondary waves whose frequency, phase, zonal and vertical wave numbers are the sum and/or difference of the primary waves (Spizzichinico, 1969; Tietelbaum and Vial, 1991). Thus before making any conclusions about nonlinear interaction, it is imperative to prove the validity of frequency, phase and the wave numbers relationship. Checking the vertical wavenumber relationship is impossible because the MLT wind data have no height resolution. Nonetheless, the bispectral analysis was used to check for the validity of the frequency and phase relationship using the fact that the bispectrum is able to retain phase information and identify any possible non-linear process that may generate phase coupling (Beard et al., 1999). Establishment of phase coupling indicates that the system produces the phase relationship that is similar to the frequency relationship. Pancheva (2000) has given a detailed description of this method and it has been used frequently in the

investigation of the mesospheric winds (Beard et al., 1999; Pancheva 2000, 2001; Pancheva and Mitchell, 2004). Figure 5.8 presents the bispectra of the meridional winds for the time interval of day 180-280 where strong modulation of SDT amplitude at 16- and 10-day periodicity is observed. The figure shows a strong interaction between the SDT and 10-day planetary wave at Halley and SANAE. Also observed at all stations is the interaction between the SDT and 12-30 day wave. Such broad peaks in the planetary wave axis are due to poor frequency resolution. In addition, interaction between the SDT and 5-day wave is also observed. The spectra also show interaction among the SDTs at all stations. The appearance of peaks in a bispectrum does not always indicate the presence of quadratic phase coupling (Beard et al., 1999). The bispectrum shows peak if frequency relationship of spectral components is the same as the phase relationship. Moreover, peaks also show in the bispectra even if a merely constant phase relationship between spectral components is noticed. This phenomenon is mostly observed during non-linear interaction among tides alone. Thus peaks which show an interaction between SDTs are doubtful whereas questionable peaks showing an interaction between tides and planetary waves are unlikely. Therefore, these results allow us to reach a conclusion about the phase and frequency relationship for the SDT and the 10- as well as the 16-day planetary waves.

5.3.4.2 Zonal wavenumber of planetary wave

Figure 5.7 revealed that the SDT amplitude is modulated at ~16 days near day 180-220 and at ~10 days near day 240-260 which is indicative of a possible nonlinear interaction between SDT and planetary waves. Therefore further investigation of a nonlinear interaction between the SDT and 16-day wave is conducted using MLT winds from day 120 to 230, while an interaction between the SDT and the 10-day wave is conducted using data from 220 to 310. The amplitude and phase of the 16-day wave were computed using the Fourier transform of the meridional component and the results are presented in the left panel of Figure 5.9 . The amplitudes from all stations are above the 95% confidence level and therefore the corresponding phases can be trusted. From the phase gradient the 16-day wave was found to be propagating westward with the zonal wavenumber s =1.2 ≈ 1. Figure 5.10 shows the instantaneous amplitude and phase of the 16-day wave from the meridional component at Halley, SANAE and Syowa computed using the analytic signal. The analytic signal is used to determine the time variation of amplitude and phase of the selected spectral component of the time series. The grey shades in the figure indicate the time interval (day 160-200) where the 16-day wave activity was simultaneously large at all stations. Therefore, the phase of 16-day wave from all stations was computed as an average over the above mentioned time interval and the results are also presented in Figure 5.9

(red triangles). The error bars indicate the standard error of the mean. The phase gradient also shows that this wave is propagating westward with the wavenumber $s = 0.69 \approx 1$.

The zonal wavenumber of the 10-day wave was computed using the same method. The right panel of Figure 5.9 shows that the amplitude of the 10-day wave is only significant at Halley and SANAE, thus the zonal wavenumber was computed using the phases from these stations. The phase gradient shows that the 10-day wave is propagating eastward with zonal wavenumber s = 1.1 ≈ 1 (from Fourier transform). The zonal wavenumber computed from the average of the phase (see Figure 5.11), also from Halley and SANAE to maintain consistency, was found to be s = 1.1 ≈ 1. Earlier observations (Dowdy et al., 2004; Espy et al., 2005) and modeling studies (Chang et al., 2009) based on 2002 data also reported that the quasi 16-day wave as the propagating westward with zonal wavenumber (*s*=1).

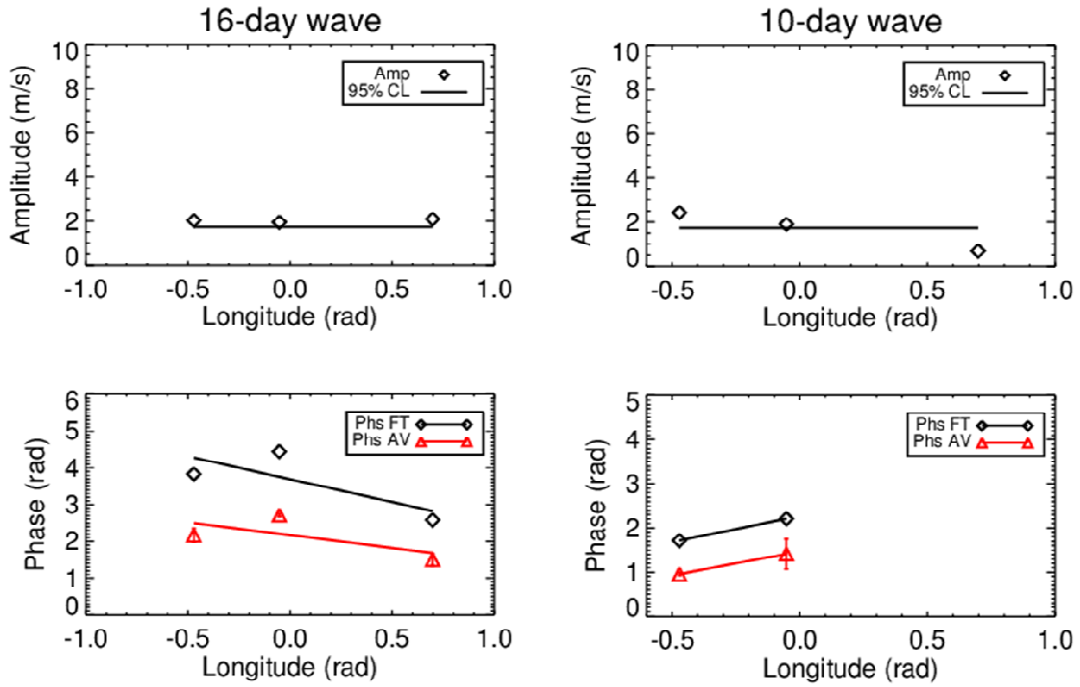

Figure 5.9: The amplitude (top) and the phase (bottom) of the 16-day wave (left) as well as the 10-day wave (right) in the meridional component. The amplitudes and phases (black diamonds) were computed using Fourier transform (FT). The phase represented with the red triangles was computed as average of instantaneous phase where the wave amplitude was maximum (see Figure 5.10 and Figure 5.11).

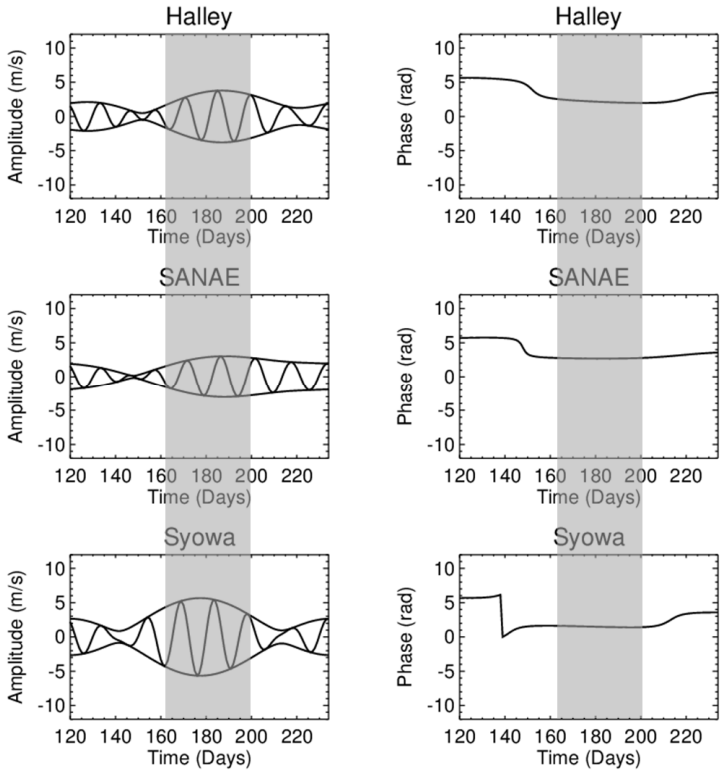

Figure 5.10: The instantaneous amplitude (left) and the phase (right) of the 16-day planetary wave from the meridional component plotted in the time interval day 120-230.

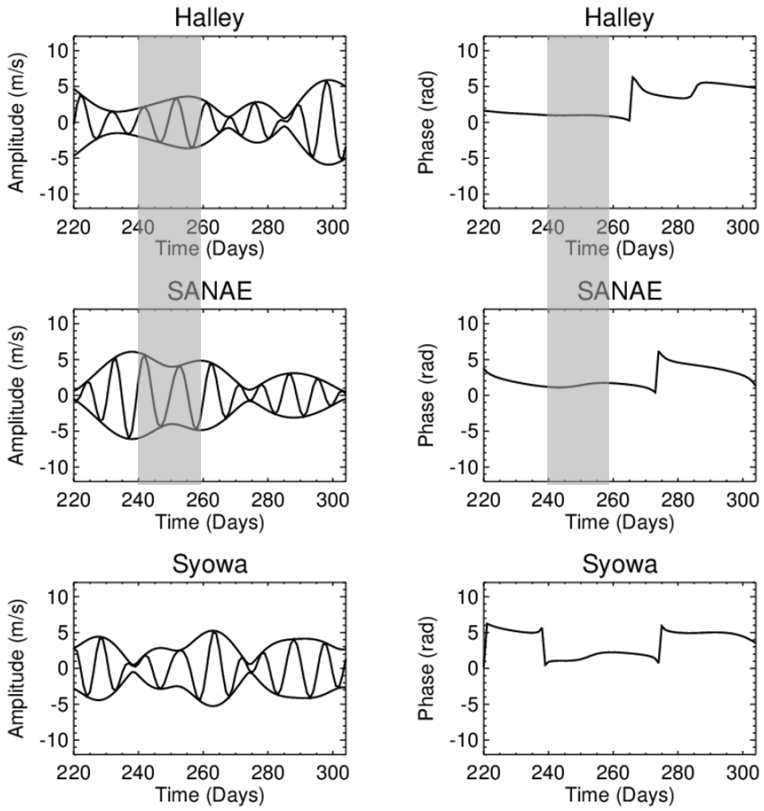

Figure 5.11: Same as Figure 5.10, but the 10-day planetary wave plotted in the time interval day 220-310.

5.3.4.3 Zonal wavenumber of SDT and secondary waves

Zonal wavenumbers of the secondary waves and SDT were computed using data intervals of days 120 to 230 and 220 to 310. Secondary waves formed during nonlinear interaction between planetary wave and the SDT have a period close to that of SDT; therefore secondary waves are extracted simultaneously with SDT. The Fourier transform of hourly wind velocity from Halley, SANAE and Syowa was computed, firstly for the time interval of day 120 to 230, which encompasses the event of strong SDT modulation at 16 days periodicity. The Fourier spectra are presented in Figure 5.12 (a) for a period range from 10 h to 14 h. Apart from the distinct peak at 12 h corresponding to the SDT, the figure also show peaks corresponding to secondary waves near 11.2 h, 11.4 h, 11.6 h, 12.2 hand 12.4 h. Some of these waves are significant as they are above the 95% confidence level, though not from all stations. The amplitude and phase of the SDT and secondary waves were extracted and plotted in Figure 5.12 (b) and (c). The phase gradient was then used to compute the zonal wavenumber and the results are presented in Table 5.1.

Table 5.1: Zonal wavenumbers (s) of the 16-day planetary wave and the SDT as well as the secondary waves computed for the time interval days 120 to 230.

Waves	16-day	SDT	11.2 h	11.4 h	**11.6 h**	12.2 h	**12.4 h**
s	-1.2	-2.4	-0.1	-0.8	**-0.1**	-0.9	**-1.7**

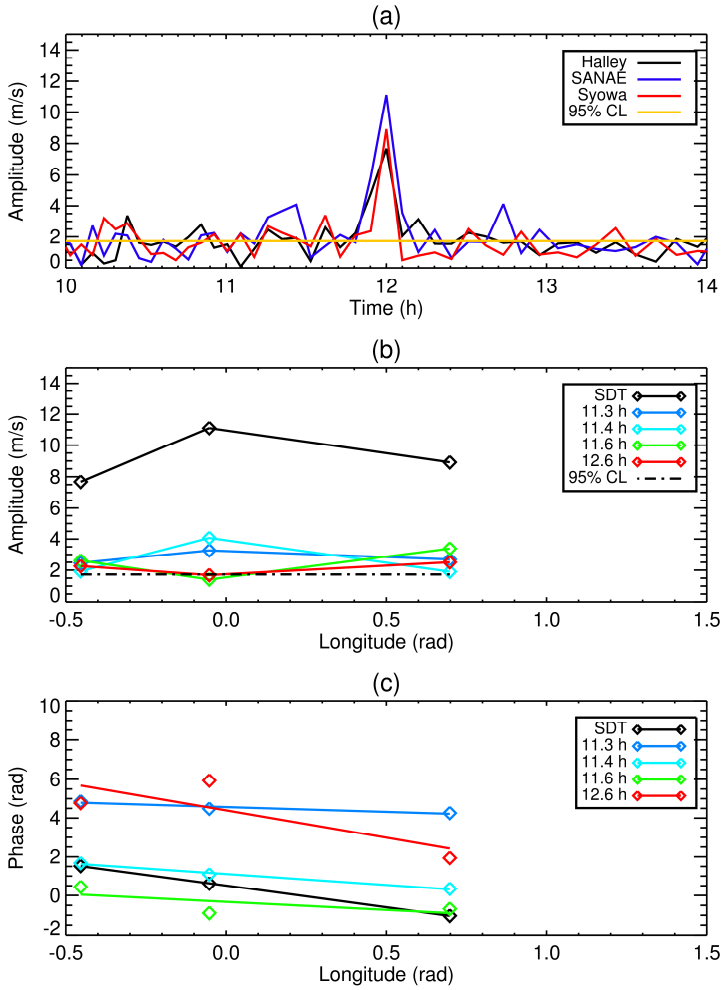

Figure 5.12: The amplitude spectra (top) of the winds computed for a time interval day 220-310. The amplitudes of the SDT and the secondary in the middle panel, the horizontal line represent the 95% confidence level. The phase of the SDT and the sum secondary waves are shown in the bottom panel.

In this investigation negative wavenumbers indicate westward propagation. The results show that the SDT has a zonal wavenumber s ≈ -2 i.e. migrating semidiurnal tide. Theoretically, nonlinear interaction between westward propagating 16-dayplanetary wave with s = 1 and migrating SDT result in the formation of westward propagating secondary waves with periods 11.6 h and 12.4 h and zonal wavenumber s = -3 and s = -1 respectively. However, the result from Table 5.1 (bold values) shows that the 11.6 h and 12.4 h secondary waves are propagating westward with zonal wavenumbers s = -0.1 and s = -1.7, which is inconsistent with nonlinear interaction between the SDT and the 16-day planetary wave. Therefore it could be deduced that SDT variation, in the time interval (day 160 to 250), was not caused by the nonlinear interaction between SDT and 16-day planetary wave. These results further supports that the SDT variation observed in the meridional component at Halley and SANAE form day 160 to 250 was possibly caused by the variation of ozone in the stratosphere. Same method was used to extract and

compute the zonal wavenumber of the SDT and the secondary waves for the time interval day 220 to 310 and the results are presented in Figure 5.13 as well as in Table 5.2.

Table 5.2: Same as Table 5.1, but for 10-day wave and for the time interval days 220 to 310.

Waves	10-day	SDT	11.3 h	**11.4 h**	11.6 h	**12.6 h**
s	1.1	-2.2	-0.5	**-1.1**	-0.8	**-2.8**

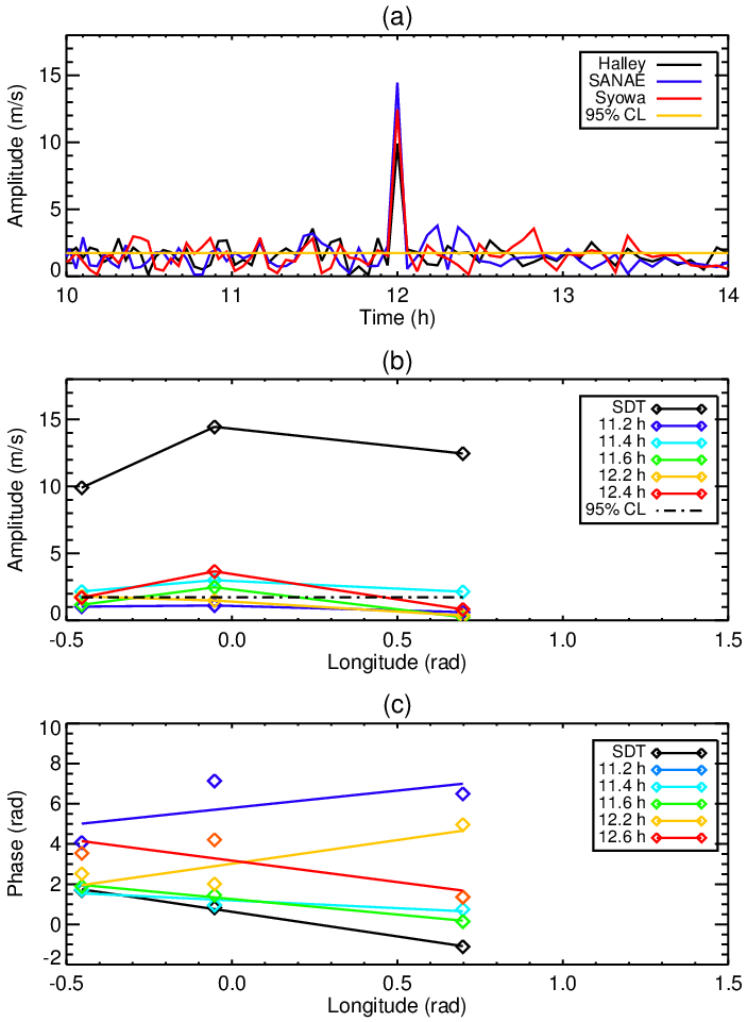

Figure 5.13: Same as Figure 5.12, but for a time interval day 120-230.

Secondary waves that would result from nonlinear interaction of the westward SDT (s = 2) and the eastward 10-day planetary wave (s = 1) are westward 11.4 h and 12.6 h components with theoretical wavenumbers s = 1 and s = 3 respectively. The results (bold values in Table 5.2) shows that the 11.4 h and 12.6 h secondary wave are propagating westward with zonal wavenumbers s = 1.1 ≈ 1 and s = 2.8 ≈ 3 respectively. This is consistent with a nonlinear interaction between the SDT and the 10-day planetary wave. Recalling that the variation of the SDT amplitude at SANAE and Halley from around day 250 to 310 (Figure 5.4) was anti-

correlated with variation of the ozone mixing ratio indicated that ozone variation was not responsible for SDT variation. Nonlinear interaction between SDT and the 10-day planetary wave, seen in Figure 5.4 and which seem to have occurred near day 240-260, is a possible mechanism responsible for the variation of SDT amplitude. Previous studies have reported the SDT variations which are caused by nonlinear interaction between SDT and planetary waves (Pancheva and Mitchell, 2004; Hibbins et al., 2007, Mthembu et al., 2013).

5.3.4.4 Further evidence of nonlinear interaction

The amplitudes of the primary waves (SDT and 10-day wave) and secondary waves (11.4 h and 12.6 h) in the time interval day 250 to 310 from Halley and SANAE were extracted using a dynamic Fourier transform which utilizes a 34-day data window which was shifted forward by one day and the results are presented in Figure 5.14. Also presented in this figure are the zonal winds from both stations. This rather longer data window yields the desired frequency resolution i.e. 0.001225 h^{-1} to resolve and extract the secondary waves. However, there is a tradeoff between good frequency resolution and time localization of the spectral components. The modulation of the SDT at 10-day periodicity shown in Figure 5.7 already indicated the approximate time where nonlinear interaction may have taken place, therefore time localization, for the purpose of the analysis was less important than good frequency resolution. Thus, the 34-day data window provides a suitable tradeoff. This method was used by Malinga and Ruohoniemi (2007) for the separation and extraction of the components (42, 48 and 52 h) of the quasi-two day wave (QTDW).

Inspection of the amplitudes of the SDT at Halley and that of the 10-day waves at both stations show a sudden decrease around day 260-265, leading to the SSW event. The SDT amplitude at SANAE on the other hand shows a steady decrease from day 250 to 310. The 12.6 h secondary wave at Halley seems to suddenly increase from day 265; however no enhancement of other secondary waves was noticed. This event coincide with the modulation of SDT at 10 day periodicity (Figure 5.7) and this behavior further supports the possible nonlinear interaction between the 10-day wave and the SDT where the decrease in SDT and 10-day wave amplitudes is understood to be due to energy loss during the formation of the secondary waves. The reversal of zonal wind at SANAE took place just after day 260 and persisted until day 273, thereby creating unfavorable conditions for the westward propagating secondary waves which then suppressed their enhancement at SANAE. The zonal winds at Halley were propagating eastward from day 265 to 270 and that created favourable conditions for the enhancement of the westward propagating 12.6 h secondary wave at Halley. However the suppression of the 11.4 h secondary wave at Halley is not understood. Chang et al., (2009) investigated the 2002 SSW

using the NCAR Thermosphere Ionosphere Mesosphere Electrodynamics General Circulation Model (TIMED-GCM) and their results revealed an anti-correlation between the migrating semidiurnal tide (primary wave) and the nonmigrating tide (secondary wave) which is in agreement with the present results.

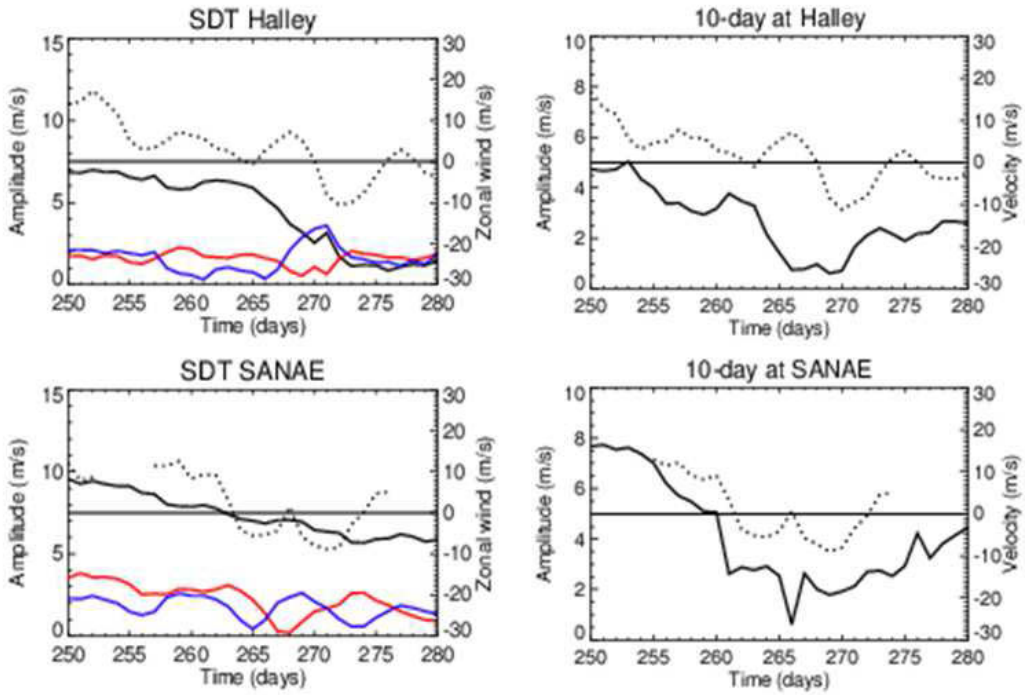

Figure 5.14: The left panel shows time variation of the amplitude of the SDT (black), 11.4 h (red) and 12.6 h (blue) secondary waves computed from the meridional component. The dotted line indicates the zonal winds where positive (negative) wind velocity represents eastward (westward) winds. The right panel shows the time variation of the amplitude of the 10 day wave from the meridional component.

The mechanism behind the SSW event as outlined by Matsuno (1971) involves interaction between planetary waves and zonal mean flow in the stratosphere which result in upward and poleward heat and momentum flux which is accompanied by deceleration and/or reversal of eastward zonal winds in the stratosphere. Connected with the SSW are the weakening and/or reversal of eastward zonal winds in the MLT region (Gregory and Manson 1975; Cevolani 1989; Singer et al., 1994). Although this phenomenon has mostly been observed in the northern high latitude (Hoffmann et al., 2002; Manson et al., 2006), its occurrence has been reported in the Southern hemisphere as well (Dowdy et al., 2004, Mbatha et al., 2010). Therefore, based on the current result the 10-day planetary wave observed near day 240-260 is believed to have contributed in driving the SSW event. Furthermore, nonlinear interaction with the SDT may have taken place and this process resulted in the weakening of the amplitude of SDT and the 10-

day planetary wave which was accompanied by the enhancement of the secondary wave (12.6 h at Halley).

5.4 Summary

The 2002 major SSW event is characterized by a sudden enhancement of temperature of about 35 K over 80°S and 10 hPa as well as the reversal of zonal-mean zonal winds over 60°S and 10 hPa pressure level. The reversal of the MLT zonal winds recorded at SANAE, Halley and Syowa HF radar were found to take place about 8 day before the reversal at stratospheric level and this is in accordance with what has previously been reported (Dowdy et al., 2004; Hoffmann et al., 2007; Mbatha et al., 2010).

The behavior of the SDT was investigated before, during and just after the SSW event (day 160 to 310). The Spectral analysis of the winds revealed the presence of tides as well as planetary wave activity. The SDT is formed in the stratosphere by absorption of solar radiation by ozone, therefore variation of the ozone mixing ratio was investigated as a possible forcing mechanisms of the SDT. For this analysis, variability of ozone mixing ratio was investigated and the results show that there are times where its variability is correlated with that of the SDT (especially from day 160 to 250 in the meridional component at Halley and SANAE as well as from day 160 to 230 in the zonal component at SANAE and Syowa). This behavior hinted to a variation of ozone mixing ratio as a possible cause of the SDT variation in this time interval. However, an anti-correlation between the SDT amplitude and the ozone mixing ratio was observed from around day 250 to 310 (especially in the meridional component at Halley and SANAE) and this ruled out the ozone variation as a possible cause of SDT variation. Following the observation of planetary waves, nonlinear interaction between the SDT and planetary waves was investigated as a possible contributing factor in the SDT variation from day 160 to 250 and as a possible cause of SDT variation from day 250 to 310.

The investigation of planetary waves in the MLT region revealed, among others, the presence of 10-day wave activity in the meridional component near day 240 to 260 and the 16-day wave near 180 to 220 from all stations. These waves were also found in the stratosphere using the geopotential height from NCEP reanalysis data. Additionally, their phases were found to fall with height indicating an upward propagation. Therefore, it was postulated that planetary waves observed in the MLT region may have been excited from a lower level of the atmosphere and propagated upward. In the process, they may have interacted nonlinearly with the SDT and modulated its amplitude at periods corresponding to that of planetary waves.

The modulation of the SDT amplitude was investigated using wavelet analysis and the results indeed show some modulation of the SDT amplitude at periods close to 5, 10, 16 and 23 days. However, attention was paid to the modulation of the SDT amplitude at 16-day periodicity near day 180-220 and that at 10-day periodicity near day 240-260 as they coincide with the 16- and 10-day planetary wave activity. The Bispectral analysis computed in the time interval day 180 to 280 which encompasses the period where strong modulation was observed further showed interaction between 5, 10 and 12-30 days. This indicates a possible nonlinear interaction between the SDT and the planetary waves of these periods which in turn may provide an explanation of the SDT variation during these events.

The data from day 120 to 230 was used to investigate possible interaction of the SDT with the 16-day wave while data from day 220 to 310 was used to the investigate interaction of the SDT with the 10-day wave following observation of strong SDT modulations during these time intervals (see Fig. 7). The phase computed from the Fourier transform and instantaneous phase were used to compute the zonal wavenumber of the 16-day and the 10-day waves in the meridional component. The phase gradient revealed 16-day wave as a westward propagating wave with the zonal wavenumber $s \approx 1$ while the 10-day wave was found to propagate eastward with $s \approx 1$. Fourier transform revealed that the zonal wavenumber of the SDT was $s \approx 2$ while that of 11.6 h and 12.4 h, resulting from the interaction between the SDT and the 16-day wave were found to be $s \approx -0.1$ and -1.7 which was, however inconsistent with nonlinear interaction. These results rule out nonlinear interaction between the SDT and the 16-day wave as the cause of the SDT variation from day 120 to 230, leaving the ozone variation as a possible candidate as observed in the meridional component at Halley and SANAE.

The zonal wavenumbers of the 11.4 h and 12.6 h secondary waves computed from day 220-310 were found to be $s \approx -1$ and -3 respectively. These results are consistent with nonlinear interaction between the SDT and the 10-day wave. Further evidence of nonlinear interaction was revealed from the temporal variation of SDT, 10-day wave and secondary waves in the time interval day 250-310. Inspection revealed a decrease in amplitude of the SDT and the 10-day wave and an increase in amplitude of the secondary wave (especially 12.6 h from Halley) few days before the SSW. The decrease in amplitude of the primary waves is consistent with the energy loss during the formation of secondary waves. The reversal of zonal winds especially at SANAE created unfavorable condition for the secondary waves and to a larger extent suppressed their enhancement. While the suppression of the 11.4 h wave at Halley is not understood, the 12.6 h wave was enhanced during favorable conditions i.e. when the zonal winds were propagating eastward.

Therefore, while the SDT variation before the SSW (day 160 to 250) could be linked with the variation of ozone mixing ratio, the anti-correlation observed from day 250 to 310 between SDT and ozone mixing ratio suggests different mechanism as a possible cause. The planetary wave (10-day wave) observed around day 240 to 260 is believed to have interacted with zonal mean winds and contributed to the triggering of the SSW. In the process nonlinear interaction between the SDT and the 10-day wave may have taken place, resulting in the formation of secondary waves which was accompanied by the decrease in the SDT and the 10-day wave amplitudes.

6 Studies on planetary waves and tide interaction in the mesosphere-lower thermosphere region using meteor radar data from Rothera (68°S, 68°W), Antarctic

6.1 Introduction

The mesosphere-lower thermosphere (MLT) region is very dynamic due to the processes taking place in this region. The variability of tidal amplitudes as usually observed in winter contributes significantly to the MLT region dynamics. The variability of tides may range from a time scale of few days to years. Numerical (Spizzichinico, 1969; Teitelbaum and Vial, 1991) and observational (Mitchell et al., 1996; Beard et al., 1999; Jacobi, 1999; Pancheva, 2000; Pancheva and Mukhtarov, 2000; Pancheva, 2001; Pancheva et al., 2002; Pancheva and Mitchell, 2004) studies have been conducted with an aim of explaining such tidal variability and a number of mechanisms were proposed as being responsible and are summarized in Pancheva (2001). The proposed mechanism include (1) variation in tidal forcing such as ozone in the stratosphere, water vapour in the troposphere, release of the latent heat (Hagan, 1996; Hagan et al., 1997) and changes in the solar flux, (2) changes in the region through which tides propagate, (3) variation in eddy diffusion and/or dissipation (Geller et al., 1997) and (4) non-linear interaction between tides and planetary waves (Teitelbuam and Vial, 1991).

The focus of this chapter is an investigation of tidal variability caused by non-linear interaction between tides and planetary waves. Theoretical studies of non-linear interaction between waves in the MLT region was pioneered by Spizzichinico (1969). Teitelbuam et al. (1989); Teitelbuam and Vial (1991) followed in their footsteps and proposed a mechanism that could explain how planetary waves could contribute to the variability of tides. The mechanism proposed that non-linear interaction between primary waves (tides and planetary waves) result in the generation of secondary waves whose frequency, phase and wave number are sums and/or differences of the primary waves. The period of the planetary wave is significantly longer than that of the tide, thus frequencies of secondary waves are close to that of tide, and consequently the secondary waves beat with the tide and modulate the tidal amplitude at periods corresponding to that of the planetary wave. Observational evidence of tidal variability caused by this mechanism was reported, more so in the Northern hemisphere (Mitchell et al., 1996; Beard et al., 1999; Jacobi, 1999; Pancheva, 2000; Pancheva and Mukhtarov, 2000; Pancheva, 2001; Pancheva et al., 2002; Pancheva and Mitchell, 2004) than in the Southern hemisphere (Pancheva and Mitchell, 2004).

The high latitude semidiurnal tide normally dominates over the diurnal tide (DT) and thus most non-linear interaction of waves at high latitude are between the semidiurnal tide and planetary waves (Manson and Meek, 1991; Burrage et al., 1995; Mitchell et al., 2002). It has been reported that non-linear interactions of waves may take place in the lower heights (Carter and Balsley, 1982; Mitchell et al., 1996) and secondary wave may propagate to the MLT region whereas planetary waves may be precluded. In this case, the planetary wave signature will be absent in the MLT region. However, in-situ non-linear interaction may also takes place and in this case planetary wave features will be imprinted in the MLT region.

Numerous studies have been conducted to investigate planetary wave activity in the Southern hemisphere (Luo et al., 2000; Espy et al., 2005; Murphy et al., 2007; Day and Mitchell, 2010a, 2010b). These studies revealed that the observed waves have periods around 23, 16, 10, 5 and 2 days with maximum activity in winter. The winter-time 23-day waves are proposed to be associated with the solar rotation period (Luo et al., 2001; Pancheva and Mitchell 2004) while the 5-, 10- and 16-day waves are related to the well know normal modes (Salby, 1984). Day and Mitchell (2010a), (2010b) have investigated the 5- and 16-day planetary wave activity, respectively, using the same data set as that used in this study. They investigated the temporal and vertical variation of the wave activity using the variance as a proxy for the wave activity. A different technique was used in the current analysis to investigate this variation and the results from Day and Mitchell (2010a), (2010b) are used to complement some of the results obtained in this study. The climatology of tides in this region is presented in Chapter 4 and this chapter investigates the non-linear interaction between tides and planetary waves.

The principal objective of this chapter is to investigate the in-situ non-linear interaction between tides and planetary waves in the Southern hemisphere and to explore the connection between this process and the variability of the tidal wave observed in the MLT region. This analysis is divided into 4 sections which includes (1) investigation of the presence of planetary waves in the MLT region using wavelet transform (2) investigation of tidal modulation using dynamic Fourier transform (3) possible non-linear interaction between planetary waves and tides was investigated using bispectral analysis and (4) secondary waves were extracted using Fourier transform and their wavelength and wave number were computed using linear least-squares best fit method.

6.2 Data set and method of analysis

The data used in this study are recorded from meteor radar located at Rothera, Antarctica. The hourly wind velocity data collected from February to December 2005 show planetary wave

activity and thus were used to investigate the variability of tides in the MLT region. An investigation on the wind data from 2005 to 2008 was made to search for a simultaneous occurrence of SDT modulation (see Section 6.3) and planetary wave activity, which could indicate a possible non-linear interaction. This phenomenon was observed only in the 2005 data and thus was used in this study. There are no data before February as this radar was only operational from February 2005. There were a day or two data gaps randomly and those were linearly interpolated prior to determine the wave amplitude and phase.

6.3 Results and discussion

The first task in this analysis was to identify the tidal and planetary wave spectral components in the wind velocity data. Planetary waves in the MLT region are non-stationary and transient and thus require a superior analytical technique to investigate their time of occurrence as well as the temporal variation of their amplitudes. Wavelet analysis, due to its capability of providing the required information, proved to be suitable for this kind of investigation. The spectral content of the wind velocity data was investigated by computing wavelet power spectra using the Morlet wavelet from six different heights and the spectra are presented in Figure 6.1 for a period from 0 to 30 days. The left panel shows the spectra for the zonal component while the right panel is for the meridional component. The power spectra in Figure 6.1 to Figure 6.3 have been normalized by dividing each value by the maximum value of the power spectrum and thereafter multiplying by 100 %, hence the relative power ranges between 0 % for the minimum and 100 % for the maximum. The Morlet wavelet transform is widely accepted in the scientific community and have been used by many researchers for calculating the spectral amplitude and phase (Malinga and Ruohoniemi, 2007; Pancheva and Mitchell, 2004)

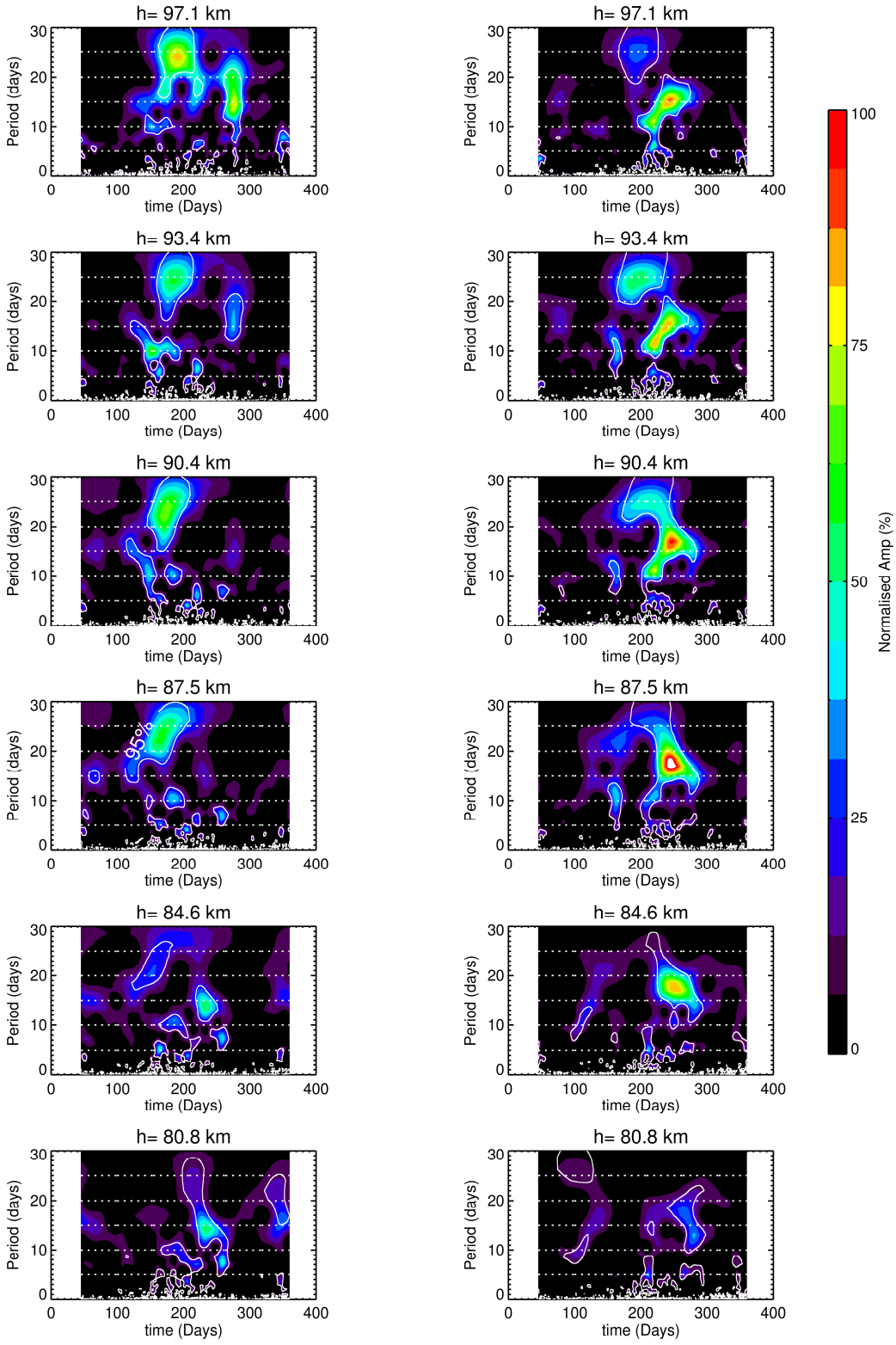

Figure 6.1: Normalised wavelet spectra of the zonal (left panel) and meridional components (right panel) of the wind velocity for a period range of 0-30 day and for different altitude. A 95% confidence level is indicated with white contour lines. The white horizontal dotted lines indicate a period every 5 days.

It is evident from Figure 6.1 that the power spectra of the zonal component show a strong winter planetary wave activity of different periodicities of ~ 5, 10, 16 and 23 day as well as little summer activity only observed at the lowest altitude. It is noted here that the above said periodicities, 5, 10, 16 and 23 days correspond to the broader spectral components for the periods in range 4-8, 8-12, 12-20 and 17-27 days. The above said nomenclature is utilized throughout the chapter. Broad ranges such as these are also reported by earlier researcher (Luo et al., 2002). These peaks are significant as shown by a white contour line which indicates the 95% confidence level. The confidence level was computed using the chi-square method which assumes that the time series can be modeled as red noise (Torrence and Compo, 1998). If a peak in the wavelet power spectrum is above the red noise then this peak is considered to be a true feature with a certain level of confidence. In this instance it is set at 95%. The dominant planetary waves are those with a period approximately 23 days and are observed in winter around day 150 starting at 84.6 km altitude and intensifying with altitude. During summer (day 300-350), a slightly weaker 23-day planetary waves are observed at 80.8 km altitude only. It is known that in summer planetary waves are unable to propagate up to the MLT region. Thus, during summer, the presence of waves in this region may be attributed to, among other processes, ducting of planetary waves from the winter hemisphere to the summer hemisphere (Garcia et al., 2005; Riggin et al., 2006; Day and Mitchell 2010a). An approximately 14-day wave activity near day 230 is observed from 80.8 km and disappears at 87.5 km. This wave coincides with that observed by Day and Mitchell (2010b) in the zonal component of the same data set at an altitude of ~85 km. In addition, planetary wave with period of 10 days are also observed near day 200 from 80.8 km altitude. Its amplitude increased with height until 87.5 km and thereafter decreased and eventually disappears at 97.1 km. A near 5-day planetary wave was observed near day 250 at all heights. This wave activity again coincides with that observed by Day and Mitchell (2010a).

The wavelet power spectra of the meridional component show numerous peaks corresponding to planetary waves with a period ~5, 10, 16 and 23 days. Planetary wave activity with a period of 23 days was observed at higher altitudes (90.4 to 97.1 km) only around day 200. The 16-day planetary wave is dominant and is observed in winter near day 250 for the altitude region between 84.6 km and 93.4 km. The amplitude of this wave is weak at 80.8 km and increases with altitude reaching maximum at 87.5 km. A weak 10-day planetary wave is observed near day 100 but it is significant only at low altitude. The 5- and 10-day waves are observed near day 200 at all heights with their intensity being low at lower heights. The 5- and -16-day waves observed here were also observed by Day and Mitchell (2010a, b) in the meridional component.

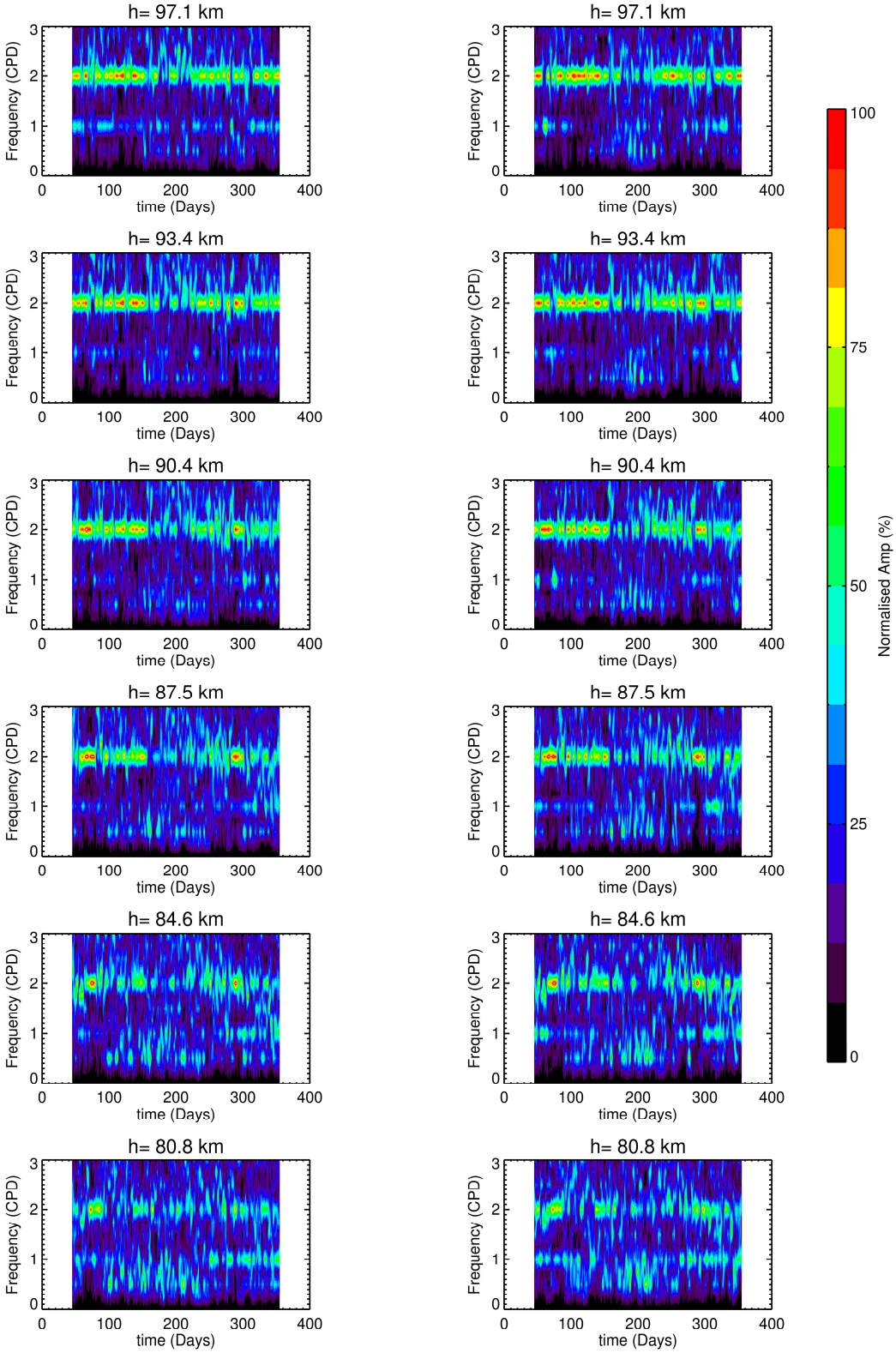

Figure 6.2: Normalised dynamic Fourier spectra of the zonal (left panel) and meridional (right panel) components of the wind velocity for a frequency range of 0-3 day and for different altitudes.

The presence of the tidal waves was investigated by plotting a dynamic spectrum, shown in Figure 6.2, computed using short term Fourier transform (STFT). In the STFT, Fourier transform of a 4-day data window is computed and attributed to day 1. The window is then shifted by one day and the computed spectrum is attributed to day 2. This procedure is repeated until the end of the time series and at all altitude levels. The spectral components are presented in terms of frequency in cycles per day (CPD) where 0.5, 1 and 2 CPD indicate quasi-two day waves (QTDW), DT and SDT, respectively. Both zonal and meridional components show signatures of SDT, DT and quasi two day waves (QTDW). The SDT activity intensifies with altitude and is dominant over the DT. Manson and Meek (1991); Burrage et al. (1995); Mitchell et al. (2002) also found that SDT at high latitude and in both the hemispheres is stronger than the DT. The DT activity is weak at almost all heights for both components except at 97.1 km in the zonal wind. The QTDW are observed in winter for both components with a stronger activity in the zonal component than in the meridional component. For the purpose of the analysis the SDT was of more interest due to its dominance over the DT and furthermore, the SDT is found to be strongly active in the coupling with longer period planetary waves than DT (Pancheva, 2000).

The variability of the SDT was investigated by first applying the band-pass filter to suppress the periods below and above 10 and 14 h respectively. The results are not represented here but they show the variation of the velocity of the SDT which is characterized by increasing velocity with altitude from ~40 m/s at 80.4 km to ~80 m/s at 97.1 km altitude for both components. Another important feature of the SDT is the temporal variation of its amplitudes as well as the amplitude modulation which is normally caused by the interaction with planetary waves. However, it is still impossible to identify the modulation period at this stage. Intense investigation into the causes of the SDT variation has been carried out before and the proposed possible mechanisms are summarized in Pancheva (2001). The main assertion were the variation in tidal forcing (Hagan, 1996; Hagan et al., 1997), the changes in the region through which tides propagate, variation in eddy diffusion and/or dissipation (Geller et al., 1997) and non-linear interaction between tides and planetary waves (Teitelbuam and Vial, 1991). Non-linear interaction between tide and planetary wave are investigated as a possible cause of the tidal variability.

The SDT modulation was investigated by computing wavelet transform of the daily SDT amplitudes and the spectra are shown in Figure 6.2 where the left panel is for the zonal component and the right panel is for the meridional component. The daily values of the SDT amplitudes were extracted from Figure 6.3. The zonal component shows several peaks corresponding to periods ~5, 10 and 16 day which are less dominant than the peak

corresponding to 23 days, thus are not considered. The most important feature in this component is the peak corresponding to approximately the 23-day wave observed in winter. The modulation of the SDT amplitude in this period coincides with a 23-day planetary wave activity observed in the zonal component in Figure 6.1. The variability of the SDT at the period of 23 days is stronger at lower altitude (84.6 km) and then decrease with altitude reaching minimum at 97.1 km

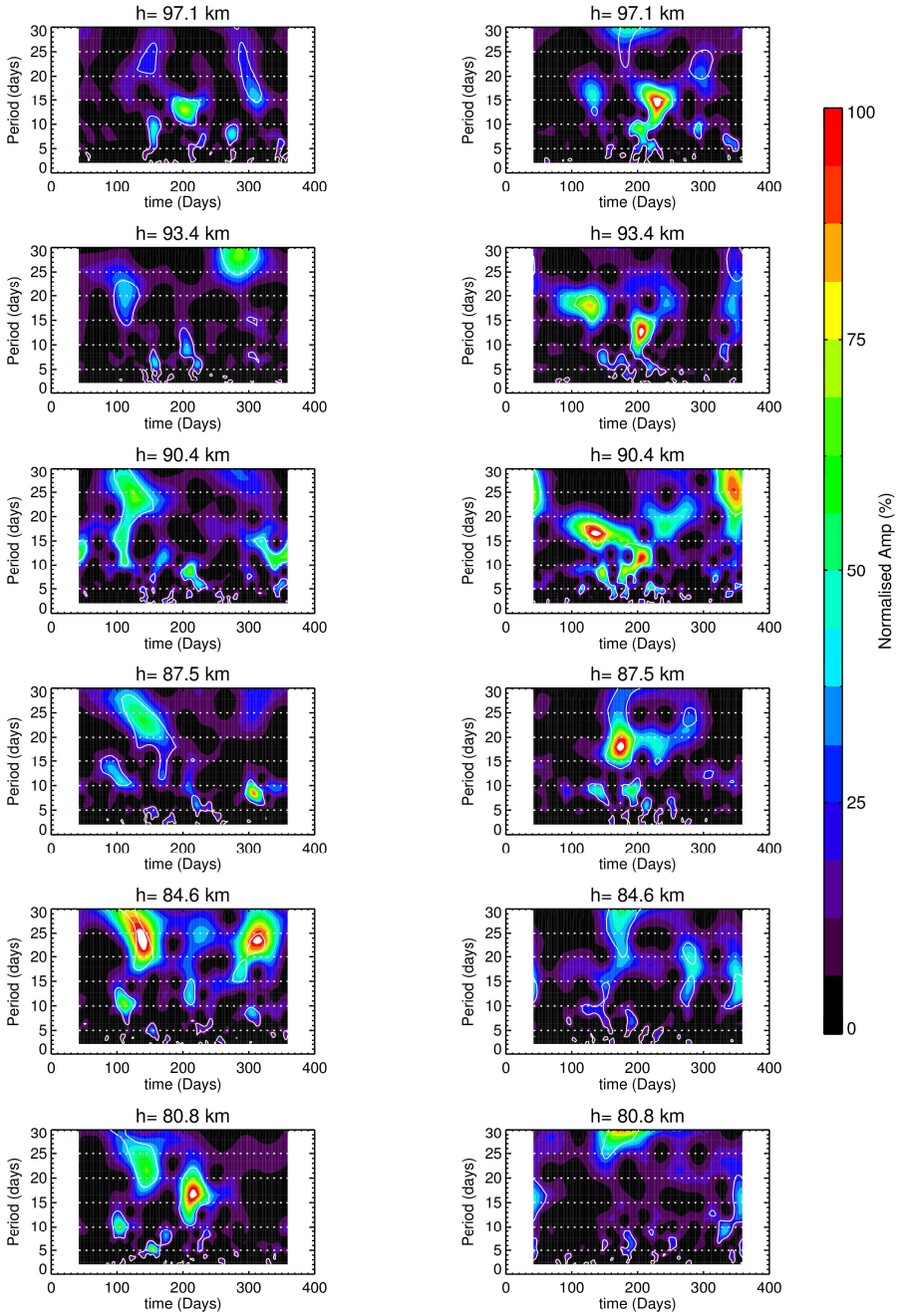

Figure 6.3: Normalised wavelet spectra of the SDT amplitude of the zonal (left panel) and meridional (right panel) component for different altitudes. A 95% confidence level is indicated with white contour lines. The white horizontal dotted lines indicate period every 5 days.

The meridional component show peaks of ~ 5 and 10 day periodicities near day 200 as well as the peak corresponding to 16 day periodicity near day 250. These peaks coincide with the planetary wave activity of similar period observed in the meridional component of Figure 6.1. The modulation of SDT at the period of 16 days is observed from 84.6-97.1 km, similar to the behaviour of the 16-day wave in Figure 6.1. The modulation of SDT at period of 5 and 10 days is observed at all heights similar to the planetary wave activity at these periods. These observations suggest a possible non-linear interaction between planetary waves and SDT which resulted in the variability of SDT. To prove this, further investigations were performed on the 23-day wave in the zonal wind as well as the 5-, 10- and 16-day waves in the meridional wind.

Non-linear interaction between the planetary wave and SDT results in the formation of secondary waves. The secondary waves, if they have large enough amplitude, beat with the SDT causing the modulation of tidal amplitude at periods corresponding to those of the planetary wave. Theoretically, non-linear interaction between the primary waves (SDT and planetary waves) results in the formation of secondary waves whose frequency, phase, zonal and vertical wave numbers are sum and/or difference of the primary waves (Spizzichinico, 1969; Tietelbaum and Vial, 1991). Mathematically the secondary waves are given by

$$x = A(t)\sin(\omega t + k_v h + k_z z - \Phi)\ ,$$

Equation 6.1

where $\omega, k_v, k_z \ and \ \Phi$ are frequency, vertical and zonal wave numbers and phase given by $\omega = \omega_{SDT} \pm \omega_{PW}, k_v = (k_v)_{SDT} \pm (k_v)_{PW}, k_z = (k_z)_{SDT} \pm (k_z)_{PW}$ and $\Phi = (\Phi)_{SDT} \pm (\Phi)_{PW}$.

Therefore to add weight to the proposition of non-linear interaction, it is required to prove the validity of the frequency, phase and the wave number relationship. Due to the single station measurement, checking the validity of the zonal wave number relationship is not possible. However, bispectral analysis was used to check for the validity of the frequency and phase relationship. This was based on the fact that bispectrum is able to retain the phase information and identify a possible non-linear process that may generate phase coupling. The demonstration of phase coupling indicates that the system yields the phase relationship that is similar to the frequency relationship. The detailed description of this method can be found in Pancheva (2000). This method has been frequently used in the investigation of the mesospheric winds (Beard et al., 1999; Pancheva 2000, 2001; Pancheva and Mitchell, 2004). The bispectra of the zonal component of the wind computed for a time interval of day 100-270 which includes all the episodes of tidal modulation observed in Figure 6.3 is shown in the left panel of Figure 6.4 .

The interaction between the SDT and the 20-35-day planetary wave is observed in all heights. The broader peaks on the planetary wave axis are due to poor frequency resolution. Similar analysis was conducted by Pancheva and Mitchell (2004) using meteor radar data from Esrange (68°N, 21°E) collected from October 1999 to December 2002 and found the interaction between SDT and planetary wave of period 22 to 24 days. Interaction between the SDT and the 5- as well as 10-day waves are also observed but could not be investigated further in the zonal component because this phenomenon is not observed at all heights. It is worth mentioning that the appearance of the peaks in the bispectrum does not always indicate the presence of the quadratic phase coupling (Beard et al., 1999). The bispectrum shows a peak if the frequency relationship of the spectral components is the same as the phase relationship as shown above (see Pancheva and Mitchell (2004)). However, the bispectrum also shows a peak although the phase relationship is not the same as the frequency relationship but instead a merely constant phase relationship between the spectral components is noticed. This phenomenon is mostly observed during the non-linear interaction among tides alone. Since the investigation of tides and planetary waves is investigated here, dubious peaks are unlikely.

The meridional wind in the right panel of Figure 6.4 shows the interaction between the SDT and the 23-28 day planetary waves for the height region from 80.8 to 93.4 km. This bispectrum was computed for the same time range as that used in the zonal component. The interaction between the SDT and the 5, 10, and -16 day wave is also observed over the height region. The 23 day wave in the meridional component in Figure 6.1 is observed at higher altitude only from 87.5 to 97.1 km. However bispectra of this component show interaction of the 23-day wave and the SDT at lower altitude as well, indicating that the interaction could have taken place at a lower height and the planetary wave may not have propagated to the MLT region due to a filtering process, This explains the absence of the 23-day wave in the meridional component at the lower MLT region. This makes the computation of the wavenumber/wavelength difficult, consequently further investigation on this wave was not undertaken. However, the 5, 10 and 16 day waves were further investigated. Based on these results a conclusion about the frequency and phase relationship between the SDT and the 23-day wave in the zonal component as well as between the SDT and 5, 10 and 16 day waves in the meridional component is reached. These observations, however, do not yet give us any assurance of the existence of the non-linear interaction, therefore the validity of the vertical wave number relationship was investigated next.

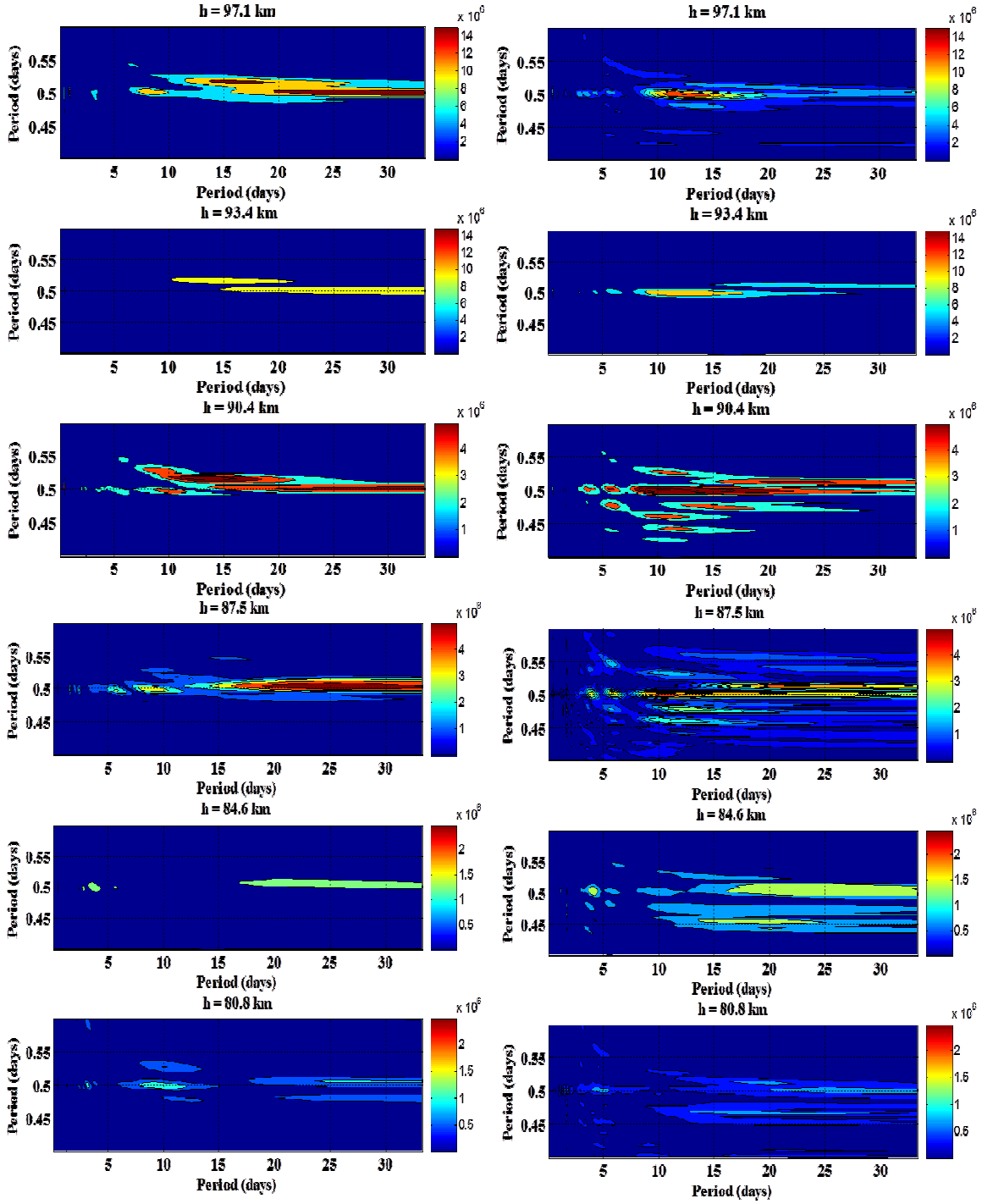

Figure 6.4: Bispectra computed from the zonal (left) and the meridional (right) component of hourly winds velocity for a time interval day 100-270.

6.3.1 The 23-wave in the zonal component

The temporal and vertical variations of the 23-day planetary wave were investigated by computing the instantaneous amplitude and phase using an analytical signal which is given by $AS(t) = f(t) + jHi(t)$ where $f(t)$ is a real function and $H(t)$ is the Hilbert transform (Brook and Wyne, 1998). The analytical signal is used to investigate the time evolution of the amplitude and phase of a particular spectral component. This method works well with the monochromatic signals, thus the 23-day planetary wave component was isolated by suppressing the periods less than 19 days and those greater than 27 days. The instantaneous amplitude and phase were computed as amplitude and phase of the analytical signal and presented in Figure 6.5 (a) for the amplitude and Figure 6.5 (b) for the phase. Figure 6.5 (a) shows a strong winter activity of the 23-day planetary wave observed from day 100 to 270. This figure also affirms that the 23-day wave activity is less at lower altitudes but then intensifies with height in agreement with what has been observed in Figure 6.1. Figure 6.5 (b) shows the variation of the phase of this component and it is apparent that the phase falls with altitude, particularly in the time range where the amplitude is maximum.

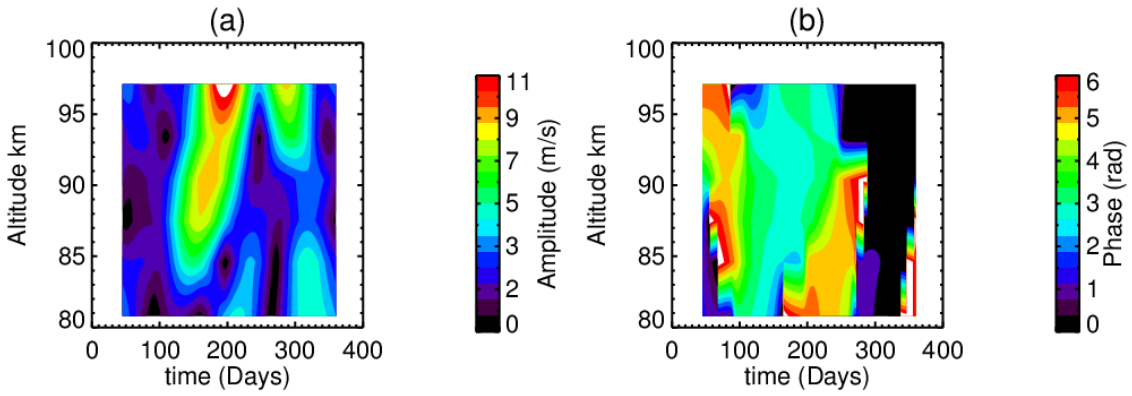

Figure 6.5: Altitude-time map of instantaneous amplitude (a) and phase (b) of the 23-day waves computed as amplitude and phase of the analytical signal.

The Fourier transform was used to extract the amplitude and phase of the 23-day wave at different heights from day 100 to 270 where the planetary wave activity is maximum as shown in Figure 6.5 (a). Figure 6.6 shows the amplitude (left) and phase (right) of the 23-day wave at different heights. The dotted line in the left panel shows a 95% confidence level thus the amplitudes are significant and the phases are not questionable. Linear least-squares best fit is used to determine the wavelength and thus the vertical wavenumber of the 23-day wave from the phase gradient. The vertical wavelength/wavenumber of the 23-day wave was found to be 50 km/0.124 rad/km. The slope is negative indicating that this is an upward propagating wave.

The wavelength of the 23-day wave found by Pancheva and Mitchell (2004) in the Northern hemisphere zonal wind was 95 km.

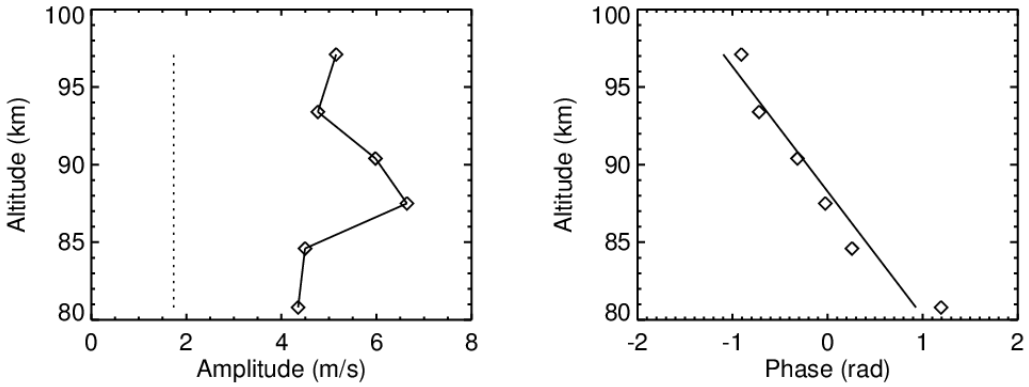

Figure 6.6: Amplitude (left) and phase (right) of the 23-day wave plotted as function of height computed with data from day 100 to 270. The dotted line indicates the 95% confidence level.

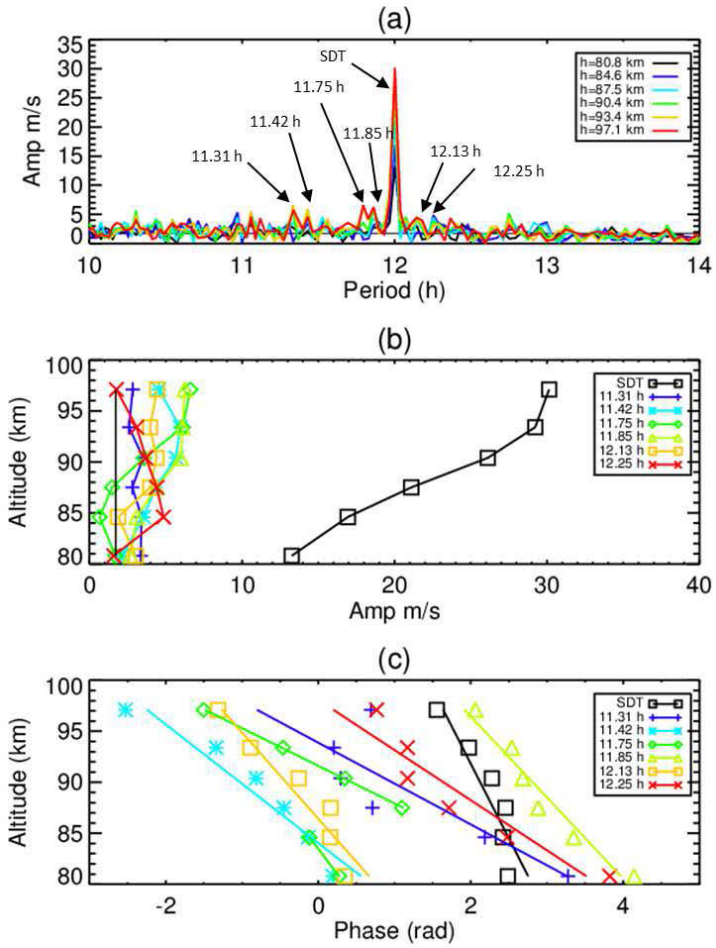

Figure 6.7: (a) Amplitude spectra of the wind velocity computed for a time interval day 100-270. (b) The amplitude of the SDT and the sum secondary waves as a function of height. The solid black line indicates the 95% confidence level. (c) The phase of the SDT and the sum secondary waves as a function of height. The solid lines indicate the linear least-squares best fits.

Generally, planetary waves found to have significantly longer periods compared to tides and the generated secondary waves have periods which are very close to that of the tides. Thus it is necessary to extract the tide and secondary waves simultaneously. The extraction of the tides and secondary waves was done using the zonal component of the wind velocity data from day 100 to 270 where the tidal modulation was stronger. Fourier transform of the data from different heights was computed and presented in Figure 6.7 (a) for a period ranging from 8 to 16 h. The horizontal line in the figure indicates the 95% confidence level. Apart from the dominant peak corresponding to the SDT which is observed to intensify with height, numerous peaks, shown with arrows, with a period of ~11.31 h, 11.42 h, 11.75 h, 11.85 h, 12.13 h and 12.25 h are observed and they correspond to secondary waves which are believed to be the result of a non-linear interaction between SDT and planetary waves. The frequencies of the SDT and the secondary waves are 0.08333 h^{-1}, 0.08842 h^{-1}, 0.08764 h^{-1}, 0.08511 h^{-1}, 0.08434 h^{-1}, 0.08244 h-1 and 0.08163 h-1 respectively. The length of the velocity time series used is 2700 and the sampling period is 1 h and this yields the frequency resolution of 0.00024 h^{-1} which is good enough to enable the separation and extraction of the secondary waves. The amplitude and phase of the SDT and the secondary waves were extracted from different altitudes and presented in Figure 6.7 (b) and Figure 6.7 (c). The amplitudes of the SDT and the secondary waves are significant as they are above the 95% confidence level shown with a dotted line, except for the 11.75 h secondary wave which is significant only at altitudes above 90 km. The gradient of the best fit line of the phase profile in Figure 6.7 (c) was used to compute the wavelengths/wavenumbers of these waves. The phase gradient shows that these waves are propagating upward. The wavelength of the SDT, 11.31 h, 11.41 h, 11.75 h and 11.80 h secondary waves were found to be approximately 89 km, 26 km, 33 km, 21 km, 52 km, 53 km and 30 km respectively. The 11.75 h wave is of particular interest as it corresponds to the secondary wave resulting from the interaction between the SDT and the 23 day planetary wave. The phase gradient and thus the wavelength/wavenumber of the 11.75 h wave were computed using the phase from altitudes above 90 km, where its amplitude is significant. Pancheva and Mitchell (2004) found the 11.75 h secondary wave and SDT wavelength of 38 km and 67 km, respectively, in the zonal wind. Theoretically, the relationship between the wavelength of the primary waves (SDT and 23-day wave) and the secondary wave (11.75 h wave) is given by

$$\lambda_{SS} = \frac{\lambda_{ST}\lambda_{PW}}{\lambda_{ST} + \lambda_{PW}}$$

Equation 6.2

Form Equation 6.2, $\lambda_{ST}, \lambda_{PW}$ and λ_{SS} are wavelengths of semidiurnal tide, planetary wave and secondary wave.

The theoretical wavelength of the 11.75 h wave was found to be 32 km. The percentage difference between the theoretical and computed vertical wavenumber/wavelength of the 11.75 h secondary wave was 31 %. The results of the vertical wavelength/wavenumber for all waves in question are listed in the Table 6.1.

Table 6.1: Vertical wavelengths and wavenumbers of the 23-day planetary wave, SDT and secondary wave computed from zonal wind velocity. Theoretical value of wavelength of the secondary wave is calculated using Equation 6.2.

Waves	Planetary waves	Tide	Secondary waves	Theoretical values
	23-day	SDT	11.75 h	11.75 h
λ (km)	50	89	21	32
k_v (rad/km)	0.124	0.070	0.286	0.159

6.3.2 The 5-, 10- and 16-day wave in the meridional component

Similar analysis to that used in the 23-day wave in the zonal wind was applied to prove the validity of the 5-, 10- and 16-day waves in the meridional wind. Instantaneous amplitude and phase were also used to determine the temporal and vertical variation of these waves as shown in Figure 6.8. Figure 6.8 (a), (c) and (e) show the amplitudes of the 16-, 10- and 5-day waves respectively while Figure 6.8 (b), (d) and (f) show the phases of the 16-, 10 and 5-day waves respectively. The activity of the16-day wave in Figure 6.8 (a) seems to intensify from day 200 to 290 reaching maximum amplitude of about 17 m/s around day 250. The height variation of this wave shows a maximum activity around the 90 km to 95 km region. Comparison with the vertical and the temporal variation of the variance of this wave, which was used as a proxy for wave activity, presented by Day and Mitchell (2010b) show similar results. Considering that for a constant-amplitude oscillation, amplitude is equal to the square root of twice the variance, Day and Mitchell (2010b) found that the 16-day wave had a maximum variance of approximately 100 m^2/s^2, which corresponds to about 14 m/s. The activity of the 10-day waves shown in Figure 6.8 (c) is at maximum near day 200 while the 5-day wave activity is maximum near day 200 and 230. The 10- and 5-day wave activity also reaches maximum amplitudes of about 12 m/s and 17 m/s around 90 km, respectively. Day and Mitchell (2010a) investigated the activity of the 5-day wave and found it to reach maximum amplitude of about 14 m/s during the same time and at the same height. The phase of the 16-day wave in Figure 6.8 (b) seems to increase

with height from 80 to 90 km, specifically during the time when the amplitude is maximum, thereafter the phase decreases with height. The phase of the 10-day wave in Figure 6.8 (d) shows a very small change in phase with height indicating that the 10-day wave is evanescent. The phase of the 5-day wave however, shows a decrease in phase with height.

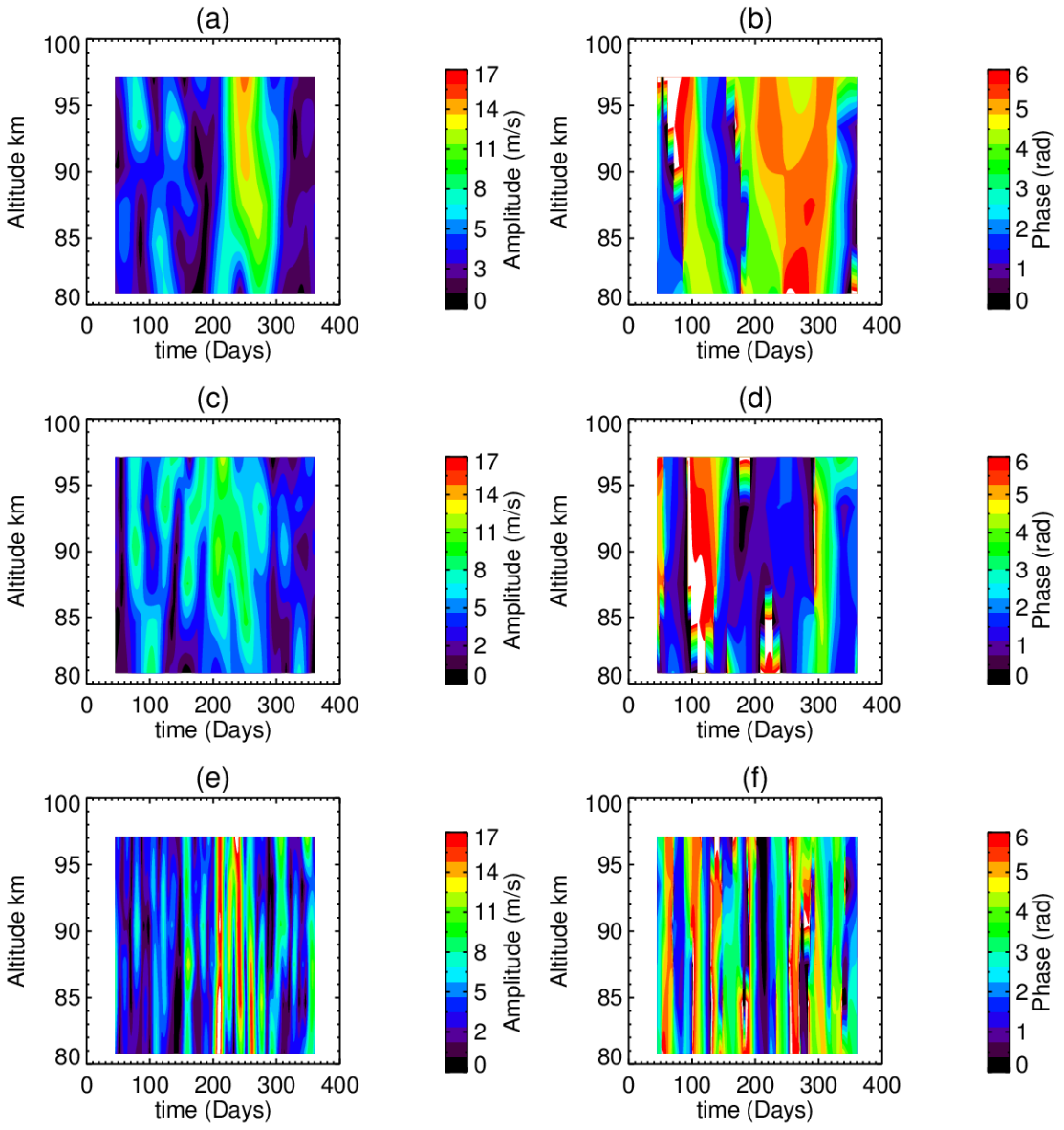

Figure 6.8: Instantaneous amplitude (left panel) and phase (right panel) of the 16-day (top panel), 10-day (middle panel) and 5-day (bottom panel) waves computed as amplitude and phase of the analytical signal at all heights.

Fourier transform was used to extract the amplitude and phase of these waves at different heights and the results are presented in Figure 6.9. The parameters of the 16- and 10-day wave were extracted using the data ranging from day 180 to 270 while that of the 5-day wave was extracted from the data ranging from day 230 to 260. These ranges were chosen close to the

time when the wave amplitudes were at maximum, yet long enough to yield a good frequency resolution. The left panel shows the wave amplitudes correspond to the 5-, 10- and 16-day periodicity. The dotted line indicates the 95% confidence level. The phase profiles on the right panel show an upward phase propagation of the 16-day wave from 80 to 90 km, implying that the wave was propagating downward at this altitude range. However this wave shows downward phase propagation in the 90-97 km altitude range indicating an upward wave propagation. On the other hand, the 5-day wave shows a downward phase propagation, implying an upward wave propagation, while the 10-day wave shows a very small phase change with height, indicating that this wave is evanescent and this made it impossible to compute the vertical wavelength of this component. Thus the validity of the vertical wavenumber relationship on the 10-day wave could not be tested. The 5-day wave investigated by Day and Mitchell (2010a) was found to be evanescent and they proposed refraction as a possible effect that prevented this wave from propagating. The linear least-square fit was used to determine the vertical wavelength/wavenumber of the 16-day wave from the phase gradient and was found to be 99 km/0.063 rad/km above 90 km and 26 km/0.239 rad/km below 90 km. Using the data for 2007, Day and Mitchell (2010a) reported a vertical wavelength of the 16 day wave of about 70 km. This slight difference may be attributed to inter-annual variability of this wave presented in Day and Mitchell (2010a) between the winter of 2005 and 2007. Pancheva and Mitchell (2004) investigated a 15-day wave in the meridional wind in the Northern hemisphere and found a vertical wavelength of ~73 km. The wavelength/wavenumber of the 5-day wave was found to be 72 km/0.087 rad/km.

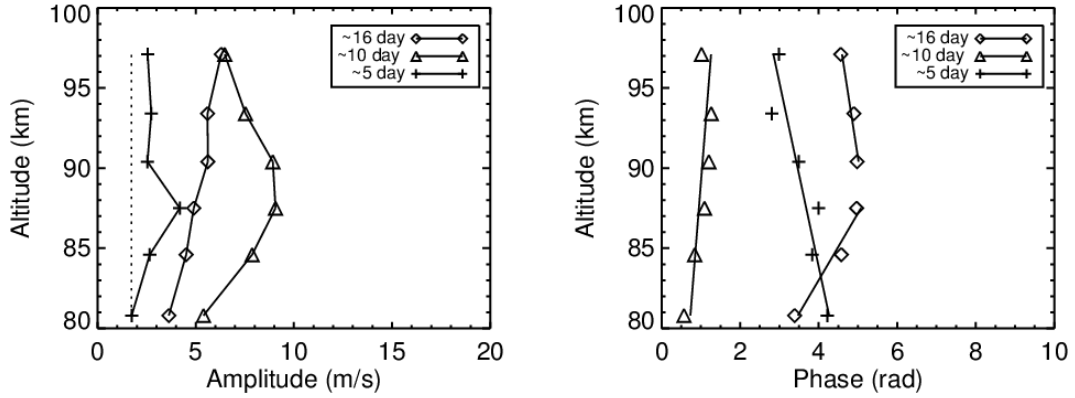

Figure 6.9: Amplitude (left) and phase (right) of the 5-day, 10-day and 16-day waves plotted as a function of height computed for a time interval day 180-270 for a 16- and 10- wave. The 5-day wave parameters were computed for a time interval day 230-260. The dotted line indicates the 95% confidence level.

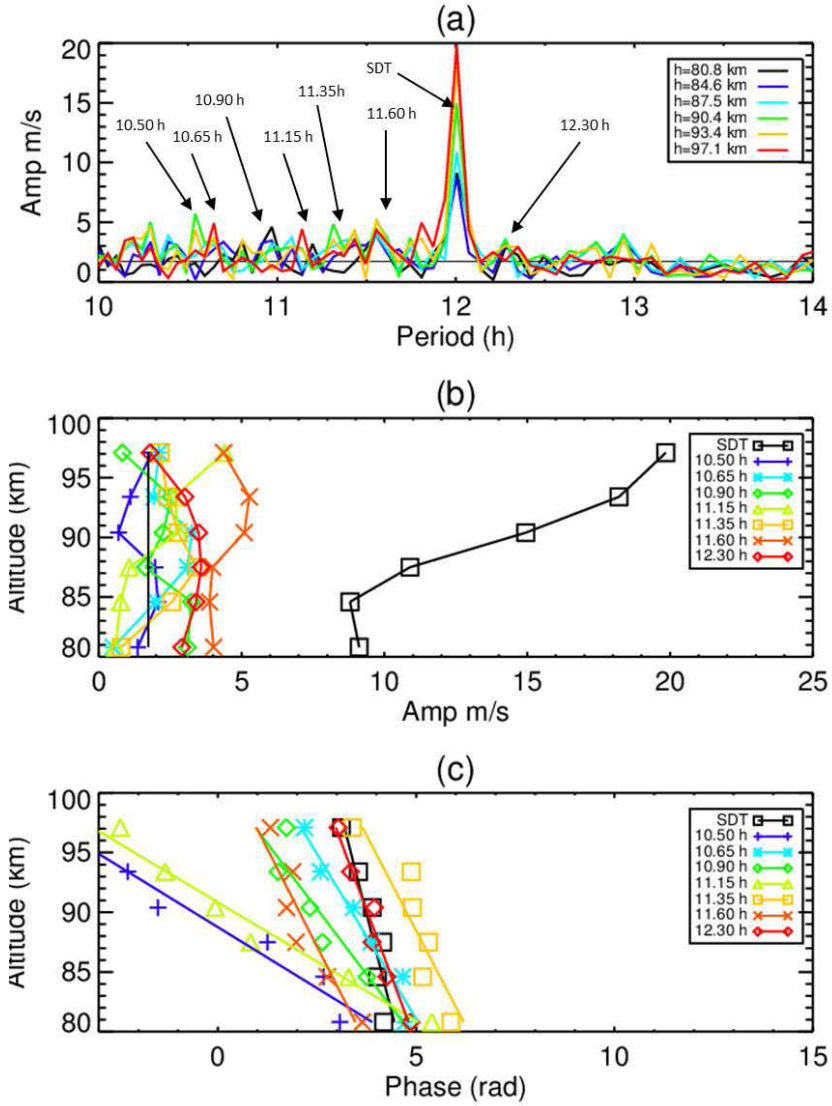

Figure 6.10: (a) Amplitude spectra of the wind velocity time series computed for a time interval day 180-270. (b) The amplitude of the SDT and the sum secondary waves as a function of height. The solid black line indicates the 95% confidence level. (c) The phase of the SDT and the sum secondary waves as a function of height. The solid lines indicate the linear least-squares best fits.

The SDT and the secondary waves were extracted from different heights by computing the Fourier transform of the meridional wind velocity from day 180-270 (where strong modulation was observed) and the spectra are presented in Figure 6.10 (a) for a period range of 10-14 h. The spectra show distinct peaks corresponding to the SDT and secondary waves with a period of approximately 10.5 h, 10.6 h, 10.9 h, 11.1 h, 11.4 h, 11.6 h and 12.3 h shown with arrows. The 10.9 h, 11.4 h and 11.6 h secondary waves are of interest and the focus will be on them as they are the result of the non-linear interaction of the SDT and the 5-day, 10-day and the 16-day waves, respectively. The frequencies of the SDT and the secondary waves are 0.08333, 0.09523, 0.09433, 0.09174, 0.08976 and 0.08620 h-1 respectively and the frequency resolution is

0.0004629 h^{-1} which is adequate for the separation and extraction of the secondary waves. The amplitude of the SDT and secondary waves are extracted from different heights and presented in Figure 6.10 (b) and the phase profiles are shown in Figure 6.10 (c). The phase profiles show a downward phase propagation indicating that the waves are propagating upward and translate into the wavelengths/wavenumbers of 82 km/0.076 rad/km for the SDT, 28 km/0.228 rad/km for the 10.9 h waves, 42 km/0.151 rad/km for the 11.4 h wave and 42 km/0.149 rad/km for the 11.6 h. The wavelength of the SDT and the 11.6 h wave investigated by Pancheva and Mitchell (2004) in the meridional wind were 41 km and 28 km respectively. The wave parameters were extracted for all the waves and summarized in Table 6.2. The theoretical wavelengths of the waves are computed from Equation 6.2 and the results are presented in Table 6.2. The percentage difference between the computed parameter and the theoretical values for 10.9 h and 11.6 h waves are 47% and 4.5% respectively.

Table 6.2: Vertical wave lengths and wavenumbers of the 5-, 10- and 16-day planetary wave, SDT and secondary waves computed from zonal wind velocity. Theoretical values of the wavelength of the secondary waves are calculated using Equation 6.2.

Waves	Planetary waves			Tide	Secondary waves			Theoretical values		
	5-day PW	10-day PW	16-day PW	SDT	10.9 h	11.4 h	11.6 h	10.9 h	11.4 h	11.6 h
λ (km)	72	---	99	82	28	42	42	38	---	44
k_v (rad/km)	0.087	---	0.063	0.076	0.228	0.151	0.149	0.163	---	0.139

6.4 Summary and conclusion

The principal objective of this work was to investigate planetary waves and the variability of the SDT amplitude thereafter seeking a connection between the two. Planetary waves with periods ~ 5, 10, 16 and 23 days are observed in the zonal as well as in the meridional winds and are found to have significant winter amplification. The 23-day wave is found to be an upward propagating wave which dominates in the zonal component while the 16-day wave was found to propagate downward from 80-90 km and upward from 90-97 km and dominates in the meridional wind. The 5- and 10-day waves were also observed to be dominant in the meridional wind. It was noticed that the 5-day wave propagated upward while the 10-day wave was evanescent. The winter-time 23-day wave in the zonal wind had previously been observed (Luo et al., 2001; Pancheva and Mitchell 2004) and was found to be associated with the solar rotation

period. Alternatively, the 5-, 10- and 16-day waves are related to the well-known normal modes (Salby, 1984).

Further analysis has shown that the 23-day wave in the zonal wind and the 5-, 10- and 16-day waves in the meridional wind may be responsible for the SDT variability observed in the MLT region, therefore the analysis was restricted to the above mentioned waves. The activity of the 23-day wave in the zonal wind and 5-, 10- and 16-day waves in the meridional wind were found to be weak at the lower altitude and intensify with increasing height reaching maximum around 90 km. Fourier transform was used to extract the amplitude and phase of these components at different altitudes. The slopes of their phase profiles were determined and from this information, the vertical wavelengths/wavenumbers were computed and found to be 50 km/0.124 rad/km for the 23-day wave in the zonal component. The wavelengths/wavenumbers of the 5-day wave and 16-day wave in the meridional component were found to be 72 km/0.087 rad/km and 99 km/0.063 rad/km, respectively. The 10-day wave was found to be evanescent which then made the computation of the vertical wavelength difficult.

The SDT in the zonal and meridional wind was found to be variable and its amplitude being modulated. Wavelet analysis of the daily values of the SDT amplitude revealed that the SDT was modulated at a period of 23 days in the zonal wind and at 5, 10 and 16 days in the meridional wind. The modulation of the SDT amplitudes in both winds coincides with the planetary wave activity. These results indicate the possibility of non-linear interaction between SDT and 23-day planetary wave in the zonal wind as well as the 5-, 10- and 16-day wave in the meridional wind. To verify that this wave-wave interaction actually took place, the validity of frequency, phase and wave number relationship was investigated.

Bispectral analysis was used to prove the validity of frequency and phase relationship and the result came out positive indicating the interaction between the SDT and the 20-25 day wave in the zonal wind and interaction between SDT and 5 as well as the 10-16 day wave in the meridional wind.

Finally, the vertical wave number relationship was investigated by extracting the secondary waves. The period of planetary wave is very much longer than that of tide, thus the period of the secondary wave is close to that of tide so the secondary waves were extracted simultaneously with the tide. Fourier transform was used to extract the amplitude and the phase of the SDT and the secondary wave with a period of 11.75 h which is due to the interaction of the SDT and the 23-day wave in the zonal wind. In the meridional wind, 10.9 h, 11.4 h and 11.6 h secondary waves formed due to the interaction between the SDT and 5-, 10- as well as 16-day waves

respectively, were extracted from different heights. The wavelengths/wavenumbers of the SDT and the secondary wave in the meridional wind were determined from the slopes of the best fit lines of the phase profile and were found to be 50 km/0.124 rad/km and 22 km/0.286 rad/km respectively. The theoretical wavelength/wavenumber of the 11.75 h wave computed using Equation 6.2 and was found to be 32 km/0.159 rad/km. On the other hand, the wavelengths/wavenumbers of the SDT, 10.9 h, 11.4 h and 11.6 h secondary waves were found to be 82 km/0.076 rad/km, 26 km/0.228, 41 km/0.151 rad/km and 42 km/0.179 rad/km, respectively. The theoretical wavelengths/wavenumbers of the 10.9 h and 11.6 h waves were found to be 38 km/0.163 rad/km and 44 km/0.139 rad/km. Correspondingly, the theoretical wavelengths/wavenumbers of the 11.4 h wave could not be computed because the 10-wave is evanescent with an infinitely long wavelength.

The percentage difference between the theoretical and the computed wavelengths/wavenumbers of the 11.75 h wave in the zonal wind was found to be 31 % and the percentage differences for the 10.9 h and 11.6 h wave in the meridional wind was 47 % and 4.5 %, respectively. Except for the 11.75 h wave in the zonal component and the 10.9 h wave in the meridional component which exhibit a higher percentage difference between the computed and the theoretical values of wavelengths/wavenumbers. The percentage difference between the theoretical and the computed value of wavelengths/wavenumbers for the11.6 h component is comparable (3.7 to 21.9 %) with those obtained by Pancheva and Mitchell (2004). Therefore, based on their conclusion, these results strongly support that the non-linear interaction between the 16 day planetary wave and the SDT in the meridional wind is mostly responsible for the variability of the SDT rather than the interaction between the SDT and the 23-day wave in the zonal wind as well as the interaction of between the SDT and the 5-day wave in the meridional wind. However, a similar data analysis, with a different period of observations, is required to conclude any statement.

7 Coupling between neutral atmosphere and ionosphere through planetary waves

7.1 Introduction

The ionosphere is considered the most complicated region of the earth's atmosphere due to for example, variability of influences emanating from the sun that drive this region, internal interaction taking place within the region and effects emanating from the magnetosphere above as well as from the neutral atmosphere below. These effects can be grouped as solar, magnetospheric and meteorological influences and they all contribute to complicating the physics of the ionospheric region. The present study investigates the meteorological influence on the ionosphere (i.e. the neutral atmosphere-ionosphere coupling) however, solar and magnetospheric influences are also considered.

Ultra violet radiation from the sun is the main cause of ionization in the ionosphere. Variation of the solar flux radiations results in a variation of ionospheric plasma density at periods ranging from days (e.g. 13.5 and 27 day oscillation), months (e.g. semi-annual oscillation) and years (e.g. annual and 11-year oscillation). Moreover, variations in neutral composition, neutral temperature and wind as well as conductivity forced by variations in the solar flux radiations also influence ionospheric plasma density. The variations of solar flux radiations at the 11-year solar cycle was found to substantially contributed to ionospheric variability while annual, semi-annual and 27-day oscillations have lesser effects (Forbes et al., 2000). Previously, Pancheva et al. (1991) found a 27-day oscillation in the ionosphere that was related to variation in solar activity during periods of high solar activity. However, during quiet conditions, the 27-day oscillations observed in winter were found to be of meteorological origin.

The interaction of solar wind with the earth's magnetic field triggers numerous disturbances in the magnetosphere which are termed 'magnetic storms', which in turn cause some modification in the F-region of the ionosphere (Foster et al. 1986). Effects of the magnetic storms on the ionosphere are termed 'ionospheric storms' and a detailed review of the ionospheric storms is given by Prölss (1995). Some of the variations associated with the ionospheric storms are precipitation of energetic particles, changes in the neutral composition and structure as well as an increase in the magnetospheric convection electric field (Foster et al., 1986). A quantitative study on the effect of magnetospheric activity on the ionospheric f_oF2 has been conducted by, among others, Xiong et al. (2006) and their result revealed that 30-50 % of the variability in the ionosphere at 5-, 10- and 13.5-day periods are of geomagnetic origin.

The studies on the ionospheric variability conducted by Forbes et al. (2000) and Rishbeth and Mendillo (2001) reveal that major effects on the ionosphere are triggered by magnetospheric activity. However meteorological influences still contribute substantially. The meteorological influence in the ionosphere is transmitted through upward propagating gravity waves, tides and planetary waves. These waves are excited in the tropospheric and stratospheric regions by various processes including: tropospheric convention (Holton and Alexander 1999), absorption of solar radiations by ozone and water vapor (Zhang et al., 2010) as well as topography and instabilities associated with temperature variations (McHall 1992). As the waves propagate upward, they grow exponentially up to altitudes of ~80-120 km where dissipation becomes important, or where they become convectively unstable and break, thereby depositing their energy and momentum in the region. The deposited energy and momentum may cause turbulence and contribute to heating and acceleration of the mean flow. Nevertheless, numerous studies have reported signatures of ionospheric oscillations at periods corresponding to those of planetary waves (2-30 days) which may be referred to as planetary wave-type oscillations (PWTO). Furthermore, simultaneous occurrences of the oscillations in the neutral atmosphere and ionosphere hinted at the coupling effect between the two regions and this was studied in details by e.g. Pancheva et al. (1994); Pancheva and Lyseko (1988); Apostolov et al. (1995); Pancheva et al. (2002).

In reports on neutral atmosphere-ionosphere coupling, it has been proposed that PWTO in the ionosphere result from direct penetration of planetary waves excited from the lower region of the atmosphere. Brown and John (1978) noted that even a small leakage of the planetary wave energy into the ionosphere has the potential of driving oscillations with large amplitude. Modulation of tides and gravity waves at planetary wave periods is proposed as one of the mechanisms responsible for transmitting planetary wave signatures to the ionosphere (Lastovicka et al., 2003, Pancheva et al., 2002). Recently, some studies have reported neutral atmosphere-ionosphere coupling during sudden stratospheric warming (SSW) using electron density, ion temperature, ion drift, f_oF2 and h_mF2 (Goncharenko and Zhang, 2008; Chau et al., 2009; Goncharenko et al., 2010). These studies were conducted during periods of low magnetic condition which are conducive for studying vertical coupling. Furthermore, this condition allows for the explicit determination of ionospheric effects that originate from the neutral atmosphere.

The mechanism that describes the coupling between the neutral atmosphere and ionosphere is given by the dynamo electric effect outlined in Pancheva and Lysenko (1998). During magnetically quiet conditions, wind systems, dominated by atmospheric waves propagate from

the neutral atmosphere to the ionosphere. In the ionosphere the wind system displaces plasma (an electrically conducting medium) through the earth's magnetic field and generates wave-like ionospheric electric fields and currents. Furthermore, the induced wave-like electric current system creates perturbations in the magnetic field that can be detected by ground-based magnetometers. The neutral atmosphere-ionosphere coupling is believed to be driven by a global-scale wave with large amplitude propagating from the neutral atmosphere into the ionosphere. Observational evidence of the neutral atmosphere-ionosphere coupling through planetary waves was previously given by researchers such as Pancheva et al. (2002, 2006); Mukhtarov et al. (2010)

The aim of this study is to investigate the coupling effect between the neutral atmospheres and ionosphere through upward propagating planetary waves. As it is well known that the ionosphere is also greatly influenced by factors coming from above, possible magnetospheric as well as solar effects on the ionosphere are investigated. This study is conducted using the 2002 data prior to the SSW event that is presented in Chapter 6. Therefore some of the discussions on the planetary wave activity are drawn from this chapter.

7.2 Data set and method of analysis

Neutral atmospheric activity was investigated using wind velocity data from the SANAE HF radar, whose location is shown in Figure 7.1, while the variability of ionospheric currents detected by a ground-based magnetometer situated at SANAE was used to represent ionospheric activity. The Dst-index was used to characterize geomagnetic influence while the flux of the solar radio emission at 10.7 cm wavelength (F10.7) was used as a proxy for solar activity. For better comparison daily averages of all datasets were computed and used for further analysis. Also presented in Figure 7.1 is the variation of the 2002 Dst-index from day 150 to 300. On average the figure shows quiet geomagnetic condition (Dst $\geq$ -50) with brief episodes of a minor storm near days 250 and 280 (Gonzalez et al., 1994). Altadill et al. (2003) also considered these conditions as quiet during their study, which reported simultaneous oscillations of quasi-6-day wave in the neutral winds and the ionospheric plasma frequency at 240 km (fp240). Therefore this time interval can be considered as geomagnetically quiet and consequently the conditions were conducive for studying coupling effect between atmospheric regions (Goncharenko and Zhang, 2008; Chau et al., 2009; Goncharenko et al., 2010a; Pancheva and Mukhtarov, 2011)

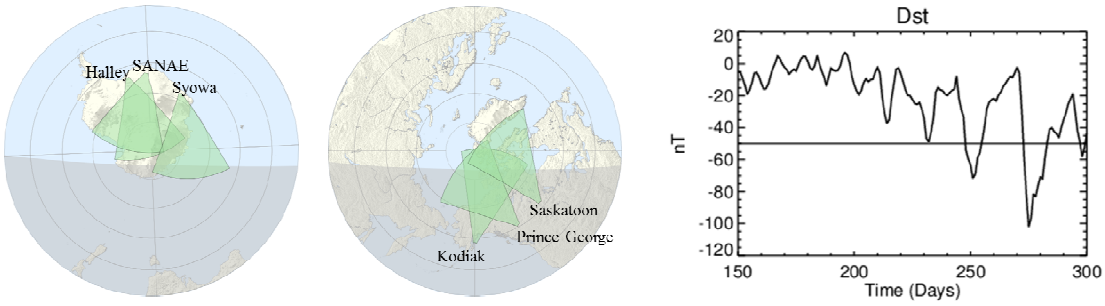

Figure 7.1: Locations of the HF radars from southern (left) and Northern hemisphere (middle). The right panel shows the variation of the 2002 Dst-index from day 150 to 300.

The wavelet transform which uses the Morlert wavelet was used to determine dominant spectral components and time of occurrence in the time series. The Morlet wavelet is suitable for this kind of investigation because it resembles modulated planetary-wave like oscillations that are frequently observed in the neutral atmosphere and the ionosphere. Cross-wavelet transform was then used to quantify the magnitude of the spectral components that coexist in the two time series. The time evolution of amplitude and phase of the selected spectral component was investigated using the analytical signal. These techniques are explained in details in Chapter 2.

Coupling between ionosphere and the neutral atmosphere through upward propagating planetary wave takes place provided there is a global-scale planetary wave observed in the neutral atmosphere (Pancheva et al., 2002). Thus, the global-scale wave nature of planetary wave was investigated using neutral wind velocity measured from the Southern hemisphere SuperDARN HF radars from Halley (75°S, 27°W), SANAE (72°S, 3°W) and Syowa (69°S, 40°E) as well as those from the Northern hemisphere at Kodiak (58°N, 152°W), Prince George (54°N, 123°W) and Saskatoon (52°N, 107°W) as shown in Figure 7.1. These radars are within a 6° latitudinal band suitable for the computation of the zonal wavenumber of planetary waves.

7.3 Results

Figure 7.2 presents normalized wavelet spectra of wind velocity, magnetic field, F10.7 and Dst-index with the white contour representing a 95% confidence level. This figure shows numerous planetary wave (PW) oscillations that simultaneously exist in the neutral winds and the ionosphere. These include quasi-20-day wave activity around day 120 in the zonal component of winds and in the X-component of the magnetic field, a quasi-16-day wave activity in the zonal and meridional winds around day 200 to 250 with similar oscillations in the X- and Y-component of the magnetic field. The oscillations in the magnetic field have a rather broad

period range extending from ~10 to 25 days. Coexistence of these PW oscillations indicates a possible neutral atmosphere-ionosphere coupling. In addition, Dst-index and F10.7 show quasi-23-day periodicity also around day 200 to 250. This may indicate a possible magnetosphere-ionosphere or solar-ionosphere coupling. The quasi-23-day wave is possible associated with the 27-day solar rotation (Luo et al., 2001; Pancheva and Mitchell 2004) while the quasi-10- and the quasi-16-day waves are related to the well-known 10- and 16-day normal modes (Salby, 1984).

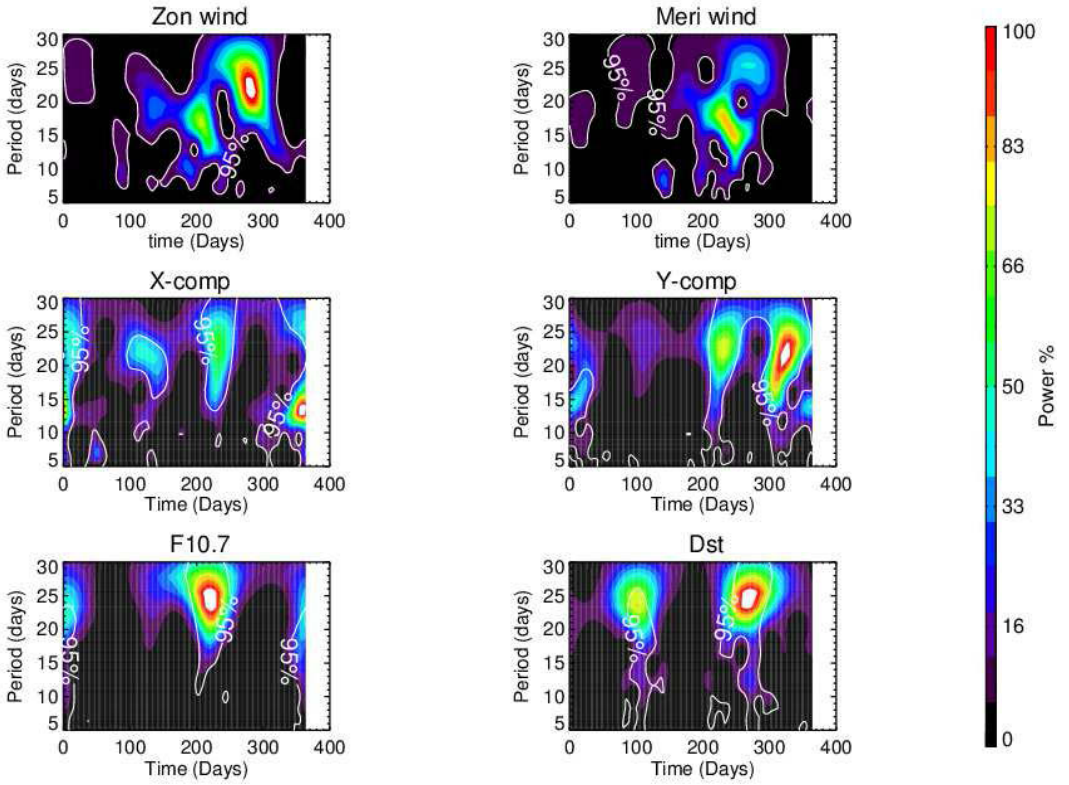

Figure 7.2: Normalized wavelet spectra of wind velocity from SANAE HF radar, magnetic field data from magnetometer at SANAE, Dst index and F10.7. White contour represents the 95% confidence level.

To quantify the above mentioned coupling, cross wavelet spectra between respective time series were computed and presented in Figure 7.3. This technique quantifies spectral components that simultaneously exist in the two time series. This figure shows simultaneous existence of the quasi-16-day periodicity between the neutral atmospheric winds and the magnetic field near day 200 to 250 indicated as peak number 1 in Figure 7.3 as well as near day 320 indicated as peak number 4. These peaks indicate a possible neutral atmospheric influence on the ionosphere that is not related to solar nor magnetospheric influence. The 23-day periodicity near day 200 to 300 shown as peak number 2 indicates a possible neutral atmospheric, solar and magnetospheric influence on the ionosphere. Neutral atmospheric and magnetospheric influence on ionosphere

at quasi-20-day periodicity is also indicated as peak number 3. Based on Figure 7.3, quasi-16-, -20- and -23-day waves will be extracted and further analysed in Subsections 7.3.1 to 7.3.3.

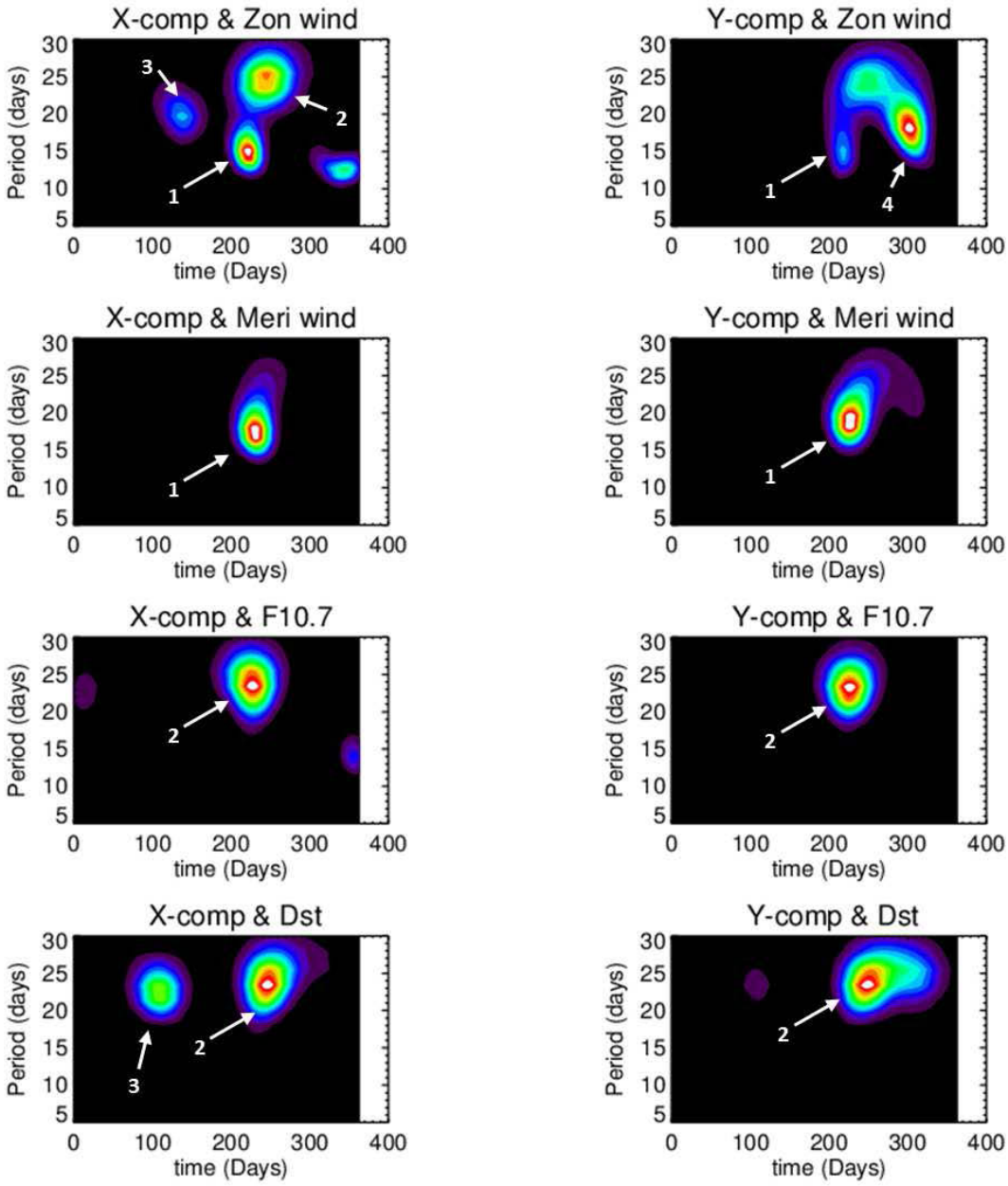

Figure 7.3: Cross wavelet spectra between the X-component of magnetic field (left) and zonal winds, meridional winds, F10.7, Dst-index. The right panel is the same as the left panel but for the Y-component of the magnetic field.

7.3.1 Quasi-16-day wave

The quasi-16-day wave from the zonal winds as well as in the X- and Y-component of the magnetic field was extracted from day 150 to 300 using a band pass filter with a band width extending from day 13 to 19 and the results are presented in the top panel of Figure 7.4. A band

pass filter with band width of 14-19 days was used to extract the quasi-16-day wave from the meridional component and both components of the magnetic field as shown in the bottom panel of Figure 7.4. This figure shows that the quasi-16-day wave was first observed in the neutral atmosphere and later in the ionosphere. The travelling time of the quasi-16-day wave between these two regions was computed using the analytic signal. This method is used to determine instantaneous amplitude and phase of the selected quasi monochromatic spectral component. The average of the instantaneous phase was computed from day 200 to 250 where the quasi-16-day wave activity was at maximum. The phase difference of the waves from two regions gives the time of travel of the wave. The time of travel computed between the zonal winds and X- as well as the Y-component of the magnetic field is given by 3.7 and 3.1 days, respectively. On the other hand the travel time between the meridional winds and X- as well as the Y-components of the magnetic field is given by 5.8 and 6.1 days, respectively. The study on coupling effect between the neutral atmosphere and the ionosphere through PW conducted by Pancheva et al. (2002) using the neutral winds and the h_mF2 recorded above Millstone Hill (42.6°N, 71.5°W) reported a travel time of 5-6 days. Later, Borries et al. (2007) conducted a similar study using stratospheric geopotential height and ionospheric total electron content (TEC). They reported a time delay of about 3 days between the two regions. The time delay reported in the present study falls within the range of the time delay reported in the literature. Therefore these results further support the proposition that the quasi-16-day periodicity observed in the ionosphere is possibly due to the upward propagating wave observed in the neutral atmosphere.

The time delay of the quasi-16-day periodicity observed near day 320 (indicated as peak 4 in Figure 7.3) was also computed but the results are not shown. It was discovered that quasi-16-day periodicity in the ionosphere was about 6 days ahead of that in the neutral atmosphere. This implies that, during this time, other influence from unknown sources, and not PW from below, were responsible for the ionosphere variability. Figure 7.3 shows that the variation in the ionosphere at quasi-20-day periodicity may have originated from the neutral atmosphere as well as from the magnetospheric activity. The possible source of this periodicity in the ionosphere is investigated in the next section.

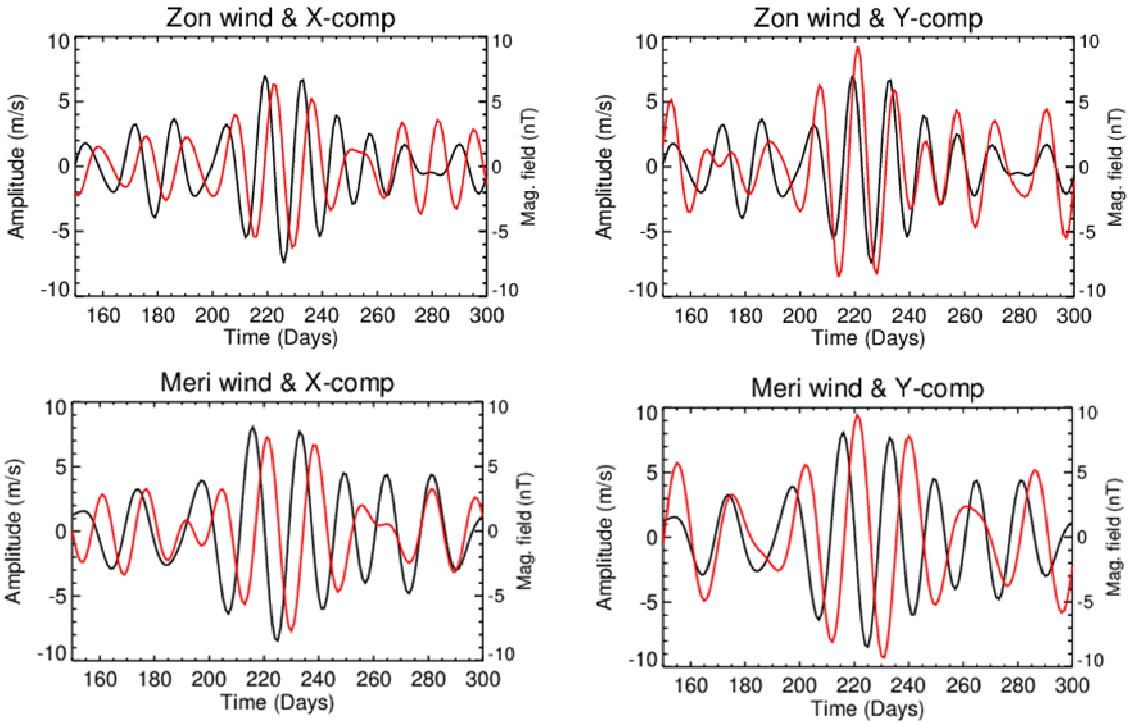

Figure 7.4: Top panel shows a quasi-16-day wave isolated by band pass filtering the zonal component of winds (black) as well as X- (left, red) and Y-component (right, red) of magnetic field from 13 to 19 days. The bottom panel is the same as the top panel but for meridional winds using a filter with a bandwidth of 14-19 days.

7.3.2 Quasi-20-day wave

The quasi-20-day wave was extracted in the time range day 1 to 200 (where the activity of the wave was maximum) from the zonal winds, X-component of magnetic field and Dst-index by band pass filtering the data from using a band width of 14-26 days as shown in Figure 7.5. This figure indicates that PW oscillation enhances from day 50 to 150 in all parameters. Furthermore, the quasi-20-day oscillation in the ionosphere is approximately 5 days ahead of that in the neutral atmosphere. Therefore, this eliminates upward propagating PW from the neutral atmosphere as the source of the ionospheric variability at this period. Alternatively, the quasi-20-day oscillation in the Dst-index was found to be 0.68 day (~16 h) ahead of the oscillation in the ionosphere. From this result it can be deduced that if the magnetospheric activity was responsible for the quasi-20-day oscillation observed in the ionosphere, the effect was felt ~16 h later. The ionospheric response to magnetospheric activity previously reported by Pröss (1995); Pancheva et al. (2002) was around 0.8 to 1 day. Furthermore, theoretical result by Kutiev and Mukhtaron (2001) in the midlatitude ionosphere reported that the response of the ionosphere to magnetospheric activity was delayed by 0.75 day, which is in accordance with the present results.

As shown in Figure 7.3, the quasi-23-day periodicity (shown as peak 3) was simultaneously observed in neutral wind, magnetic field, Dst-index and F10.7, hence a possible driver of the periodicity in the ionosphere was investigated in the next section.

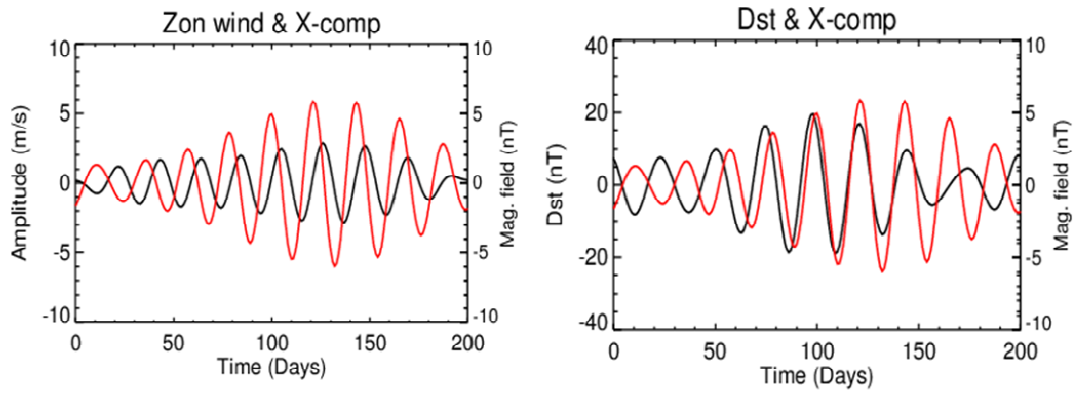

Figure 7.5: A quasi-20-day wave isolated by band pass filtering the X-component of magnetic field (red), zonal winds (left, black) and Dst-index (right, black) from 14 to 26 days.

7.3.3 Quasi-23-day wave

The quasi-23-day oscillation was extracted in the same way as the quasi-16- and quasi-20-day oscillations but using the band width of 19-27 days as shown in Figure 7.6. This figure shows that the magnitude of the quasi-23-day oscillation in the Y-component is twice that in the X-component. Moreover the top panel of Figure 7.6 and computation of phase difference shows that the quasi-23-day oscillation in the X-component of the magnetic field was about 9 days ahead of the oscillation in the zonal winds while the Y-component was about 6 days ahead. This would then eliminate neutral atmospheric activity as a possible source of the observed ionospheric oscillation. The bottom panel shows the quasi-23-day oscillation in the X-component of the magnetic field was 9 days after the oscillation in the solar activity while the Y-component was observed 12 days after. This time delay is much longer than 1 h reported by Walter et al. (1989). This further eliminates solar activity as a possible source of the observed ionospheric oscillation. The middle panel shows that the quasi-23-day oscillation in the X-component of the magnetic field was observed 1.7 days before the oscillation in the Dst-index while the Y-component of the magnetic field was observed 0.7 days after. As noted above the amplitude of the quasi-23-day oscillation in the X-component is small, the corresponding phase is dubious and thus the computed time delay cannot be trusted. Therefore, the time delay of 0.7 day between the oscillations in the Dst-index and the Y-component of the magnetic field is in accordance with that reported by Prӧss (1995); Pancheva et al. (2002); Kutiev and Mukhtaron (2001).

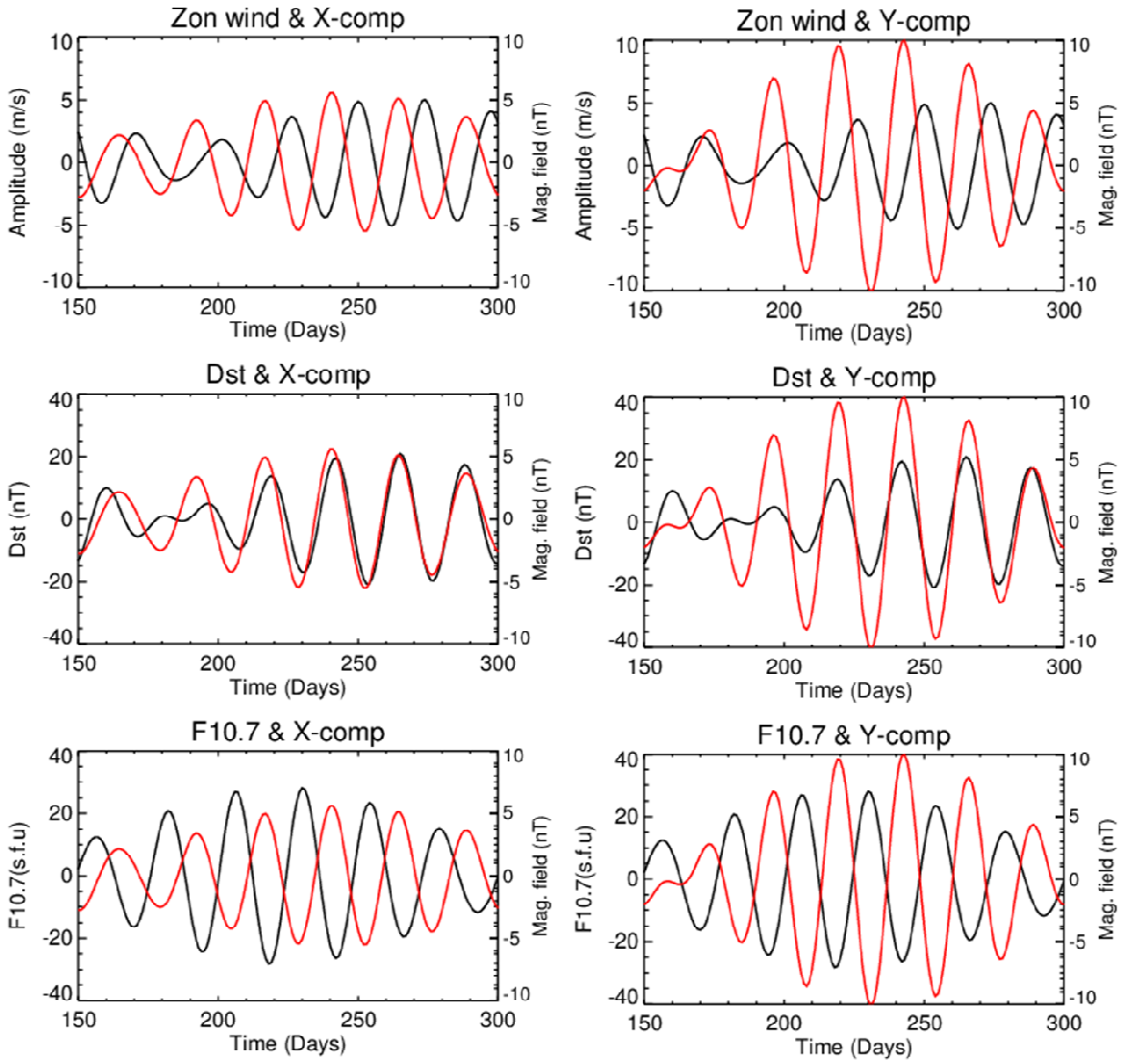

Figure 7.6: A quasi 23-day wave isolated by band pass filtering X-component (left, red) and the Y-component (right, red) of magnetic field from 19 to 27 days. The black curve represent the same wave from the zonal winds, (top), Dst-index (middle) and F10.7 (bottom).

From Section 7.3.1 the quasi-16-day oscillation observed in the ionosphere was discovered to have possibly been driven by the same oscillation observed in the neutral atmosphere. However, this kind of coupling is only possible if the oscillation observed in the neutral atmosphere is a global event. Therefore, the global-scale nature of the quasi-16-day oscillation was subsequently investigated.

7.3.4 Global-scale wave nature of the quasi-16-day wave

Daily averages of the meridional winds from the SuperDARN HF radars located in the Southern hemisphere at Halley, SANAE and Syowa as well as in the Northern hemisphere at Kodia, Prince George and Saskatoon were used. Normalized wavelet spectra of the respective data

were computed and presented in Figure 7.7 with contours of a 95% confidence level superimposed on the figure. This figure clearly shows quasi-16-day-wave activity in the Southern hemisphere extending from around day 180 to 280. The quasi-16 day periodicity is also apparent in the Northern hemisphere from around day 240 to 280.

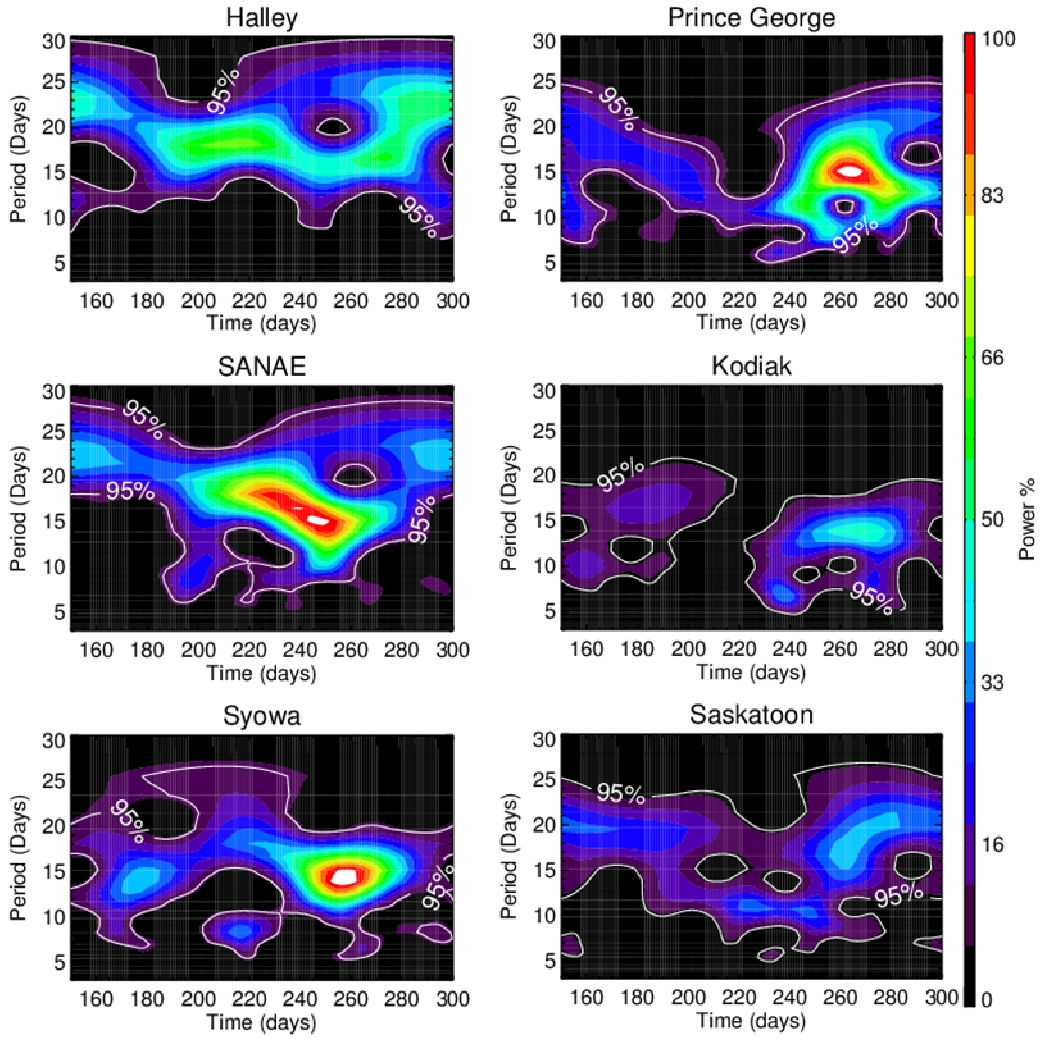

Figure 7.7: Normalized wavelet spectra of HF radar winds from the southern (right) and northern (left) hemisphere. White contours represent a 95% confidence level.

The zonal structure of this wave in both hemispheres was characterized by computing the zonal wavenumber using the method utilized by Mthembu et al. (2013). The amplitude and phase of the quasi-16-day wave were computed using Fourier transform of meridional winds for a time range of day 150 to 300 and the results are presented in Figure 7.8 indicated as black diamonds. This figure shows that the amplitudes are above the 95% confidence level, except at Saskatoon where the amplitude is on a 95% confidence level, and thus the phase can be trusted. The solid line in the bottom panel of Figure 7.8 represents the best-fit line computed using ordinary least-squares fit. The zonal wavenumber was then computed as a gradient of the phase as a function

of longitude. The zonal wavenumber of the quasi-16-day wave in the Southern (Northern) hemisphere computed with the phase from the Fourier transform was found to be -0.6 (-1.4). Instantaneous amplitude and phase of the quasi-16-day wave were also computed using the analytic signal as amplitude and phase of the analytic signal and the results are presented in Figure 7.9 for the Southern hemisphere and in Figure 7.10 for the northern hemisphere. The average phase of the quasi-16-day wave was computed where the activity of the wave was maximum (as indicated by the grey shade) and the results are presented as red triangle in the bottom panel of Figure 7.8. The zonal wavenumber of this wave in the Southern (Northern) hemisphere computed with the phase from the analytic signal was found to be -0.7 (-1.2). The negative sign indicates westward propagation. The westward propagating quasi-16-day waves with wavenumber 1 in the Southern and Northern hemisphere (75°) were also reported by researches such as Dowdy et al (2004); Mbatha et al. (2010); Day et al. (2010b).

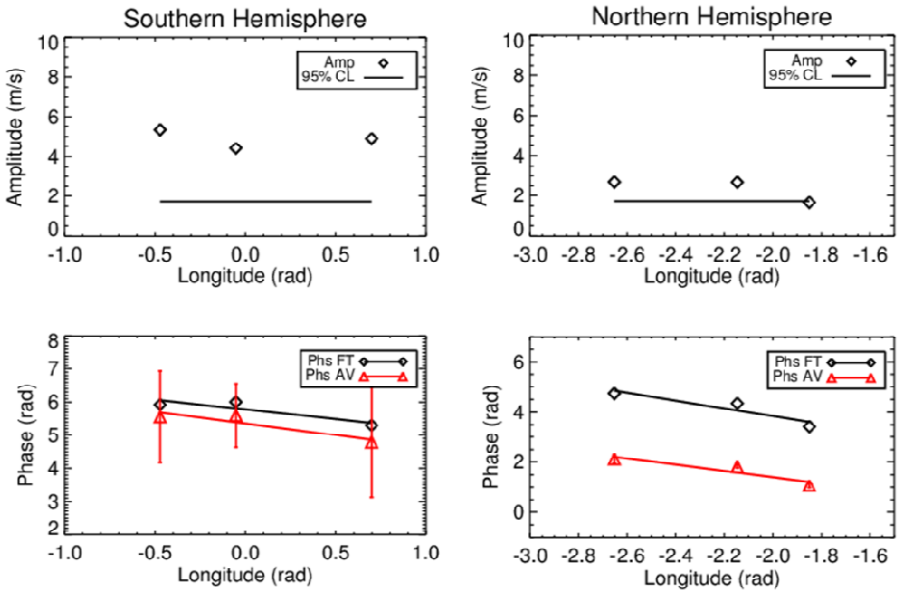

Figure 7.8: Amplitude (top) and phase (bottom) of the quasi 16-day wave from the southern (left) and northern (right) hemisphere. The horizontal line in the top panel represents the 95% confidence level. The phase represented by black diamonds is computed from Fourier transform while the phase represented by red triangle is computed as average of instantaneous phase where the quasi 16-day wave activity as maximum (see Figure 7.9 and 7.10).

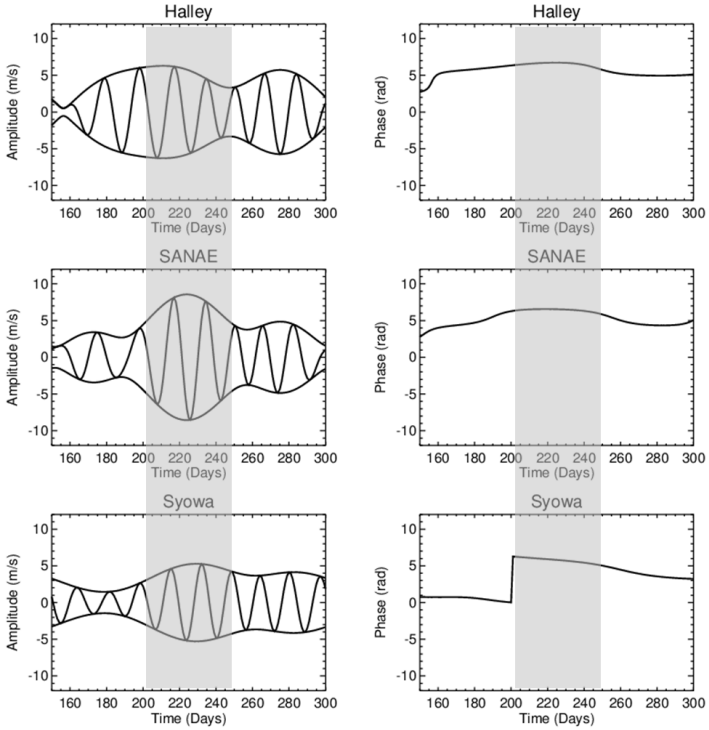

Figure 7.9: The instantaneous amplitude (left) and phase (phase) of the quasi 16-day wave from the meridional component in the southern hemisphere. Grey shade indicates time of simultaneous maximum activity from all stations.

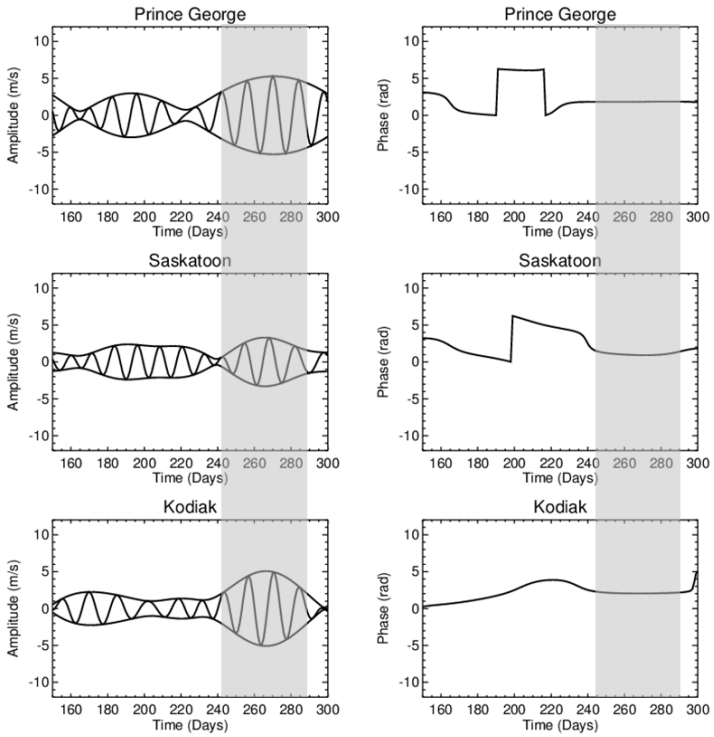

Figure 7.10: Same as in Figure 7.9, but for the Northern hemisphere stations.

7.4 Discussion and summary

The neutral atmosphere-ionosphere coupling was studied using mesospheric winds recoded by SuperDARN HF radar and the magnetic field data recoded by the magnetometer co-located at SANAE. This study was conducted during periods of low geomagnetic activity which is conducive for studying coupling effects between atmospheric regions. Cross-wavelet spectra of the neutral atmospheric winds and magnetic field data displayed, among others, simultaneous occurrence of the quasi-16 day oscillation in the neutral atmosphere and the ionosphere. Further analysis revealed that the phase difference of this oscillation between these regions was 3-6 days. This implied that if the oscillation in the neutral atmosphere was responsible for the oscillations in the ionosphere, it took 3-6 day for the effect to be registered in the ionosphere. Independent studies on neutral atmosphere and ionosphere coupling conducted by Pancheva et al. (2002) and Borries et al. (2007) reported phase difference of 5-6 days and ~3 day, respectively. The phase differences obtained in the present results are within those reported in the literature and this suggests a possible neutral atmosphere-ionosphere coupling through quasi-16-day wave. This proposition was further strengthened through observation of the global-scale wave nature of the quasi-16-day wave.

The mechanism that could explain the observed coupling is the ionosphere wind dynamo electric effect caused by the penetration of the quasi-16-day oscillation as outlined by Pancheva and Lysenko (1998). The penetration of the quasi-16-day oscillation induced electric fields and currents which then caused perturbation in the magnetic field at a period of quasi-16 days. The magnetic field perturbations were recorded by the ground-based magnetometer located at SANAE. According to the numerical model created by Chen (1992), planetary oscillations of magnitude of few tens of m/s are required to drive electrodynamic coupling. According to this model the amplitude of ~7 m/s, found in this study, are not large enough to drive this coupling. However, the results suggest that the ionospheric 16-day oscillation observed in the magnetic field is possibly due to the penetration of quasi-16-day oscillation propagated from the neutral atmosphere. The amplitude of the 27-day oscillation reported by Pancheva et al. (2002) in their study of the neutral atmosphere-ionosphere coupling was 8 m/s. Studies conducted by Lastovicka et al. (2003) showed that planetary waves generated from the lower regions of the atmosphere are unable to penetrate through to ionospheric F-2 region due to filtering processes. Earlier, theoretical studies on planetary waves conducted by Forbes et al. (1995) revealed that direct penetration of planetary waves was not favored. Moreover, independent studies by Pancheva (1998) and Apostolov et al. (1995) revealed that the zonal wavenumbers of the

QTDW observed in the MLT region (i.e. s = 3 and 4) did not match those obtained in the ionosphere (s = 1 or zonally symmetric oscillation). Pancheva et al. (2002) proposed that semidiurnal tides modulated at planetary wave periods, due to their ability to penetrate to the ionosphere, can transfer PWTO to this region. Pancheva et al. (2002) further suggested that if PWTO observed in the ionosphere are due to modulated semidiurnal tides, the semidiurnal tide periodicity in the ionosphere has to be affected. For this investigation normalized Fourier spectra of the raw data of the X- and Y-component of the magnetic field was computed and presented in the top panel of Figure 7.11.

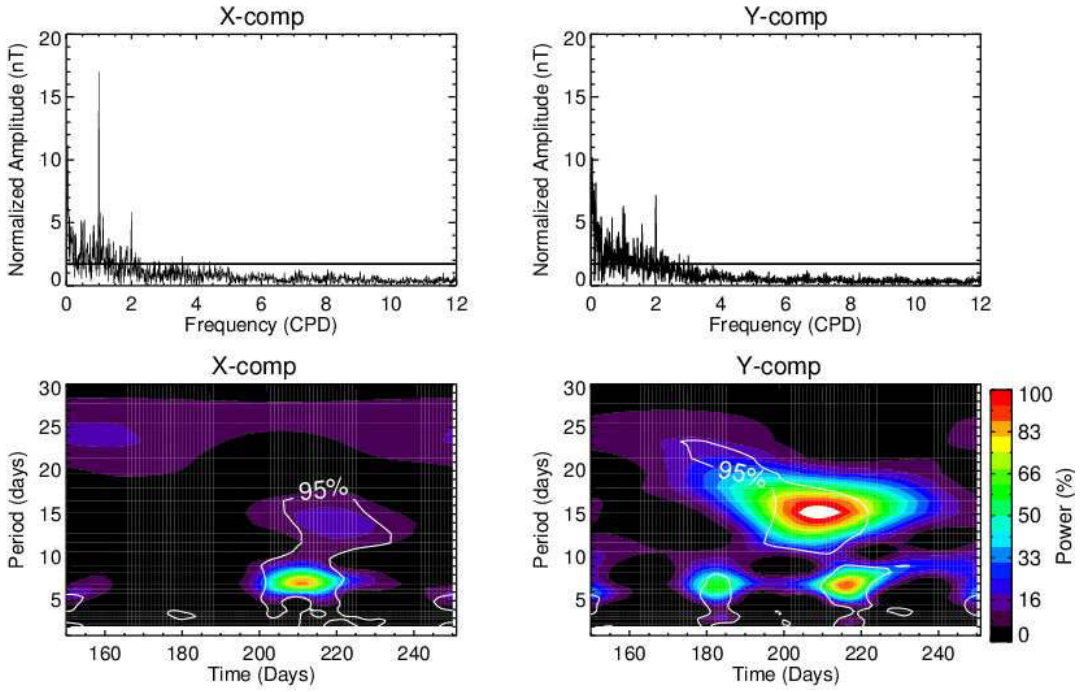

Figure 7.11: Normalized amplitude spectra (top panel) of the X- and Y-components of the magnetic field with the horizontal line indicating 95% confidence level. The bottom panel shows normalized wavelet spectra of the SDT amplitude extracted from the X- and Y-components of the magnetic field.

It is known that the raw data of the magnetic field is dominated by quiet-day geomagnetic perturbation with frequency of 1 cycle per day (CPD), however this figure shows significant peaks above 95% confidence level corresponding to SDT (2 CPD). Thus dynamic Fourier spectrum using a 10-day data window which was progressively shifted forward by one day was used to extract amplitude and phase of the SDT and DT. The computed spectra was attributed to a central day i.e. day 5. Normalized wavelet spectra of the amplitudes and the phases of the SDT and DT from the X- and Y-components of the magnetic field were computed. The bottom panel of Figure 7.11 presents (from day 150 to 250 close to a period where coupling was observed) normalized wavelet spectra of the amplitudes of the SDT showing a quasi-16 day periodicity.

Spectra of the DT amplitude and phase as well as spectra of the SDT phase did not show this quasi-16-day periodicity and thus were not presented. From these results it can be asserted that the 16-day oscillation observed in the ionosphere is most probably due to the penetration of the SDT modulated at a 16-day periodicity.

The mechanism behind the SSW was outlined by Matsuno (1971) and it involves nonlinear interaction between upward propagating transient planetary waves and zonal mean flow. This results in the deceleration and/or reversal of stratospheric and mesospheric eastward winter winds as well as downward circulation in the stratosphere which causes adiabatic heating and upward circulation in the mesosphere which causes adiabatic cooling (Lui and Roble, 2002). The wavelet spectra of the neutral winds presented in Figure 7.2 shows that for the time interval day 180-250 leading to the SSW event, the neutral atmosphere was dominated by quasi-10- and quasi-16-day oscillations, which are believed to have driven the SSW. If further results revealed that only the quasi-16-day oscillations was responsible the coupling of the neutral atmosphere and ionosphere, why was the quasi-10-day oscillation not involved in such coupling? An explanation for this could be drawn from the discussion on the planetary waves during the SSW presented in Chapter 6. The results displayed occurrence of nonlinear interaction between 10-day planetary wave and semidiurnal tide while the results of nonlinear interaction between 16-day planetary wave and semidiurnal tide were negative. Accompanying the nonlinear interaction was a decrease in the 10-day wave energy during the formation of the secondary waves. As a result the 10-day oscillation probably became weak and was filtered out during its upward propagation or if it managed to reach the ionosphere, its energy was insufficient to generate ionospheric oscillations. This may imply that the SDT modulation at 16-day period observed near day 200 in Figure 5.7 was caused by a mechanism other than nonlinear interaction with the 16-day planetary wave. A possible mechanism that may have resulted in the SDT modulation is probably a periodic filtering of the SDT at period of quasi-16 days (Riggin at al., 2003).

It is known that the physics of the ionosphere is not only complicated by meteorological activity, thus solar and magnetospheric influences were investigated as well. The results showed that the phase difference between the 20-day oscillations observed in the ionospheric and magnetospheric parameters was 0.68 days. A possible ionosphere-magnetosphere as well as ionosphere-solar coupling was also observed at quasi 23-day periodicity. The phase difference between solar and ionospheric oscillations at quasi 23-day periodicity was found to be 9-12 days. On the other hand, the phase difference between magnetospheric and ionospheric oscillations was found to be 0.73 days. Observational (Pröss, 1995; Pancheva et al., 2002) and theoretical (Kutiev and Mukhtaron, 2001) results reported a phase difference of 0.8-1 days for

ionosphere-magnetosphere coupling. The phase difference for the solar-ionosphere coupling reported by Walter et al. (1989) was about 1 h. Thus from the results, 9-12 days is rather too long for solar effects to reach the ionosphere. Instead, ionosphere-magnetosphere coupling was preferred.

8 Summary and conclusion

In this thesis, observational study of atmospheric dynamics caused by upward propagating planetary waves and tides was presented. Coupling between the neutral atmosphere and the ionosphere was also investigated. A brief introduction and background theory introduced the topic, which included the description of neutral and ionized atmosphere, brief overview of atmospheric waves (planetary waves and tides) including their theoretical aspects and finally the neutral atmosphere/ionosphere coupling effect was discussed. This is explained by ionospheric electrodynamo mechanism caused by penetration of atmospheric waves through to the ionosphere. Description of data analysis techniques used to analyse the data was given and these include Fourier transform, Wavelet transform, Bispectrum, analytic signal. This was followed by a description of instrumentation used to collect the data which include SuperDARN HF radars, meteor radar and ground-based magnetometer.

The presentation of results began with climatological study of tides observed at Halley, SANAE and Syowa as presented in Chapter 4. In this chapter, the variability of tidal amplitudes at timescales ranging from 1 year to 11 years was investigated using wind velocity data recorded from 1998 to 2007. In particular, seasonal, quasi-biennial, ~5-year and 11-year solar cycle periodicities were investigated. The results indicated that the seasonal variation of the diurnal tides was characterized by maximum amplitudes in summer and minimum amplitudes in winter. The semidiurnal tides exhibited a similar variation but with an additional enhancement of amplitude in the fall. The seasonal behavior of the diurnal tide (semidiurnal tide) was found to be similar to that of tropospheric specific humidity (stratospheric ozone mixing ratio) and thus the forcing mechanism was subsequently considered as a possible source of tidal variation. Investigation of long-term variation of semidiurnal tide showed that it exhibited quasi-biennial oscillation, ~5, and 11 year periodicities. Further analysis revealed significant positive as well as negative correlations between the SDT amplitude and the F10.7 solar flux, which suggests solar activity as a possible driver of the semidiurnal tide variation. Lastly, trend analysis revealed that the tidal variation had a break point coinciding with solar maximum and the trends had opposite signs on either side of a break point.

The 2002 wind velocity data from the SuperDARN HF radars located at Halley, SANAE and Syowa for a time range day 160-310 was used to investigate the variability of semidiurnal tides prior, during and post the 2002 sudden stratospheric warming event. Subsequent to observation of planetary wave activity near day 200-220 (16-day period) and near day 260 (16 and 10-day period), an investigation was conducted using two time segments i.e. day 160-250 and day 250-

310. Forcing mechanism using ozone mixing ratio and nonlinear interaction between planetary waves and the SDT were investigated as possible sources of the SDT variability in both time segments. The results showed that while the variation of ozone mixing ratio probably caused the variation of the SDT before the warming (160-250), nonlinear interaction between the SDT and 10-day planetary wave was possibly responsible for the SDT variation just before, during and after the SSW event (250-310). Further results showed enhancement of the amplitude of the 12.6 h wave (secondary wave) which was accompanied by decrease in amplitudes of the migrating semidiurnal and the 10-day wave (primary waves). The decrease in the primary wave amplitudes is in accordance with the loss of energy during the formation of the secondary waves.

A case study on the investigation of in-situ non-linear interaction between semidiurnal tides and planetary waves and the connection between the variability of the tidal wave observed in the MLT region and this process was undertaken using the 2005 wind velocity data recoded by the MF radar located at Rothera. The results showed that the winds were dominated by semidiurnal tides and planetary waves with periods around 5, 10, 16 and 23 days. Further investigation showed that the semidiurnal tide is substantially variable and modulated at period of ~23 days in the zonal component and at ~5 and 16 days in meridional component. However, non-linear interaction between the SDT and 16-day planetary wave in the meridional component was established as more responsible for the variability of the SDT than the interaction between the SDT and 5 day in the meridional component and between the SDT and 23-day planetary wave in the zonal component.

The final part of this thesis involved an investigation of the coupling effect between the neutral atmosphere and the ionosphere through penetration of upward propagating planetary oscillations. This coupling was examined based on time of travel of planetary oscillations between the two regions. This study was undertaken using SuperDARN HF radar data and magnetic field data both collected at SANAE. Simultaneous oscillation at around 16-day periodicity was observed in the neutral winds and the magnetic field. Further analysis showed that this oscillation most probably emanated from the neutral atmosphere and caused variability in the ionosphere. The ionospheric dynamo effect caused by the penetration of semidiurnal tides modulated at 16-day periodicity was proposed as a mechanism behind this coupling. Since the ionosphere is also known to be affected by magnetospheric and solar activity, such couplings were investigated as well using Dst index and F10.7 representing magnetospheric and solar activity, respectively. While no solar/ionosphere coupling was found, the results indicated that magnetosphere/ionosphere coupling manifested at around 20- and 23-day periodicity.

Future work…

This study on long-term variation of the tides in the thesis was conducted using 10 years' worth of data. Though similar studies were conducted using data of the approximately the same temporal extent, previous results had showed that longer data sets (approximate 40 year's) produce most reliable results. Therefore this study may need to be revisited in the future.

9 References

Andrews, D.G., J.R. Holton and C.B. Leovy. " *Middle atmosphere dynamics*." London: Academic Press. 1987.

Altadill, D., E.M. Apostolov, Ch. Jacobi and N. J. Mitchell. "Six-day westward propagating wave in the maximum electron density of the ionosphere." *Ann. Geophys.* 21 (2003): 1577-1588.

Angelats-i-Coll, M. and J.M. Forbes. "Nonlinear interactions in the upper atmosphere: The s = 1 and s = 3 nonmigrating semidiurnal tides." *J. Geophys. Res* 107(A8) (2002): 1157.

Apostolov, E.M., D. Altadill and L.F. Alberca. "Characteristics of quasi-2-day oscillations inthe foF2 at northern middle latitudes." *J. Geophys. Res.* 100 (1995): 12163–12171.

Baumgaertner, A.J.G., A.J. McDonald, G.J. Fracer and G.E. Plank. "Long-term observations of mean winds and tides in the upper mesosphere and lower thermosphere above Scott Base, Antarctica." *J. Atmos. Solar Terr. Phys.* 67 (2005): 1480-1496.

Baumgaertner, A.J.G., M.J. Jarvis, A.J. McDonald and G.J. Fraser. "Observations of the wavenumber 1 and 2 components of the semi-diurnal tide over Antarctica." *J. Atmos. Solar-Terr. Phys.* 68 (2006): 1195–1214.

Beard, G.A., N.J. Mitchell, P.J.S. Williams and M. Kunitake. "Non-linear interactions between tides and planetary waves resulting in periodic tidal variability." *J. Atmos. Solar-Terr. Phys.* 61 (1999): 363–376.

Borries, C., N. Jakowski, Ch. Jacobi, P. Hoffmann and A. Pogoreltsev. "Spectral analysis of planetary waves seen in ionospheric totalel ectron content (TEC): first results using GPS differential TEC and stratospheric reanalyses." *J. Atmos. Sol. Terr. Phys.* 69 (2007): 2442-2451.

Bracewell, R.N. *The Fourier transform and its Applications, 2nd ed.,*. New York: McGraw-Hill, 1986.

Bremer, J., R. Schminder, K. M. Greisiger, P. Hoffmann, D. Kürschner, and W. Singer. "Solar cycle dependence and long-term trends inthe wind field of the mesosphere/lower thermosphere." *J. Atmos. Sol. Terr. Phys.*, 1997: 497-509.

Brook, D. and R.J. Wynne. *Signal processing, Principles and Applications.* London: Edward Arnold, 1998.

Brown, G.M. and J.I. John. "Vertical penetration of planetary waves into the lower ionosphere." *F. Atmos. Terr. Phys.* 41 (1978): 79–385.

Buriti, R.A., W.K. Hocking, P.P. Batista, A.F. Medeiros and B.R. Clemesha. "Observation of equatorial mesosphere winds over Cariri (7.4°S) by a meteor radar and comparison with existing models." *Ann. Geophys* 26 (2008): 485-497.

Burrage, M.D., M.E. Hagan, W.R. Skinner, D.L. Wu and P.B. Hays. "Long-term variability in the solar diurnal tide observed by HRDI and simulated by the GSWM." *Geophys. Res. Lett.* 22 (1995a): 2641–2644.

Burrage, M.D., D.L. Wu, W.R. Skinner, D.A. Ortland and P.B. Hays. "Latitude and seasonal dependence of the semidiurnal tide by the high-resolution Doppler imager." *J. Geophys. Res.* 100(D6) (1995b): 11,313 –11,321.

Carter, D. and B. Balsley. "The summer wind Field between 80–93 km observed by the MSDT radar at Poker Flat, Alaska (65°N)." *J. Atmos. Sci.* 39 (1982): 2905–2915.

Cevolani, G. "Long period waves in the middle atmosphere: response of mesospheric and thermospheric winds to recent minor stratospheric warmings at mid-latitudes." *Ann. Geophys.* 7 (1989): 451–458.

Chang, L.C, Scott E.P. and H.-L. Liu. "Short-term variation of the s = 1 nonmigrating semidiurnal tide during the 2002 stratospheric sudden warming." *J. Geophys. Res.* 114 (2009): D03109.

Chapman, S. and R.S. Lindzen. *Atmospheric tides.* Holland: Reidel, 1970.

Charney, J.G. and P.G Drazin. "Propagation of planetary-scale disturbances from the lower into the upper atmosphere." *J. Geophys. Res.* 66 (1961): 83-109.

Chau, J.L., B.G. Fejer and L.P. Goncharenko. "Quiet variability of equatorial E × B drifts during a sudden stratospheric warming event." *Geophys. Res. Lett.* 36 (2009): L05101.

Chen, J., L. Zhao, Z. Zhao and J. Wu. "Comparison of simaltaneous wind measurements using colocated All-sky meteor radar and MF spaced antenna radar systems." *Progress in Electromagnetics Research Symposium*, 2009: 79-84.

Chen, P.R. "Two-day oscillatio of the equatorial ionization anomaly." *J. Geophys. Res.* 97, no. No. A5 (1992): 6343-6357.

Cho, Y.-M., G.G. Shepherd, Y.-I. Won, S. Sargoytchev, S. Brown and B. Solheim. "MLT cooling during stratospheric warming events." *Geophys. Res. Lett.* 31 (2004): L10104.

Clark, R.R. and Bergin, J.S. "Bispectral analysis of mesosphere winds." (Journal of Atmosphere and Sola-Terrestrial Physics) 59 (1997): 629-639.

Coy, L., D.E. Siskind, S.D. Eckermann, J.P. McCormack, D.R. Allen and T.F. Hogan. "Modelling the August 2002 minor warming event." *Geophys. Res. Lett.* 32 (2005): L07808.

Dartt, D., G. Nastrom and A. Belmont. "Seasonal and solar cycle wind variations, 80–100 km." *J. Atmos. Terr. Phys.* 45 (1983): 707-718.

Davis, R.N., J. Du, A.K. Smith, W.E. Ward and N.J. Mitchell. "The diurnal and semidiurnal tides over Ascension Island (8°S, 14°W) and their interaction with the stratospheric QBO: studies with meteor radar, eCMAM and WACCM." *Atmos. Chem. Phys. Discuss.* 13 (2013): 4785-4837.

Day, K.A. and Mitchell, N.J. "The 16-day in the Arctic and Antantarctic mesosphere and lower thermospher." *Atmos. Chem. Phys* 10 (2010b): 1461-1472.

Day, K.A. and Mitchell, N.J. "The 5-day wave in the Arctic and Antarctica mesosphere and lower thermosphere." *J. Geophs. Res.* 115 (2010a): D01109.

Dowdy, A.J., et al. "Polar mesosphere lower thermosphere dynamics: 1. Mean wind and gravity wave climatology." *J. Geophys. Res.* 112 (2007a): 1.

Dowdy, A.J., R.A. Vincent, D.J. Murphy, M. Tsutsumi, D.M. Riggin and M.J. Jarvis. "The large-scale dynamics of the mesosphere-lower thermosphere during the Southern Hemisphere stratospheric." *Geophys. Res. Lett.* 31 (2004): L14102.

Espy, P.J., R.E. Hibbins, D.M. Riggin and D.C. Fritts. "Mesospheric planetary waves over Antarctica during 2002." *Geophys. Res. Lett.* 32 (21) (2005): L21804.4.

Fagundes, P.R., V.G. Pillat, M.J.A. Bolzan, Y. Sahai, F. Becker-Guedes, J.R. Abalde, S.L. Aranha and J.A. Bittencourt. "Observations of F layer electron density profiles modulated by planetary wave type oscillations in the equatorial ionospheric anomaly region." *J. Geophys. Res*, 2005: A12302.

Forbes, J.M., S.E. Palo and X. Zhang. "Variability of the ionosphere." *J. Atmos. Sol. Terr. Phys.* 62 (2000): 685–693.

Foster, J.C., J.M. Holt, R.G. Musgrove and D.S. Evans. "Ionospheric convection associated with discrete levels of particle precipitation." *Geophys. Res. Lett.* 13 (1986): 656–659.

Fraser, G.J., Yu. I. Portnyagin, J.M. Forbes, R.A. Vincent, I.A. Lysenko and N.A. Marakov. "Diurnal tide in the Antarctic and Artctic mesosphere/lower thermosphere regions." *J. Atmos. Terr. Phys.* 57 (4) (1995): 383–393.

Fraser, G.J., R.A. Vincent, A.H. Manson, C.E. Meek and R.R. Clark. "Inter-annual variability of tides in the mesosphere and lower thermosphere." *J. Atmos. Terr. Phys.* 51 (1989): 555–567.

Fritts, D.C. and R.A. Vincent. "Mesospheric momentum flux studies at Adelaide Australia: Obsrvations and a gravity wave/tidal interaction model." *J. Atmos. Sci* 44 (1987): 605-619.

Fritts, D.C. and S. L. Vadas. "Gravity wave penetration into the thermosphere: sensitivity to solar cycle variations and mean winds." *Ann. Geophys.* 26 (2008): 3841–3861.

Fritts, D.C., D. Janches, H. Iimura, W.K. Hocking, J.V. Bageston and N.M.P. Leme. "Drake Antarctic Agile Meteor Radar first results: Configuration and comparison of mean and tidal wind and gravity wave momentum flux measurements with Southern Argentina Agile Meteor Radar." *J. Geophys. Res.* 117 (2012): D02105.

Garcia, R.R., R. Lieberman, J.M. Russell III and M.G. Mlynczak. "Large-scale waves in the mesosphere and lower thermosphere observed by SABER." *J. Atmos. Sci.* 62 (2005): 4384–4399.

Geller, M., V.A. Yudin, B.V. Kattatov and M.E. Hagan. "Modeling the diurnal tide with dissipation derived from UARS/HRDI measurements." *Ann. Geo-phys.* 15 (1997): 198-1204.

Gilman, D.L., F.J. Fuglister and J.M. Mitchell Jr. "On the power spectrum of “red noise”." *J. Atmos. Sci.* 20 (1963): 182–184.

Gold, E. "Isothermal Layer of the Atmosphere and Atmospheric Radiation." *Roy. Soc. Lond.* (Roy. Soc. Lond.) 82 (1909): 43.

Goncharenko, L., A. Coster, J. Chau and C. Valladares. "Impact of sudden stratospheric warmings on equatorial ionization anomaly." *J. Geophys. Res.* 115 (2010): A00G07.

Goncharenko, L. and S.-R. Zhang. "Ionospheric signatures of sudden stratospheric warming: Ion temperature at middle latitude." *Geophys. Res. Lett.* 35 (2008): L21103.

Gonzalez, W.D., et al. "“What is A Geomagmetic Storm?”." *J. Geophys. Res* 99 (1994): 5771-5792.

Greenwald, et al. "DARN/SUPERDARN, A global view of the dynamics of high latitude convection." *Space Sci. Rev.* 71 (1995): 761–796.

Gregory, J.B. and A.H. Manson. "Winds and wave motions to 110 km at mid-latitudes: III. Response of the mesospheric and thermospheric winds to major stratospheric warmings." *J. Atmos. Sci.* 32 (1975): 1676–1681.

Greisiger, K.M., R. Schminder and D. Kuerschner. "Long-period variations of wind parameters in the mesopause region and the solar cycle dependence." *J. Atmos. Terr. Phys.* 49 (1987): 281–285.

Grieger, N., G. Schmitz and U. Achatz. "The dependence of nonmigrating diurnal tide in the mesosphere and lower thermosphere on stationary planetary waves." *J. Atmos. Sol. Terr. Phys.* 66 (2004): 733–754.

Grinsted, A, J.C. Moore and S. Jevrejeva. "Application of the cross wavelet transform and wavelet coherence to geophysical time series." *Nonlinear Proc. Geoph.* 11 (2004): 561-566.

Hagan, M.E., J.M. Forbes and C. McLandress. "Diurnal tidal variability in the 1 upper mesosphere and lower thermosphere." *Ann. Geophys.* 15 (1997): 1176–1186.

Hagan, M.E., M.D. Burrage, J.M. Forbes, J. Hackney, W. J. Randel and X. Zhang. "QBO effects on the diurnal tide in the upper atmosphere." *Earth Planets Space* 51 (1999): 571–578.

Hagan, M.E. "Comparative effects of migrating solar sources on tidal signatures in the middle and upper atmosphere." *J. Geophs. Res.* 101 (1996): 21 213–21 222.

Hall, G.E, J.W. McDougall, D.R. Moorcroft, J.-P. St.-Maurice, A.H. Manson and C.E. Meek. "SuperDARN Auroral Radar Network observation of meteor echoes." *J. Geophy. Res.* 102, no. A7 (1997): 14603-14614.

Heelis, R.A. "Electrodynamics in the low and middle latitude ionosphere: a tutorial." *J. Atmos. Sol. Terr. Phys.* 66 (2004): 825-838.

Hibbins, R.E., M.P. Freeman, S.E. Milan and J.M. Ruohoniemi. "Winds and tides in the mid-latitude Southern Hemisphere upper mesosphere recorded with the Falkland Islands SuperDARN radar." *Ann. Geophys.* 29 (2011): 1985–1996.

Hibbins, R.E., O.J. Marsh, A.J. McDonald and M.J. Jarvis. "Interannual variability of the S=1 and S=2 component of the semidiurnal tide in the Antarctica MLT." *JASTP* 72 (2010): 794-800.

Hibbins, R.E., P.J. Espy and M.J. Jarvis. "Mean winds and tidesin the mesosphere and lower thermosphere above Halley, Antarctica." *J. Atmos. Sol. Terr. Phys.* 68 (2006): 436–444.

Hibbins, R.E., P.J. Espy and M.J. Jarvis. "Quasi-biennial modulationof the semidiurnal tide in the upper mesosphere above Halley, Antarctica." *Geophys. Res. Lett.* 34 (2007): L21804.

Hibbins, R.E. and M.J. Jarvis. "A long-term comparison of wind and tide measurements in the upper mesosphere recorded with an imaging Doppler interferometer and SuperDARN radar at Halley, Antarctica." *Atmos. Chem. Phys.* 8 (2008): 1367–1376.

Ho, C-H, H-S Kim, J-H Jeong and S-W Son. "Influence of stratospheric quasi-biennial oscillation on tropical cyclone tracks in the western North Pacific." *Geophys. Res. Lett.* 36 (2009): L06702.

Hocking, W.K. "Dynamic coupling precesses between the middle atmosphere and the lower atmosphere." *J. Atmos. Solar Terr. Phys* 58 (1996): 735-752.

Hocking, W.K., B Fuller and B Vandepeer. "Real-time determination of meteor related parameters utilizing modern digital technology." *J. Atmos. Solar-Terr. Phys*, 2001: 155-169.

Hoffmann, P. "Latitudinal and longitudinal variability of mesospheric winds and temperatures during stratospheric warming events." *J. Atmos. Sol. Terr. Phys.* 69 (2007): 2355–2366.

Holton, J.R and M.J Alexander. "Gravity waves in the mesosphere generated by tropospheric convention." (Tellus) 51 A-B (1999): 45-58.

Holton, J.R. "The dynamic meteorology of the stratosphere and mesosphere, in: Research supported by the National Science Foundation Boston." *American Meteorological Society* (American Meteorological Society) 15 (1975): 224.

Hussey, G.C., C.E. Meek, A.H. André, A.H. Manson, G.J., Hall and C.M. Sofko. "A comparison of Northern hemisphere wind using SuperDARN meteor trail and MF radar wind measurements." *J. Geophys. Res.* 105 (2000): 18053–18066.

Igarashi, K., S.P. Namboothiri and P. Kishore. "Tidal structure and variability in the mesosphere and lower thermosphere over Yamagawa and Wakkanai." *J. Atmos. Solar-Terr. Phys.* 64 (2002): 1037–1053.

Iimura, H., D.C. Fritts and D.M. Riggin. "Long-term oscillations of the wind field in the tropicalmesosphere and lower thermosphere from Hawaii MF radar measurements." *J. Geophys. Res.* 115 (2010): D09112.

Iimura, H., D.C. Fritts, M. Tsutsumi, T. Nakamura, P. Hoffmann and W. Singer. "Long-term observations of the wind field in the Antarctic and Arctic mesosphere and lower-thermosphere at conjugate latitudes." *J. Geophys. Res.* 116 (2011): D20112.

Jacobi, C., et al. "Long-term trends in the mesopause wind field obtained from LF D1 wind measurements at Collm, Germany." *Adv. Space Res.* 20 (1997): 2085–2088.

Jacobi, C., Y.I. Portnyagin, E.G. Merzlyakov, T.V. Solovjova, N.A. Makarov and D. Kürschner. "A long-term comparison of mesopause region wind measurements over eastern and central Europe." *Atmos. Solar Terr. Phys.* 67 (2005): 229–240.

Jacobi, Ch. "Nonlinear interaction of planetary waves and the semidiurnal tide as seen from midlatitude mesopause region winds measured at Collm, Germany." *Meteorol. Z.* (Meteorol. Z.), 1999: 28-35.

Jacobi, Ch., C. Arras, D. Kurschner, W. Singer, P Hoffmann and D. Keuer. "Comparison of mesopause region meteor radar winds, medium frequency radar winds and low frequency drifts over Germany." *Adv. Space Res.* 43 (2009): 247–252.

Jacobi, Ch., K. Froehlilch, C. Viehweg, G. Stober and D. Kuerschner. "Midlatitude mesosphere/lower thermosphere meridional winds and temperatures measured with meteor radar." *Adv. Space Res.* 39 (2007): 1278–1283.

Jarvis, M.J. "Quasi-biennial oscillation effects in the semidiurnal tide of the Antarctic lower thermosphere." *Geophys. Res. Lett.* 23 (19) (1996): 2661–2664.

Jenkins, B. and M.J. Jarvis. "Mesospheric winds derived from SuperDARN HF radar meteor echoes at Halley, Antarctica." *Earth planet Space* 51 (1999): 685-689.

Jenkins, G.M. and D.G. Watts. *Spectral Analysis and Its Applications.* Holden-Day, 1968.

Kutiev, I. and P. Mukhtaron. "Modeling of midlatitude F-region response to geomagnetic activity." *J. Geohps. Res.* 106 (2001): 15501-15509.

Labitzke, K. "On the solar cycle-QBO relationship: a summary." *J. Atmos. Sol. Terr. Phys.* 67 (1-2) (2005): 45–54.

Labitzke, K. and B. Naujokat. "The lower Arctic stratosphere in winter since 1952." *SPARC Newsletter,* 15 (2000): 11–14.

Lastovicka, J., P. Krizan, P. Sauli and D Novotna. "Persistence of the planetary wave type oscillations in foF2 over Europe." *Ann. Geophys.* 21 (2003): 1543–1552.

Li, Q, H,-F Graf and M. A Giorgetta. "Stationary planetary wave propagation in Northern Hemisphere winter – climatological analysis of the refractive index." *Atmospheric Chemistry and Physics* 7 (2007): 183-200.

Li, T., T. Leblanc and I.S. McDermid. "Interannual variations of middle atmospheric temperature as measured by the JPL lidar at Mauna Loa Observatory, Hawaii (19.5°N, 155.6°W)." *J. Geophys. Res.* 113 (2008): D14109.

Lieberman, R.S., D.M. Riggin, D.A. Ortland, S.W. Nesbitt and R.A. Vincent. "Variability of mesospheric diurnal tides and tropospheric diurnal heating during 1997–1998." *J. Geophys. Res.* 112 (2007): D20110.

Lieberman, R.S., J. Oberheide, E.E. Remsberg M.E. Hagan and L.L. Gordley. "Variability of diurnal tides and planetary waves during November 1978–May 1979." *J. Atmos. Sol. Terr. Phys.* 66 (2004): 517– 528.

Lima, L.M., E.O. Alves, P.P. Batista, B.R. Clemesha, A.F. Medeiros and R.A. Burit. "Sudden stratospheric warming effects on themesospheric tides and 2-day wave dynamics at 7°S." *J. Atmos. Solar-Terr. Phys.* 78-79 (2012): 99-107.

Lindzen, R.S. "Atmospheric Tides." *Annual Review of Earth and Planetary Sciences*, 1979: 199-225.

Liu, H.-L. and Roble, R.G. "A study of self-generated stratospheric sudden warming and it mesosphere-lower thermosphere impacts using the coupled TIME-GCM/CCM3." *J. Geophys. Res.* 107(D23) (2002): 4695.

Luo, Y, A.H. Manson, C.E. Meek, T. Thayaparan, J MacDougall and Hocking W. K. "The 16-day wave in the mesosphere lower thermosphere: simaltaneous observation at Saskatoon (52 degrees N, 107 degrees W) and London (43 degree N, 81 degrees W), Canada." *J. Atmos. Sol. Terr. Phys* 64 (2002): 1287-1307.

Luo, Y., A.H. Manson, C.E. Meek, K. Igarashi and C Jacobi. "Extra long period (20–40 day) oscillations in the mesospheric and lower thermospheric winds: observations in Canada, Europe and Japan, and considerations of possible solar influences." *J. Atmos. Solar-Terr. Phys.* 63 (2001): 835–852.

Luo, Y., A.H. Manson, C.E. Meek, C.K. Meyer and J.M Forbes. "The quasi 16-day oscillations in the mesosphere and lower thermosphere at Saskatoon (52 degrees N, 107 degrees W), 1980–1996." *J. Geophs. Res.* 105 (D2) (2000): 2125–2138.

Lysenko, I.A., Portnyagin, Yu. I., Fakhrutdinova, A.N., Ishmuratov R.A. Manson, A.H. and Meek, C. E. "Wind regime at 80–110 km at midlatitudes of the northern-hemisphere." *J. Atmos. Terr. Phys.* 56 (1994): 31–42.

Malinga, S.B., L.M.G. Poole and R.A. Vincent. "Long term variations in the mesospheric mean flow observed at Grahamstown (South Africa) and Adelaide (Australia)." *J. Atmos. Solar Terr. Phys.* 66 (2004): 1745-1754.

Malinga, S.B., L.M.G. Poole and R.A. Vincent. "Simultaneous observation of atmospheric summer tides at Grahamstown (South Africa) and Adelaid (Australia)." *JASTP* 60 (1998): 1459-1469.

Malinga, S.B. *PhD Thesis, A comparative study of atmospheric dynamics in the mesosphere and lower thermosphere (MLT) near Grahamstown (South Africa) and Adelaide (Australia),.* Rhode: Rhode University, 2001.

Malinga, S.B., and J.M. Ruohoniemi. "The quasi-two-day wave studied using the Northern hemisphere SuperDARN HF radars." *Ann. Geophys.* 25 (2007): 1767-1778.

Manson, A.H., and C.E. Meek. "Climatologies of mean winds and tides observed by Medium frequency radars at Tromso (70◦N) and Saskatoon (52◦N) during 1987–1989." *Can. J. Phys.* 69 (1991): 966–975.

Manson, A.H., et al. "Climatologies of semi-diurnal and diurnal tides in the middle atmosphere (70–110 km) at middle latitudes (40–55◦)." *J. Atmos. Sol. Terr. Phys.* 51 (1989): 579–593.

Manson, A.H., et al. "Mesopause dynamics from the Scandinavian triangle of radars within the PSMOS-DATAE Project." *Ann. Geophys.*, 2004: 367-386.

Manson, A.H., et al. "Modulation of gravity waves by planetary waves (2 and 16 d): observations with the North American-Pacific MLT-MFR radar network." *J. Atmos. Solar-Terr. Phys.* 65 (2003): 85–104.

Manson, A.H., et al. "Wave activity (planetary, tidal) throughout the middle atmosphere (20–100 km) over the CUJO network: Satellite (TOMS) and Medium Frequency (MF) radar observations." *Ann. Geophys.* 23 (2005): 305–323.

Manson, A.H., et al. "Winter warmings, tides and planetary waves: comparisions between CMAM (with interactive chemistry) and MFR-MetO observations and data." *Ann. Geophys.* 24 (2006): 2493–2518.

Matsuno, T. "A dynamical model of the stratospheric sudden warming." *J. Atmos. Sci.* 28 (1971): 1479–1494.

Matthews, D.M., M.L. Parkinson, P.L. Dyson and J.C. Devlin. "Optimising estimates of mesospheric neutral wind using the TIGER SuperDARN radar." *Adv. Space Res.* 38 (2006): 2353–2360.

Matthews, D. *Optimising Meteor Echo Detection Rates for the TIGER SuperDARN Radar.* Bundoora, Victoria: La Trobe University , 2003.

Mayr, H.G., J.G. Mengel, F.T. Huang and E.R. Nash. "Equatorialannual oscillation with QBO-driven 5-year modulation in NCEP data." *Ann. Geophys.* 25 (2007): 37–45.

Mayr, H.G., J.G. Mengel, K.L. Chan and F.T. Huang. "Middle atmosphere dynamics with gravity wave interactions in the numerical spectral model: Zonal mean variations." *J. Atmos. Solar Terr. Phys.* 72 (2010): 807-828.

Mayr, H.G., J.G. Mengel, E.R. Talaat, H.S. Porter and K.L. Chan. "Mesospheric non-migrating tides generated with planetary waves: I. Characteristics." *J. Atmos. Terr. Phys.* 67 (2005): 959–980.

Mbatha, N.M. *Study on 2002 Sudden Stratospheric Warming, Mesosphere-1 Lower Thermospheric wind structure and dynamics and middle atmospheric temperature structure, based on SuperDARN HF RADAR, LIDAR, Riometer, Satellites and Models.* PhD Thesis, University of KwaZulu-Natal, 2012.

Mbatha, N., V. Sivakumar, S.B. Malinga, H. Bencherif and S.R. Pillay. "Study on the impact of sudden stratosphere warming in the upper mesosphere-lower thermosphere regions using satellite and HF radar measurements." *Atmos. Chem. Phys.* 10 (2010): 3397–3404.

McHall, Y.L. "Nonlinear planetary wave instability and blocking." *Advances in Atmospheric Sciences* 9 (1992): 173-190.

McKinley, D.W.R. *Meteor Science and Engineering.* McGraw-Hill, 1961.

Merzlyakov, E.G. and Y.I. Portnyagin. "Long-term changes in theparameters of winds in the midlatitude lower thermosphere (90–100 km)." *Izv. Atmos. Oceanic Phys.* 35 (1999): 531–542.

Merzlyakov, E.G. and Yu.I. Portynyagin. "Long-term changes in the parameters of wind in the mid-latitude lower thermosphere (90-100 km)." *Atmosphereic and Oceanic Physics* 35 (1999): 482-493.

Merzlyakov, E.G., D.J. Murphy, R.A. Vincent and Yu.I. Portnyagin. "Long-term tendencies in the MLT prevailing winds and tides over Antarctica as observed by radars at Molodezhnaya, Mawson and Davis." *J. Atmos. Solar-Terr. Phys.* 71 (2009): 21–32.

Merzlyakov, E.G., et al. "On the longitudinal structure of the transient day-to-day variation of the semidiurnal tide in the mid-latitude lower thermosphere – I.Winter season." *Ann. Geophys.* 19 (2001): 545–562,.

Middleton, H.R., N.J. Mitchell and H.G. Muller. "Mean winds of the mesosphere and lower thermosphere at 52 degrees N in the period 1988–2000." *Ann. Geophys.* 20 (2002): 81–91.

Misiti, M., Y Misiti, G. Oppenheim and J. Poggi. *Wavelet Toolbox.* The MathWork, 1996.

Mitchell, N., H.R. Middleton, A.G. Beard, P.J.S. Williams and H. G. Muller. "The 16-day planetary wave in the mesosphere and lower thermospher." *Ann. Geo. Atmos. Hydro. And Space*, 1999: 1447-1456.

Mitchell, N.J., P.J.S. Williams, A.G. Beard, G.R. Buesnel and H.G. Muller. "Nonlinear planetary/tidal wave interactions in the lower thermosphere observed by meteor radar." *Ann. Geophys* 19 (1996): 364-366.

Mitchell, N.J., Pancheva, D., Middleton, H.R., Hagan, M.E., et al. "Mean winds and tides in the Arctic mesosphere and lower thermosphere." *J, Geophs. Res.* 107 (A1) (2002): 1004.

Mthembu, S.H, V. Sivakumar, N.J. Mitchell, and S.B. Malinga. "Studies on planetary waves and tide interaction in the mesosphere/lower thermosphere region using meteor RADAR data from Rothera (68°S, 68°W), Antarctica." *J. Atmos. Sol. Terr. Phys.* 102 (2013): 59–70.

Mthembu, S.H. *An investigation of Ultra Low Frequency (ULF) pulsations using radar data and solar wind data.* Durban: University of KwaZulu-Nata, 2007.

Müller-Wodarg, I.C.F., A.D. Aylward, and T.J. Fuller-Rowell. "Tidal oscillations in the thermosphere: a theoretical investigation of their sources." *J. Atmos. Solar-Terr. Phys.* 63 (2001): 899–914.

Murphy, D.J., et al. "A climatology of tides in the Antarctic mesosphere and lower thermosphere." *J. Geophys. Res.* 111 (2006): D23104.

Murphy, D.J., et al. "Observations of a nonmigrating component of the semidiurnal tide ocer Antarctica." *J. Geophys. Res.* 108(D8) (2003): 4241.

Murphy, D.J., W.J.R. French and R.A. Vincent. "Long-period planetary waves in the mesosphere and lower thermosphere above Davis, Antarctica." *J. Atmos. Solar-Terr Phys* 69 (2007): 2118–2138.

Nakamura, T, T Tsuda and M Tsutsumi. "Meteor wind obsevation with the MU radar." *Radio Sci* 26 (1991): 875-869.

Namboothiri, S.P., C.E. Meek and A.H. Manson. "Variations ofmean winds and solar tides in the mesosphere and lower thermosphereover time scales ranging from 6 months to 11 yr: Saskatoon, 52°N, 107°W." *J. Atmos. Terr. Phys.* 56 (1994): 1313–1325.

Ortland, D.A. and M.J. Alexander. "Gravity wave influence on the global structure of the diurnal tide in the mesosphere and lower thermosphere." *J. Geophys. Res.* 111 (2006): A10S10,.

Pancheva, D. "Evidence for non-linear coupling of planetary waves and tides in the lower thermosphere over Bulgaria." *J. Atmos. Terr. Phys.* 62 (2000): 115–132.

Pancheva, D. "Non-linear interaction of tides and planetary waves in the mesosphere and lower thermosphere." *Phys. Chem. Earth PT C* 26 (2001): 411–418.

Pancheva, D. V. and P. Mukhtarov. "Wavelet analysis on transient behaviour of tidal amplitude fluctuations observed by meteor radar in the lower thermosphere above Bulgaria." *Ann. Geophys.* 18 (1999): 316– 331.

Pancheva, D. V., N.J. Mitchell, R.R. Clark, J. Drobjeva and J. Lastovicka. "Variability in the maximum height of the ionoapheric F2-layer over Millstone Hill (September 1998-March 2000); influence from below and above." *Ann. Geophysicae* 20 (2002): 1807-1819.

Pancheva, D. and I. Lysenko. "Quasi-two-day fluctuations observed in the summer F-region electron maximum." *Bulg. Geophys. J.* 14(2) (1988): 41–51.

Pancheva, D. and N. J. Mitchell. "Planetary waves and variability of the semidiurnal tide in the mesosphere and lower thermosphere over Esrange (68°N, 21°E) during winter." *J. Geophys. Res.* 109 (2004): A08307.

Pancheva, D., L. Alberca and B. De La Morna. "Quasi-two-day variations observed in the lower and upper ionosphere over Europe." *Bulg. Geophys. J.* 17 (1994): 24-32.

Pancheva, D., R. Schminder and J. Lastovicka. "27-day fluctuations in the ionospheric D-region." *J. Atmos. Terr. Phys.* 53 (1991): 1145–1150.

Pancheva, D., et al. "Two-day wave coupling of the low-latitude atmosphere system." *J. Geophys. Res.* 111 (2006): 7313.

Pant, T. K., et al. "Evidence for direct solar control of the mesosphere dynamics through dayglow and redar measurements." *Ann. Geophys* 22 (2004): 3299-3303.

Paschmann G., S., S. Haaland and R. Treumann. ""“Auroral Plasma Physics”." *Space Sci. Rev.* 103 (2002): 1–486.

Percival, D.B. and D.A. Rothrock. "‘‘Eyeballing’’ trends inclimate time series: a caution note." *J. Climate* 18 (2005): 886–891.

Petenko, I.V. and S. Argentina. "The annual behavior of the semidiurnal and diurnal pressure variation in East Antarctica." *American Metereological Society*, 2002: 1093-1100.

Polikar, R. *‘The wavelet tutorial part II ‘.* http://ingineering.rowan.ude/~polikar/WAVELETS/Wtpart3.html, 2002.

Portnyagin, Y.I., et al. "Dynamics of the Antarctic and Arctic mesosphere and lower thermosphere regoins, I, The prevailing winds." *J. Atmos. Terr. Phys.* 55 (1993a): 827-841.

Portnyagin, Y.I., et al. "Long-term trends andyear-to-year variability of mid-latitude mesosphere/lower thermosphere winds." *J. Atmos. Sol. Terr. Phys.* 68 (2006): 1890–1901.

Portnyagin, Y.I., et al. "Monthly mean climatology of the prevailing winds and tides in the Arctic mesosphere/lower thermosphere." 22 (2004): 3395-3410.

Portnyagin, Y.I., J.M. Forbes, G.M. Fraser, R.A. Vincent, S.K. Avery, I.A. 1 Lysenko and N.A. Makarov. "Dynamics of the Antarcticand Arctic mesosphere and lower thermosphere regions—II." *J. Atmos. Terr. Phys. The semidiurnal tide* 55 (1993b): 843–855.

Portnyagin, Y., E. Merzlyakov J. Forbes, N. Makarov and S. Palo. "The summertime 12-h wind oscillation with zonal wavenumber s = 1 in the lower thermosphere over the South Pole." *Ann. Geophys.* 16 (1998): 828–837.

Prolss, G.W. *Ionospheric F-region storms, in: Handbook for atmospheric Electrodynamics.* Vols. Vol. 2, (Ed) Volland. Boca Raton: CHC Press, 1995.

Randel, W.J. "Global variations of zonal Mean ozone during stratospheric warming events." *J. Atmos. Sci.* 50 (1993): 3308–3321.

Richmond, A.D. and J.P. Thayer. "“Ionospheric Electrodynamics: A Tutorial”." In *Magnetospheric Current Systems*, by S-I Ohtani, R. F. Hesse and R. L. Lysak, 131–146. 2000.

Riggin, D.M., D.C. Fritts, M.J. Jarvis and G.O.L. Jones. "Spatialstructure of the 12-hour wave in the Antarctic as observed byradar." *Earth Planets Space* 51 (1999): 621–628.

Riggin, D.M., et al. "MF radar observations of seasonal variability of semidiurnalmotions in the mesosphere at high northern and southern latitudes." *J. Atm. Sol. Terr. Phys.* 65 (2003): 483 – 493.

Riggin, D.M., et al. "Observations of the 5-day wave in the mesosphere and lower thermosphere." *J. Atmos. Solar-Terr. Phys.* 68 (2006): 323–339.

Rishbeth, H. "The ionospheric E-layer and F-layer dynamos—a tutorial review." *J. Atmos. Space Phys.* 59 (1997): 1873.

Rishbeth, H. and M Mendillo. "Patterns of F2-layer variability." *J. Atmos. Sol. Terr. Phys.* 63 (2001): 1661–1680.

Salby, M.L. "Survey of planetary-scale travelling waves: the state of theory and observations." *Rev. Geophys. Space Phys.* 22 (1984): 209–236.

Sandford, D.J. *Dynamics of the stratosphere, mesosphere and thermosphere.* Bath: University of Bath, 2008.

Sandford, D.J., C.L. Beldon, R.E. Hibbins and N.J. Mitchell. "Dynamics of the Antarstic ans Arstic mesosphere and lower thermosphere: 1. Mean winds." *Atmos. Chem. Phys.* 10 (21) (2010): 10273-10289.

Sathishkumar, S. and S. Sridharan. "Planetary and gravity waves in the mesosphere and lower thermosphere region over Tirunelveli (8.7°N, 77°E) during stratospheric warming events." *Geophys.Res. Lett.* 36 (2009): L07806.

Schoeberl, M.R. "Stratospheric warmings: observations and theory." *Rev. Geophys.* 16 (1978): 521–238.

Seidel, D.J. and J.R. Lanzante. "An assessment of threealternatives to linear trends for characterizing global atmospherictemperature changes." *J. Geophys. Res.* 109 (2004): D14108.

Singer, W., et al. "The wind regime of the mesosphere and lower thermosphere during the DYANA campaign – I. Prevailing winds." *J. Atmos. Terr. Phys.* 56 (1994): 1717–1729.

Smith, J.O. " Mathematics of the Discrete Fourier Transform (DFT)." W3K Publishing, http://books.w3k.org/, (2003), ISBN 0-9745607-0-7.

Spizzichino, A. "Etude des interactions entre les differentes composantes du vent dans la haute atmosphere: 3. Theorie des interactions non lineaires entre les ondes atmospheriques." *Ann. Geophys.* 25 (1969): 773–783.

Sprenger, K. and R. Schminder. "Solar cycle dependence of winds in the lower ionosphere." *J. Atmos. Terr. Phys.* 31 (1969): 217–221.

Sridharan, S., S. Sathishkumar and S. Gurubaran. "Variabilities of mesospheric tides and equatorial electrojet strength during major stratospheric warming events." *Ann. Geophys.* 27 (2009): 4125–4130.

Sridharan, S., S. Sathishkumar and S. Gurubaran. "Variabilities of mesospheric tides during sudden stratospheric warming events of 2006 and 2009 and their relationship with ozone and water vapour." *J. Atmos. Solar-Terr. Phys.* 78-79 (2012): 108-115.

Stober, G. and Ch. Jacobi;" Meteor head velocity determination". *Wiss. Mitteil. Inst. f. Meteorol. Univ. Leipzig*. Band 4 (2007): 47-56

Teitelbaum, H. and F. Vial. "On the tidal variability induced by non-linear interaction with planetary waves." *J. Geophys. Res.* 96 (1991): 14 169–14 178.

Torrence, C. and G. P. Compo. "A Practical Guide to Wavelet Analysis." *Bulletin of the American Meteorological Society* 79 (1998): 61-78.

Tung, K. K. and H. Yang. "Global QBO in circulation and ozone. Part I: Reexamination of observational evidence." *J. Atmos. Sci.* 51 (1994): 2699–2707.

Volland, H. *Atmospheric tidal and planetary waves.* Springer, 1988.

Walker, A.D.M. "The SHARE Radar at SANAE, Antarctica." *S. Afr. J. Sci.* 98 (2002): 257-268.

Walker, A. D. M., J. M. Ruohoniemi, K. B. Baker, R. A. Greenwald, J. C. Samson. "Spatial and temporal behaviour of ULF pulsations observed by the Goose Bay HF radar." *J. Geophys. Res.*, 97 (A8) (1992): 12187-12202.

Walter, D.G., T.T Bruce, L.C.G. Alicia, J.S Edward, T. Frances and I.A Syun. "Solar wind magnetosphere coupling during intense magnetict storm." *J. Geophys. Res.* 94 (1989): 8835–8851.

Wang, J., and E. Zivot. "A Bayesian time series model of multiple structural changes in level, trend and variance." *J. Bus. Econ.Statist.* 8 (2000): 374–386.

Wilson, A. *IMAGING RIOMETER OBSERVATIONS ON ENERGETIC ELECTRON PRECIPITATION AT SANAE IV, ANTARCTICA.* Potchefstroom: University of Potchefstroom, 2000.

Xiong, J., W. Wan, B. Ning, L. Liu and Y. Gao. "Planetary wave-type oscillations in the ionosphere and their relationship to the mesosphereic/lower thermosphereic and geomagnetic disturbances at Wuhan (30.6deg N, 114.5 deg E)." *J. Atmos. Sol.-Terr Phys* 68 (2006): 498-508.

Younger, P.T., I. Astin, D.J. Sandford and N.J. Mitchell. "The sporadic radiant and distribution of meteors in the atmosphere as observed by VHF radar at Arctic, Antarctic and equatorial latitudes." *Ann. Geophys* 27 (2009): 2831-2841.

Zhang, S.-R., W.L. Olive and S. Fukaol. "MU radar and ion drift model." *Adv. Space Res.* 27 (2001): 115-120.

Zhang, X., J.M. Forbes and M.E. Hagan. "Longitudinal variation of tides in 1 the MLT region: 1. Tides driven by tropospheric net radiative heating." *J. Geophys. Res.* 115 (2010): A06317.